Investigation and Modeling of Heterogeneously Catalyzed G/L Reactions in Microreactors

zur Erlangung des akademischen Grades eines
DOKTORS DER INGENIEURWISSENSCHAFTEN (Dr.-Ing.)

der Fakultät für Chemieingenieurwesen und Verfahrenstechnik des
Karlsruher Instituts für Technologie (KIT)

genehmigte
DISSERTATION

von
M.Sc Furkan Özkan
aus Sakarya, Türkei

Hauptreferentin: Prof. Dr. Bettina Kraushaar-Czarnetzki
Korreferent: Prof. Dr. Uwe Hampel
Tag der mündlichen Prüfung: 27.09.2013

Zusammenfassung

Um mikrostrukturierte Reaktoren für die Mehrphasenströmung zu optimieren und ihr Verhalten beschreiben bzw. vorhersagen zu können, werden lokale Information der physikalischen und chemischen Vorgänge innerhalb des Reaktors benötigt. Diese Information können über orts- und zeitaufgelöste Messungen oder numerische Methoden beschafft werden. Da es mit den derzeitigen Messmethoden sehr schwierig ist, Messungen im Mikromaßstab in strömenden Medien durchzuführen, werden zunehmend CFD-Codes mit Modellen zur Beschreibung von Mehrphasenvorgängen eingesetzt, um die Vorgänge in mikrostrukturierten Reaktoren sichtbar zu machen.

CFD-Codes werden sowohl in der Industrie als auch auf akademischer Ebene in vielen Bereichen der Verfahrenstechnik erfolgreich eingesetzt, um Probleme einphasiger Systeme zu lösen. Es besteht jedoch erhöhter Bedarf, den Massentransport über die Phasengrenze gekoppelt mit chemischen Reaktionen in mehrphasigen Systemen mathematisch zu beschreiben. Deshalb ist es die Aufgabe dieser Arbeit, einen kommerziellen CFD-Code über dessen Programmierschnittstelle soweit zu erweitern, um solche System zu simulieren. Das so erweiterte Mehrphasenmodell soll anhand analytischer Lösungen einfacher Mehrphasenprobleme als auch experimenteller Daten aus der Literatur validiert werden.

Am Institut für Mikroverfahrenstechnik wurde ein Mehrphasen-Mikroreaktor zur Anilinerzeugung mittels Hydrierung von Nitrobenzol entwickelt. Zum besseren Verständnis der physikalischen bzw. chemischen Vorgänge im Reaktor sollten durch CFD-Simulationen der Stoffübergang vom gasförmigen Wasserstoff in das flüssige Nitrobenzol und die anschließende chemische Reaktion auf einer Katalysatoroberfläche simuliert werden. Der Schwerpunkt der Simulationsrechnungen lag dabei bei der Modellierung des Stofftransportes aus der Gasphase in die flüssige Phase. Da die Datenbasis zur Validierung des erweiterten Mehrphasenmodells auf Basis des Wasserstoff/Nitrobenzol Systems nicht ausreichend war, wurde hierfür das System Luft/Wasser herangezogen. Hierbei wurde bei verschiedenen Schmidt-Zahlen das Aufsteigen einer Luftblase in einem mit Wassergefüllten senkrecht stehenden Kanal simuliert. Der aus den Simulationen ermittelte Stofftransport konnte dann mit theoretischen Modellen und analytischen Lösungen verglichen werden.

Um das System Wasserstoff/Nitrobenzol simulieren zu können, musste der Kontaktwinkel zu einer Edelstahl- und Kunststoffoberfläche mit der statischen Tropfenmethode bestimmt werden. Damit war es möglich das Einströmen von Wasserstoff in einen von Nitrobenzol durchströmten Mikrokanal zu simulieren. Mit dem VOF (Volume of Fluid) Mehrphasenmodel konnte der Einfluss von Oberflächenspannung, geometrischer Parameter und des Kontaktwinkels untersucht werden. Die Kopplung von Stofftransport und chemischer Reaktionen wurde in Simulationsrechnungen integriert. Die Ergebnisse konnten aber aufgrund der dafür benötigten Zeit nicht mehr in diese Arbeit einfließen. Den Code des erweiterten Mehrphasenmodells ist im Anhang zu finden.

I would like to dedicate this thesis to my loving wife ...

Abstract

In order to optimize and describe or predict the behavior of microstructured reactors in multiphase flow one needs to know local information on the physical phenomena. For determination of local information two ways exist: experimental and numerical investigation. Shortcomings of measurement techniques in micro-scale and advantages of Computational Fluid Dynamic (CFD) codes to visualize the system behavior encourages usage and improvement of CFD methods and tools.

In single phase flow with and without reaction CFD tools and experimental procedures are available to solve academic and industrial problems in chemical process engineering. However, there is still a big lack in academic and industrial applications to control and predict the physical and chemical phenomena within the micro-scale for multiphase flow systems particularly with a combination of interfacial mass transfer and reactions. For this reason this work is dedicated to simulation at such a system using a commercial code and novel subroutines based on finite volume method (FVM) and verification of these simulations with analytic results and some relevant experimental results from laboratory and literature.

The hydrogenation of nitrobenzene to aniline has been chosen as a model multiphase reaction, which is suitable for microreactors due to its high exothermicity, low number of side-products, well known physical properties and which is also of industrial importance. For two phase flow researches hydrogen and nitrobenzene are thus used. However, due to lack of data for verification of numerical interfacial mass transfer an air-water system is chosen. Main points in the work

are description and identification of relevant parameters on the hydrodynamic phenomena, interfacial mass transfer and volume change of the gas phase due to mass transfer.

Missing physical parameters such as the static contact angle of hydrogen/nitrobenzene on stainless steel and on a carbon surface have been measured using a static droplet method. Observation of two phase flow system in microreactors has been performed in a special lab microreactor for comparison with the simulations. Influence of surface tension, geometrical properties, and static contact angle on the chosen two phase flow have been explored in a microchannel with gas inlet hole in the channel wall using VOF method. One of the main goals of this work was to the model mass transfer from gas to liquid phase while coupling this with the volume change in the gas phase. Influence of mesh size, and different arbitrary modifications of the Schmidt numbers have been investigated for a free rising bubble in a channel in order to compare the numerical results of mass transfer with theoretical models and analytical solutions. Chemical reaction has been implemented into the simulation files but due to the required simulation time with the required time steps no results are integrated in the written thesis. The code is however added to the Appendix.

Contents

List of Figures

LIST OF FIGURES

LIST OF FIGURES

List of Tables

LIST OF TABLES

List of Symbols

Roman Symbols

A	Interfacial area (m^2)
a, b, c	Coefficients for linear equations of cell boundaries
C	Concentration (kg/m^3)
$\vec{c}, \vec{m}, \vec{f}$	Vectors describing the triangle prism
D	Diffusion coefficient (m^2/s)
d	Diameter (m)
$\mathbf{a}$	acceleration (m^2/s)
F	Force (N)
f_c	Iteratively calculated void fraction
f_r	Delivered void fraction from Fluent code
$\mathbf{g}, \vec{g}$	gravity vector (m^2/s)
h	Height (m)
$\vec{i}$	Normal vector of triangle prism
$\vec{I}$	Normalized vector of vector i
J	Surface specific mass flux (kg/m^2s)

LIST OF SYMBOLS

K	Specific adsorption constant (m^3/kg)
k	Mass transfer coefficient (m/s)
$\vec{k}, \vec{j}, \vec{d}$	Vectors describing the triangle prism
$k^{'}$	modified reaction constant (kg/(g.s.m^3))
k_{Pd}	reaction coefficient for Pd catalyst
k_R	reaction coefficient
L	Characteristic length (m)
$\dot{m}$	Mass transfer rate (kg/s)
M	Mass fraction (-)
m	Mass (kg)
N	Number of mesh cells (-)
Z	Number of vertices (-)
$\mathbf{n}$	Surface normal vector
$\vec{N}$	Transformation vector for $y^{'}$ axe
$\widetilde{\mathbf{n}}$	normalized surface vector
$\widetilde{\mathbf{n}}_{\mathbf{w}}$	Surface normal vector to solid wall
Q	Volume flux (m^3/s)
R	Source term for reaction source (kg/m^3s)
S	Source term (kg/m^3s)
$\vec{S}$	Transformation vector for $z^{'}$ axe
T	Temperature (K)
t	Time (s)

LIST OF SYMBOLS

$\vec{T}$	Transformation vector for $x^{'}$ axe
$\widetilde{\mathbf{t}}_{\mathbf{w}}$	Tangential surface vector to solid wall
U	Velocity (m/s)
u	velocity component in x coordinate (m/s)
V	Volume (m^3)
v	velocity component in y coordinate (m/s)
w	velocity component in z coordinate (m/s)
$\vec{V}$	Centroid vector of cut volume
x	x coordinate
y	y coordinate
z	z coordinate

Greek Symbols

ΔX	Discretization length at interface cells (m)
ϵ	Rate of energy dissipation per unit mass viscosity (m^3/s^2)
κ	Surface curvature (1/m)
ν	Kinematic viscosity (m^2/s)
μ	Dynamic viscosity (Pa.s)
ρ	Density (kg/m^3)
σ	Surface tension coefficient (N/m)
θ	Contact angle

Subscripts

0	Initial

avg	Average
Bat	Batchelor
bub	Bubble
cat	Catalyst
dis	Dissolution
g	Gas phase
gl	From gas phase to liquid phase
hmg	Homogeneous
i	Species i
in	Inlet
int	Interface
Kol	Kolmogorov
l	Liquid phase
lg	From liquid phase to gas phase
mix	Mixture
$norm$	Normalized
out	Outlet
sat	Saturation
σ	Surface tension
w	Wall
x	Cell index in x direction
y	Cell index in y direction

z Cell index in z direction

Acronyms

AR Aspect Ratio

CS Control surface

CV Control volume

CWL Concentration wake length

NB Nitrobenzene

SCA Static contact angle (^{0})

STP Standard temperature and pressure

Dimensionless Numbers

Ca Capillary number

Gr Grashof number

H Henry number

Pe Peclet number

π Pi number

Re Reynolds number

Sc Schmidt number

Sh Sherwood number

We Weber number

Chapter 1

Motivation

The concept of process intensification, which was originally pioneered by Colin Ramshaw in the 1970s, was defined as a reduction of size to allow processes safer, more compact and cheaper than conventional ones in chemical process engineering and technologies [8]. One way towards process intensification is the application of microstructured devices. These reactors possess unique advantages such as enhancing heat and mass transfer not only for single phase flow reactions but also for multiphase flow reactions e.g. by enabling high interfacial area between gas and liquid all over the reaction zone for multiphase flow reactions. Applications where a higher efficiency of the microreactor system is demonstrated are available in literature with discussion of advantages and disadvantages [9, 10]. Microstructured reactors are mostly applied for the research phase, however some of them are also established for production in industry [9, 11].

In order to optimize and describe or predict the behavior of microstructured reactors in multiphase flow one needs to know local information on the physical phenomena. For determination of local information two ways exist: experimental and numerical investigation. Shortcomings of measurement techniques in micro-scale and advantages of Computational Fluid Dynamic (CFD) codes to visualize the system behavior encourage usage and improvement of CFD methods and tools. Nowadays commercial CFD codes are able to capture the interface between two immiscible flows. However, implementation of interfacial mass transfer with coupled mass balance to provide gas volume changes and implementation of reaction in multiphase systems are missing or are under development [12]. There-

fore, a trend in micro chemical engineering is to investigate experimentally and numerically heterogeneously catalyzed gas-liquid reactions to cover these gaps [9]. Identification of relevant parameters by means of experimental studies and implementing numerical methods should provide to control and to manage the chemical reaction in a desired way and thus to increase the benefit for industry. Pharmaceutical and fine chemical production is commonly a multiple-stage

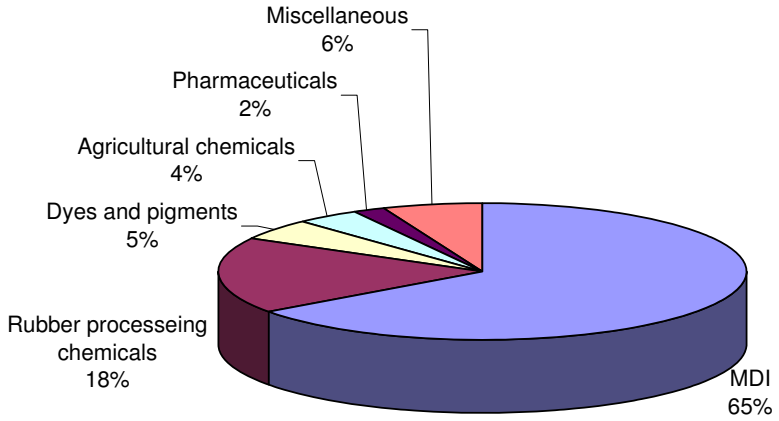

Figure 1.1: Percentage of aniline consumption for applications in industry [1]

synthesis and often involves catalytic hydrogenation. For this reason this work is dedicated to simulation at such a system using a commercial code and novel subroutines based on finite volume method (FVM) and verification of these simulations with analytic results and some relevant experimental results from laboratory and literature. The hydrogenation of nitrobenzene to aniline has been chosen as a model multiphase reaction, which has been investigated in literature and which is also of industrial importance. Aniline, for example, has a worldwide production capacity of 1.4 million tons per year and is an intermediate as 78% of aniline is used for production of isocyanides (see Figure 1.1). It is produced commercially by the reduction of nitrobenzene via hydrogenation as preferred route as shown in Figure 1.2 and it is one of the most important intermediates for many dyes and drugs [1]. The reduction is currently performed as a heterogeneously catalyzed gas phase reaction and preferably conducted in coated reaction tubes

as it is a highly exothermic reaction. The multiphase process has less industrial

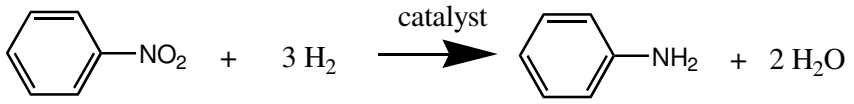

Figure 1.2: Net reaction of hydrogenation of nitrobenzene to aniline

importance today as a recycle of aniline (approx. 95%) is necessary to dilute and remove reaction heat during the process. This recycle and the subsequent product clean-up are clearly uneconomic. Since micro process engineering offers the advantage of fast heat removal and considerable increase in mass transfer by high gas-liquid interfacial area in continuous operation, a reduction or removal of the recycle could be anticipated. From a numerical point of view, this reaction is also suitable to study mass and heat transfer issues since the number of by-products will be limited under temperature control and thus reduces the calculation time in the already complex multiphase simulation due to a less complex reaction network.

Chapter 2

State-of-the-art

2.1 Experimental investigations in literature

Reactor configuration plays an important role to minimize mass transfer limitations. Therefore different options can be applied to provide sufficient interface between gas-liquid-solid (GLS) phases. Cross flow reactors, monolith reactors, membrane reactors are just examples of advanced reactor designs from literature [13, 14].

The main focus in this chapter is, however, not on the reactor types but on the physical and chemical steps occurring in heterogeneously gas liquid reaction: influence of hydrodynamics (flow regimes in minichannels), investigation of interfacial mass transfer from gas to liquid. The dimensionless numbers which are relevant for gas-liquid systems and their meaning at different magnitudes is briefly described in the following:

Reynolds number (Re) is a dimensionless ratio between inertial forces to viscosity forces and characterizes the flow regime (laminar, turbulent flow) in the system. Since the characteristic length L is the diameter of a microchannel, the Reynolds number is usually low; values indicate typically laminar flow.

$$Re = \frac{\rho L U}{\mu} \tag{2.1}$$

The most important dimensionless number for multiphase flow in microre-

actors is the Capillary number (Ca) which represents a ratio of forces between viscosity and surface tension, and it indicates whether the surface tension can play a role on the bubble shape or not.

$$Ca = \frac{\mu U}{\sigma} \tag{2.2}$$

When the Re number is greater than 1 the Weber number (We) is interesting as it indicates the importance of surface tension on the bubble shape. The Weber number is a ratio between inertial force and surface tension force.

$$We = \frac{\rho U^2 L}{\sigma} \tag{2.3}$$

If We and Ca numbers are greater than unity, then influence of surface tension can be neglected.

There are different ways to define the Henry number which represents the concentration jump in immiscible fluids [15]. In this work it is defined as

$$H = \frac{C_{sat} \;\; (saturation\ concentration\ at\ liquid\ interface)}{C_{gas} \;\; (gas\ species\ concentration\ in\ dispersed\ gas\ phase)} \tag{2.4}$$

The Sherwood number (Sh) is relevant for the mass transfer operation. It represents the ratio of convective to diffusive mass transport. The higher the number the better is the support of the mass transfer by convection.

$$Sh = \frac{kL}{D} \tag{2.5}$$

The Schmidt number (Sc) is defined as the ratio of momentum diffusivity (viscosity) and mass diffusivity, and is used to characterize fluid flows in which there are simultaneous momentum and mass transfer processes. It physically relates the relative thickness of the hydrodynamic layer and mass transfer boundary layer. It is not influenced by the reactor system, since it is only a fluid property.

$$Sc = \frac{\mu}{\rho D} \tag{2.6}$$

The Peclet number (Pe) is a dimensionless number relevant in the study of transport phenomena in fluid flows. It is defined to be the ratio of the rate of advection of a physical quantity by the flow to the rate of diffusion of the same quantity driven by an appropriate gradient. In the case of species or mass dispersion, the Peclet number is the product of the Reynolds number and the Schmidt number.

$$Pe = \frac{LU}{D} = ReSc \tag{2.7}$$

2.1.1 Gas-Liquid flow investigations in mini- and microchannels

In order to monitor the fluid regime in minichannels (see Figure 2.1) current methods are the dilution-based method [16], micro particle image velocimetry [16], imaging techniques [17], and non intrusive sensors [18]. A general classification of flow pattern with explanation of the dominant forces is published by Shao et al. [19]. Bubbly flow is characterized by bubbles smaller than the channel diameter. Plug flow (also known as segmented, slug, elongated bubble, bubble train or Taylor flow [19]) is characterized by elongated bubbles with an equivalent diameter larger than the channel diameter. Churn flow is a transitional regime between Taylor flow and annular flow. Generally it occurs at high gas and liquid velocities. Annular flow occurs at high superficial gas velocity in the system. Drop flow is not a common flow pattern in microchannels due to the required low drop diameters.

There exists a dispute about the influence of the gravity force on the flow regime in minichannels. Some investigators report on the influence of gravity force can be neglected; on the another hand, some investigators say that it should be considered. However, the transitional flow pattern map published by Hassan

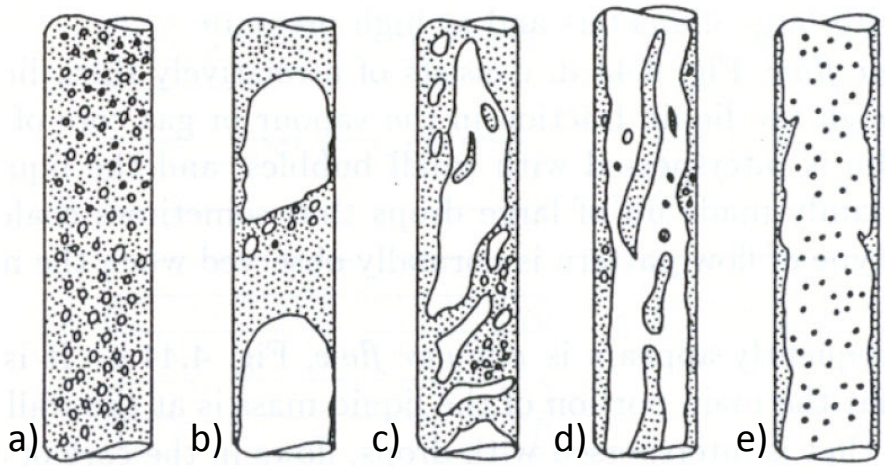

Figure 2.1: Typical flow regimes in minichannels: a) Bubbly flow b) Plug flow c) Churn flow d) Annular flow e) Drop flow

et al. [2] (Figure 2.2) based on comprehensive literature data clearly show that there is an obvious difference between transition of flow regime in horizontal (no influence of buoyancy) and vertical flow (with influence of buoyancy). Gravity force shifts the transition lines of flow regime comparing the continuous lines with dotted lines in Figure 2.2. For instance, buoyancy may assist bubbles to detach from the inlet; bubbly flow regime appears at a smaller superficial liquid velocity in the vertical channel than in the horizontal channel.

Since the fluid regime has a big influence on heat and mass transfer, residence time, and thus on product quality [20], determination of fluid regime is quite important for the individual reactant system. Fluid maps have been reported in the literature mostly as a function of superficial gas and liquid velocity (see Figure 2.2) [2, 21, 22, 23]. However, those maps usually do not in deep consider physical properties and geometric aspects. Influences of those aspects on fluid regime in multiphase systems were comprehensively reviewed and investigated for specific systems [19, 24]. For instance Yue et al. [6] investigated influence of hydraulic diameter of rectangular channels on flow regimes in single microchannel contactors and found that slug flow is more dominant at smaller hydraulic diameters. In the results section the fluid map from Yue et al. [6] will be used for the comparison

of numerical results with experimental results.

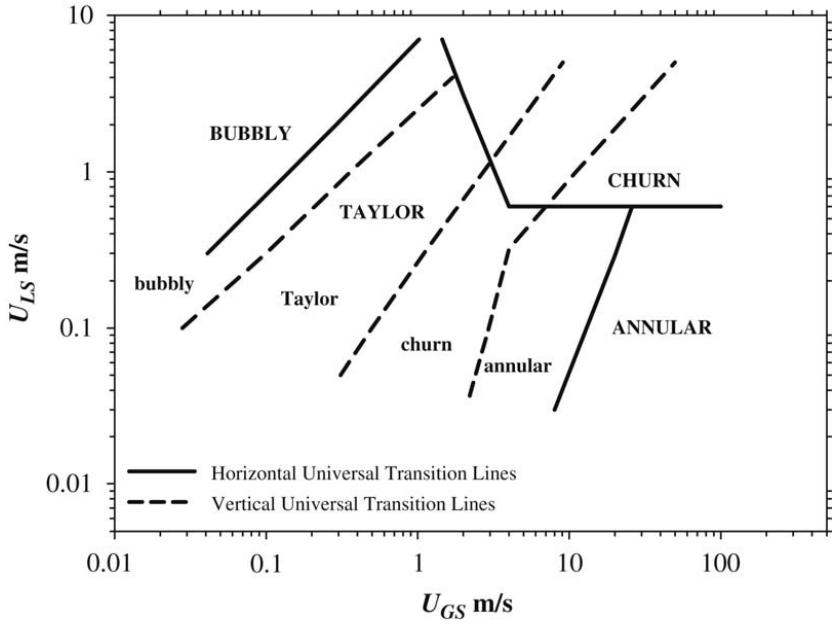

Figure 2.2: Comparison of flow pattern transition lines in horizontal and vertical channel as a function of gas and liquid superficial velocity [2]

2.1.2 Mass transfer studies

The gas dissolution process of a spherical rising gas bubble was investigated experimentally by Takemura and Yabe [25] using a developed technique that has a charged-coupled device (CCD) camera coupled with a microscope to follow the rising bubble. By measuring the bubble size and the rising speed from the bubble motion data captured, they could precisely estimate the drag coefficients and the Sherwood (Sh) number for the dissolution of gas bubbles at Reynolds numbers below 100. They compared the experimental results with several proposed equations for estimating Sh. Finally, they developed a general expression for Sh that may be applied to the entire range of Re $<$100 and Pe$>$1.

Investigators	Sh correlation
Higbie [26]	$Sh=1.13Re^{1/2}\ Sc^{1/2}$
Frössling [27]	$Sh=2+0.6Re^{1/2}\ Sc^{1/3}$
Chao [28]	$Sh=1.13\ \left[1-\left(\frac{2+3\mu_g/\mu}{1+(\rho_g\mu g/\rho\mu)^{0.5}}\right)\frac{1.45}{Re^{0.5}}\right]Pe^{1/2}$
Calderbank [29]	$Sh=0.42\ (\frac{d_{bub}^3.\Delta\rho.\rho_l.g}{\mu_l^2})^{1/3}\ Sc^{1/2}$
Takemura [25]	$Sh=\frac{2}{\sqrt{\pi}}\left[1-\left(\frac{2}{3(1+0.09Re^{2/3})^{3/4}}\right)\right](2.5+Pe^{1/2})$

Table 2.1: Proposed Sh correlations for free rising bubbles in liquid at Reynolds numbers $1 < Re < 100$ from literature

Laser-induced fluorescence (LIF) technique has been recently used for the visualization of dissolved gas concentration field in liquid phase. This optical technique is non-intrusive. Roy and Duke [30] found a significant variation of concentration boundary layer thickness using this technique for a free rising bubble. They observed that the front of the bubble has a thin boundary layer and high concentration gradients while rear of the bubble has low concentration gradients. A planar laser-induced fluorescence (PLIF) technique for visualizing gas liquid mass transfer and wake structure of rising gas bubbles is used by Stohr et al. [4]. Dani et al. [3] presented a modification of the PLIF technique to measure oxygen concentration fields in an aqueous liquid. These two studies focused on the ability of experimental techniques for visualization of concentrations in liquid as it is shown in Figure 2.3. However there was no determination of the mass transfer in their researches. An original direct and non-intrusive technique using Planar Laser Induced Florescence with Inhibition (PLIFI) was presented to quantify the local mass transfer around a single spherical bubble rising in liquid by Francois et al. [31]. They compared experimental results with the Sherwood numbers calculated from the Frössling and Higbie models used for fully contaminated

and clean spherical bubbles, respectively. Results show that all experimental Sherwood numbers are between the two models. An overview of proposed Sh correlation is presented in Table 2.1 for free rising bubbles at low Re numbers. From the different parameters but also the deviations between these correlations it becomes clear that a direct numerical approach for description could be helpful for prediction of mass transfer in general.

2.2 Numerical researches in literature

The numerical investigation of mass transfer in two phase flows can be categorized by two methods. The first method, which is also used in this thesis, considers the direct solution of the species conservation equation. Therefore this direct approach does not involve any empirical models for the mass transfer coefficient. Also in this method the flow field is solved by the Navier−Stokes equations without any empirical correlation. Advantage of this method is that it can be applied for any two-phase flow topology. On the other hand, smaller time steps and finer grids are needed to resolve well the Navier−Stokes equations and species conservation equation. Usage of smaller time steps and finer grids ends up with high CPU time. Because of calculation effort, the method is currently restricted to fundamental investigations of scientific interest. Additionally, the motion of the interface is a key issue and needs to be considered by means of an interface capturing method. In the past, different methods have been developed for computation of two-fluid flows with deformable interfaces. Most widely used ones are the volume-of-fluid (VOF) method [32], the level-set method [33] and the front-tracking method [34]. The level-set method and the front-tracking method are not popular in well-known commercial codes, therefore in the codes CFX, FLUENT and STAR-CD the VOF method is available [35]. An overview of interface calculation approaches in these interface capturing methods is presented in Figure 2.4.

In the second indirect approach averaged equations (Euler-Euler method) are solved instead of local equations or presumed shape of dispersed phase (Euler-Lagrange method) is considered to save CPU time. Disadvantage of this method is that the flow regime and relevant empirical correlations (mass transfer coefficient,

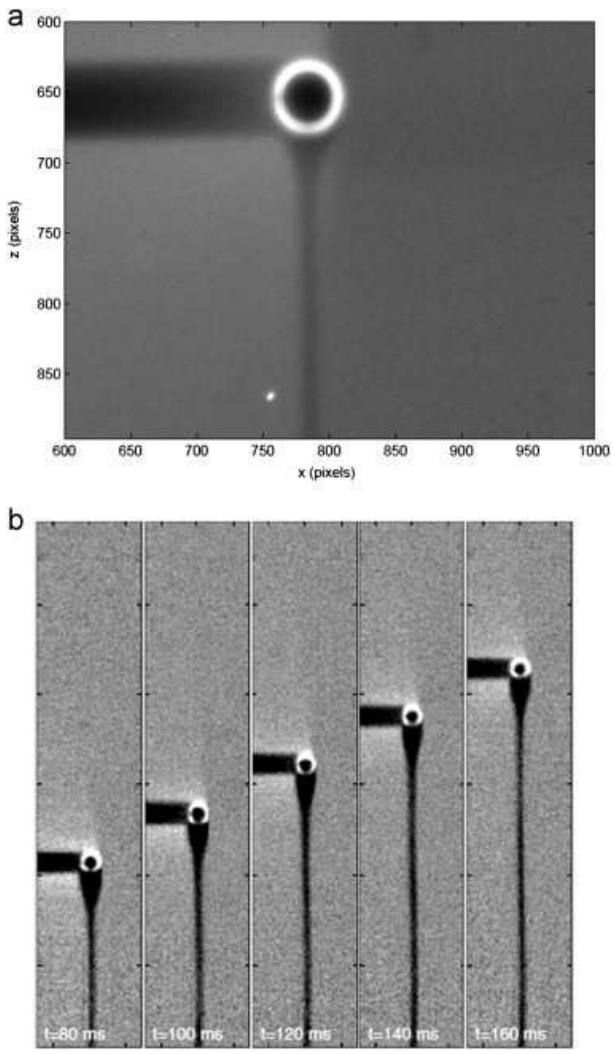

Figure 2.3: (a) PLIF image of a rising air bubble from Dani et al. [3] and (b) PLIF images of a rising carbon dioxide bubble from Stoehr et al. [4] for the determination of gaseous species concentration in the liquid.

drag coefficient) should be known in advance. Therefore they always rely on certain assumptions for mass transfer and/or hydrodynamics and thus require appropriate closure models. The researches about indirect method can be found in literature and not discussed further.

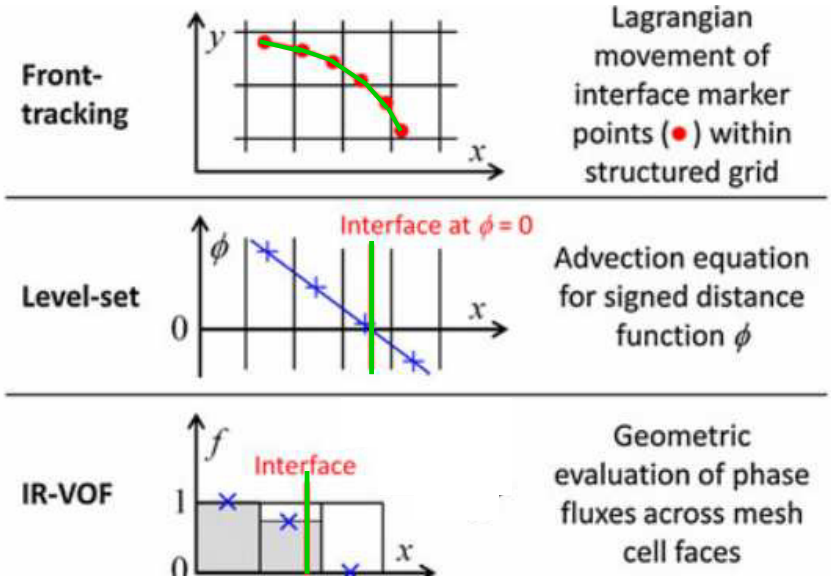

Figure 2.4: Illustration of the different interface capturing methods in two-phase flow. The interface position is indicated by a solid green line [5].

During the research Ansys Fluent, which is the commercial well known CFD code, is used to investigate hydrodynamic phenomena in microstructured devices. The VOF method was originally developed by Hirt and Nichols [32]. The basic concept of the VOF method is the definition of a non-dimensional scalar quantity f, which represents the fraction of the mesh cell volume occupied by the continuous phase, which is here the liquid phase as it is demonstrated in Figure 2.5. Thus, for $f = 0$ the mesh cell is entirely filled with liquid, while for $f = 1$ it is entirely filled with gas. In a mesh cell which has both phases, it is $0 < f < 1$.

The VOF method gives the opportunity to discretize with Piecewise Linear Interface Calculation (PLIC) and therefore it yields the most realistic shape of the dispersed phase [35]. For example, Taha and Cui [36] performed CFD studies on bubble size shape and velocity fields in bubble and slug by using the VOF model in the Fluent package. Computed values of the bubble velocity and diameter were in

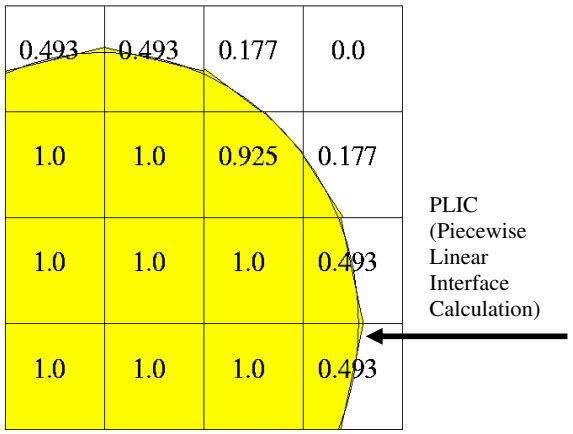

Figure 2.5: Volume of fluid method with discretization of the bubble by PLIC (Piecewise Linear Interface Calculation). Yellow = gas phase, white = liquid; numbers between 0 and 1 = cells with both phases.

excellent agreement with published experimental measurements from Thulasidas et al. [37]. Qian and Lawal [38] studied numerically the influence of geometries and inlet conditions on gas and liquid slug lengths in microreactors using the VOF method in Ansys Fluent code and found consistency with literature results. Özkan et al. [35] evaluated the well known CFD codes for the bubble train flows in minichanells using VOF method and found that VOF-PLIC is the most robust one in Ansys Fluent. These researches are just a couple of examples from literature for the ability of the VOF method in the commercial code.

Important parameters influencing the flow regime in microreactors are surface tension, contact angle (particularly in the case of bubble formation), volumetric flow ratio, gravity (if the channel is oriented vertically) and channel geometry [39, 40, 41].

Since modeling of interfacial mass transfer in multiphase system is complex, the dispersed phase is often considered spherical shape and motionless to describe the physical and mathematical mass transfer in previous studies [42]. Three cases for description of mass transfer can be distinguished due to the investigated phase or phases (see Figure 2.6).

a) Resistance of the mass transfer occurs in both phases (conjugate mass

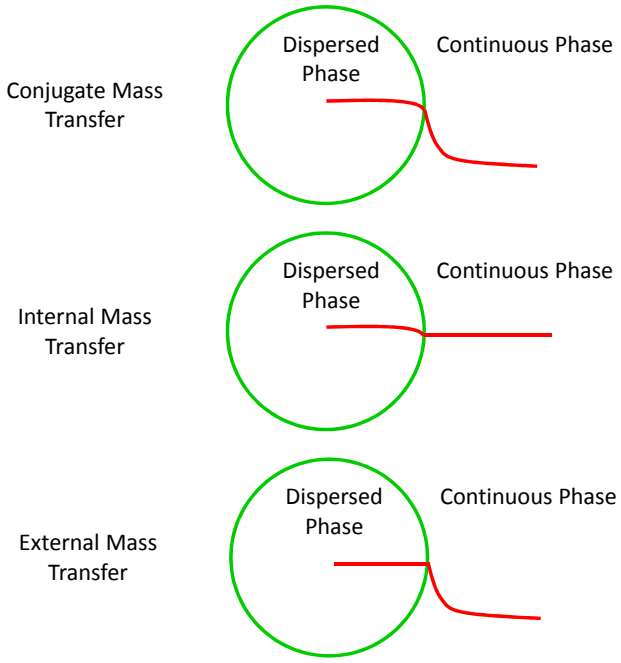

Figure 2.6: Illustration of the different assumptions for relevant mass transfer(Henry=1). The species concentration is indicated.

transfer).

b) Resistance of the mass transfer is in dispersed phase (internal mass transfer).

c) Resistance of the mass transfer is in continuous phase (external mass transfer).

The first numerical simulation of mass transfer combined with the VOF method has been reported by Ohta and Suzuki [43]. They considered three values of the Schmidt number (Sc= 10, 100, 1000) for a rising droplet in a solvent extraction process to simulate conjugate mass transfer and numerically obtained that mass transfer in free rising droplets depends on the drop shape and its physical properties. They also concluded that the concentration field is strongly linked with the flow field. Davidson and Rudman [44] calculated the internal mass transfer for a droplet rising in a liquid column using a new algorithm for calculating convective and diffusive heat or mass transfer based on the VOF method. In these two papers continuity of the concentrations across the interface is assumed (Henry number is unity). Sato et al. [45] developed a numerical simulation method for

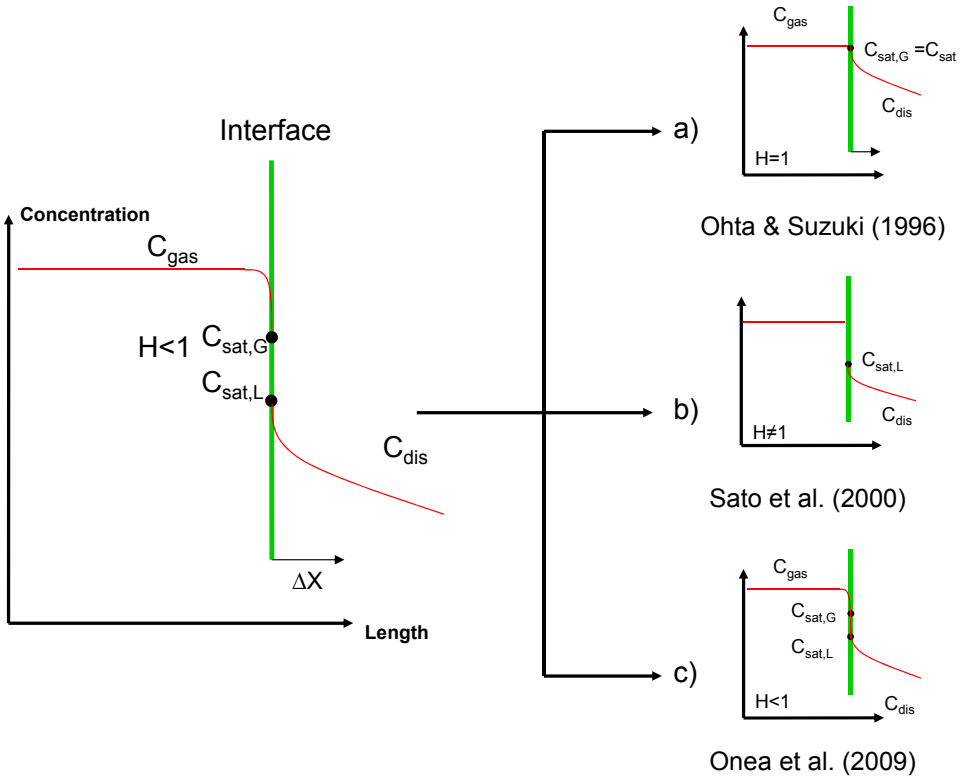

Figure 2.7: Illustration of the different interfacial concentration boundary conditions. Schematic view of the real concentration curve is demonstrated on the left side, on the right different approaches for the concentration boundary conditions. The interface position is indicated by the vertical line.

solving two-phase flow with mass transfer through the interface. The interface is determined by a front-capturing method solving the transport equation of marker density function. From the interface, mass of the dispersed phase dissolves into the continuous phase and diminishes at the rate of dissolution. They considered the species conservation only in liquid phase. Bothe et al. [46] numerically investigated oxygen transfer from an air bubble and bubble train flow into liquid phase at Schmidt numbers between 1 to 1000 using the VOF method. The concentration field is modeled discontinuous at the interface by applying the Henry number to provide the concentration jump in the interface cells. A similar method of concentration field (discontinuous at the interface) has been used by Onea et al. [47] for upward bubble train flow within square and rectangular channels.

They modeled three transport steps in minichannels namely; mass transfer, mass transfer with homogeneously reaction in liquid phase, and mass transfer with heterogeneously reaction which takes places at channel walls. They considered a bubble and surrounding liquid with periodic boundary conditions to provide bubble train flow in minichannels and then named this computational domain as a unit cell. Their study focuses on the influence of the unit cell length, liquid slug length and channel aspect ratio on mass transfer. It was found that the major part of mass transfer is at the bubble front and rear so that short unit cells are more efficient for describing mass transfer. If the main mass transfer resistance is in gas phase at fast heterogeneous reaction on the channel walls long unit cells are more efficient. Illustration of the different interfacial concentration boundary conditions implemented in CFD codes in literature is shown in Figure 2.7. On the left side the real concentration curve is demonstrated. On the right the different methods for concentration field description at interface are explained. Ohta and Suzuki [43] was not able to describe the concentration jump because of unity of Henry number. Sato et al. [45] did not consider the concentration distribution in dispersed phase. The approach of Onea et al. [47] does not allow change of dispersed phase volume due to mass transfer.

Numerical mass transfer studies based on CFD approaches are summarized and categorized in the Table 2.2.

Because of the shortcomings of the measurement techniques for visualization of mass transfer in gas-liquid flow types, this PhD work deals with interfacial mass transfer by help of Computational Fluid Dynamics (CFD) methods. A direct method was chosen for interfacial mass transfer modeling as it can be used for any type of two phase flow. Since the gas distribution in dispersed phase is not important for heterogeneously catalyzed gas-liquid reactions, external mass transfer from dispersed phase into continuous phase is modeled using VOF-PLIC method in Ansys Fluent like Sato approach [45]. However, in comparison to the method of Sato the calculation methods which are applied for the liquid phase in this thesis can be easily added for the gas phase and lead to a full description for all possible cases. For the comparison of the mass transfer results numerical Sh numbers and proposed Sh numbers from Calderbank [29] and Chao [28] are compared in results section.

Investigators	Fluid System	Sc	Method	M.T.C	Size change
Ohta and Suzuki (1996) [43]	A Rising Droplet in air	$10,10^2,10^3$	VOF	Conjugate	No
Sato et.al (2000) [45]	A Rising Droplet in liquid	1	M.D.F	External	Yes
Petera and Weatherley (2001) [48]	A Falling Droplet in liquid	10^4	F.E.M	Conjugate	No
Waheed et.al (2002) [49]	A Falling Droplet in liquid	10^3	F.E.M		
Davidson and Rudman (2002) [44]	A Rising Droplet in liquid	-	VOF	Conjugate	No
Bothe et al. (2003-2004) [46]	A Rising Bubble in liquid	$1 \leq Sc \leq 10^3$	VOF	Conjugate	No
Yang and Mao(2005) [50]	A Rising Droplet in liquid	3000	L.S	Conjugate	No
Koynov (2005-2006) [51, 52]	A Rising Bubble in liquid	$62 \leq Sc \leq 431$	F.T	External	No
Darmana et al. (2006) [53]	A Rising Bubble in liquid	1	F.T	External	No
Wang et al. (2008) [54]	A Rising Droplet in liquid	1	L.S	Conjugate	No
Onea et al. (2009) [47]	A Rising Bubble in liquid	0.8	VOF	Conjugate	No
Ganguli and Kenig (2011) [55]	A Rising Bubble in liquid	500	L.S	Conjugate	No

Table 2.2: Numerical mass transfer studies in CFD with indication of applied method and Mass Transfer Case (M.T.C): Modified Density Function (M.D.F.), Finite Element Method (F.E.M), Level Set (L.S), Front Tracking (F.T.)

As a summary, investigated issues in this PhD work are 1) interface capturing at a certain inlet geometry and special conditions (low liquid flow rates) with VOF-PLIC method 2) transfer of mass from gas interface into continuous phase based on direct method and especially 3) shrinkage of gas because of mass transfer ratio. The chemical reaction with dissolved species on the channel walls was also started in this thesis in combination with issues 1-3 but the required time step time is so small and calculation time is too large for today's CPU power. In order to model the mass transfer the required source terms have been implemented into void fraction, mass conservation and species transport equation. In the next chapter experimental studies will be presented. Mathematical modeling for two phase flow, interfacial mass transfer will be presented in Chapter 3. Numerical results of two phase flow are presented in Chapter 4. Chapter 5 is denoted for direct numerical interfacial mass transfer model.

Chapter 3

Experimental Researches

This chapter is exclusively devoted to experimental results. First, contact angle measurements are described. For numerical simulations static contact angle is required as a boundary condition. Contact angles for nitrobenzene-hydrogen-stainless steel and nitrobenzene-hydrogen-carbon systems were measured using the sessile drop method at various pressures. Results from simulation of the two-phase flow with the static contact angle, which is used as a boundary condition, are reported at Chapter 5. These results then include flow for even a wider range of contact angles as the measured contact angles. Secondly, experimental investigation of flow regimes are described. Two inlet boundary conditions (see Table 3.1) in experimental research were applied into numerical simulation to compare the results.

3.1 Experimental determination of the static contact angle

This section is a short excursion into the experimental determination of the contact angle which is a boundary condition for the simulation recently published [41, 56]. The system hydrogen/nitrobenzene and polished carbon or stainless steel material were analyzed as model representing the situation in the microreactor of fluids-catalyst and fluids-reactor wall interactions.

In order to determine a static contact angle, there are several methods avail-

Figure 3.1: Static sessile drop analysis setup

able [57]. One of the contact angle measurement methods is the static sessile drop method, which is recommended in literature from a comparison of five different contact angle measurement methods [58]. For the static sessile drop method, a camera, a light source, and a stage are required. The camera captures a photo of a drop of liquid on a flat, solid material lit by a parallel light beam.

The applied set-up shown in 3.1 consist of an optical cell (SITEC AG, Maur,Zuerich, 740.2086) with sapphire windows for the observation of the droplet, gas introduction with pressure regulation (Rotarex/SMT, Genlis, France, SL225-16), and liquid dosing through means of a hand-operated pump (SITEC AG, Maur,Zuerich, 750.1400). An Imaging Source C3516-M (KP) (35 mm focal length) lens with 5 mm and 10 mm extension rings was used with a SONY AVC-D5CE CCD camera [59]. A light (HLV-24SW-NR-3W, CCS Inc., Japan) was passed through a series of lenses to create a parallel beam as it is shown Figure 3.1. Special flattened calibration spheres made from metal, which were introduced into the cell to represent a drop, were used to determine the absolute measurement error (3.5 %) of the whole setup.

Images collected from the apparatus were analyzed with a free-software (ImageJ with DropSnake plug-in) used to particularly examine the drop shape in detail. The software fits the drop contour with a spline and determines the contact angle [60]. When analyzing drops, iterations of the contact angle were repeated until the angles and curves were the same in both the initial and final iterations. Since surface roughness and unclean surfaces have a large influence on the measurement of the static contact angle [61], observations have been made

on polished material, and the surfaces have been cleaned chemically and mechanically. Acetone was used to clean the flat, solid material from dusts and other unwanted substances, and then the solid material was washed with hot water. Finally, it was dried with pressurized air.

Important parameters for static contact angle measurements are drop size, pressure, temperature, surface material, and surface roughness of the material from which the microchannels are created [61, 62, 63]. In the measurements it was focused on the influence of pressure and material. Concerning temperature dependence, there is no indication for a strong influence since the microreactor is usually operated at a temperature-pressure combination under which the liquid is far from the boiling point. Under these conditions it is possible to refer to the observations of Bernardin et al. [61] for measurement of the static contact angle of the system water-air-aluminum at various temperatures and pressures. They observed that the influence of temperature is minor until the surface temperature reaches the water boiling temperature. Then the contact angle suddenly decreases with increasing temperature [61].

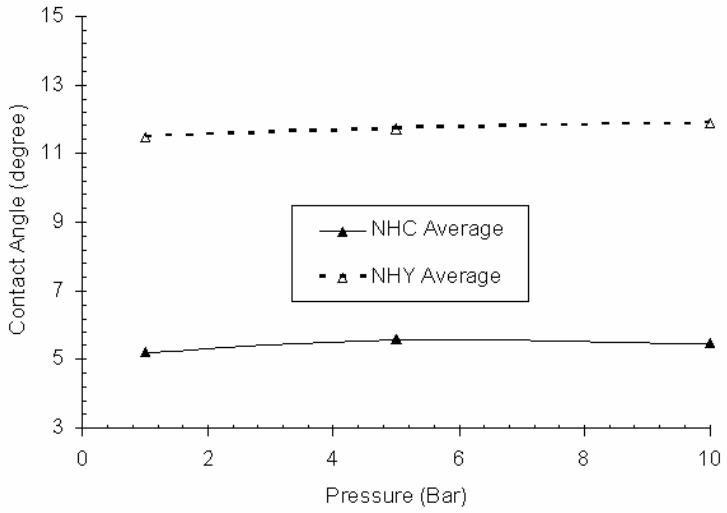

Figure 3.2: Influence of pressure on static contact angle for NHY = nitrobenzene /hydrogen /stainless steel and NHC = nitrobenzene /hydrogen /carbon

The influence of pressure on the static contact angle is shown in Figure 3.2. Static contact angle increases slightly with increasing pressure. This slight trend is in accordance with the observation of pressure influence on static contact angles reported by Bernardin et al. [61]. For the carbon surface the mean contact angle is 5.66^0 with a standard deviation of 0.5^0. For the simulation of hydrogen/nitrobenzene/carbon, a 5^0 static contact angle is used later.

In case of stainless-steel, the mean contact angle is 12.51^0 with a standard deviation of 1.71^0. The lowest contact angle at one bar amounts to 11.69^0 with a standard deviation of 1.22^0. For the respective simulation a value of 12^0 was used.

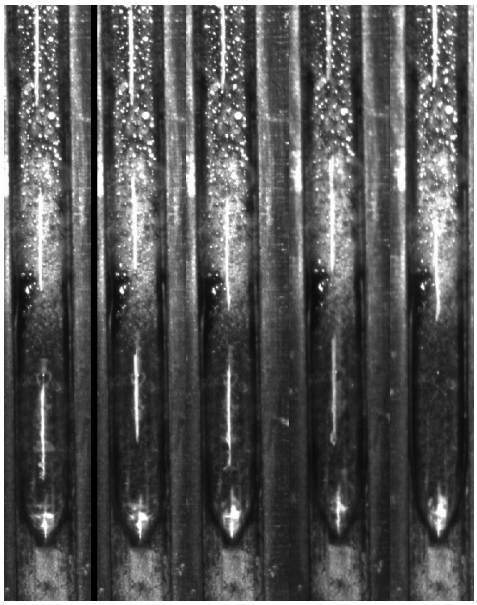

Figure 3.3: Pictures of the flow in a single microchannel; hydrogen mass flow rate = 2.5 ml/min; nitrobenzene mass flow rate 2.5 g/h, 5 g/h, 10 g/h, 20 g/h, 30 g/h from left to right side

3.2 Experimental investigations for flow regime

In the experimental investigation of the flow phenomena in a vertically arranged microchannel the volumetric flow rates of hydrogen and nitrobenzene have been varied. The temperature was 383 K and atmospheric pressure was applied at the

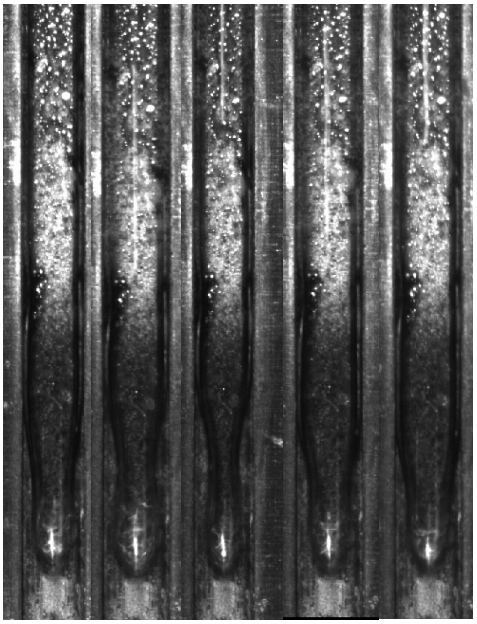

Figure 3.4: Pictures of the flow in a single microchannel; hydrogen flow rate = 5 ml /min; nitrobenzene mass flow rate 2.5 g/h, 5 g/h, 10 g/h, 20 g/h, 30 g/h from left to right side

channel outlet. The hydrogen flow rates were 2.5 ml /min and 5 ml /min at STP conditions. The mass flow rates of nitrobenzene were 2.5 g/h, 5 g/h, 10 g/h, 20 g/h and 30 g/h. The applied microchannel is rectangular with dimensions of 1 mm x 0.4 mm. The channel was mechanically fabricated and a carbon catalyst was deposited on the channel walls. The details on catalyst preparation were published in the Bachelor thesis of S. Geiss [64]. The channel is covered by a glass sheet and the hydrogen is supplied from the back of the channel via a 100 μm hole. Pressure drop has been found to be negligible, i.e. is lower than 0.04 bar on both, the hydrogen and the nitrobenzene inlet. Corresponding Reynolds numbers at hydrogen inlet and at nitrobenzene inlet are 2.41 and 4.82, 1.94 and 22.3, respectively. Volumetric flow ratio between gas and liquid is between 135 and 6.

In Figure 3.3 and Figure 3.4 the flow field for the different hydrogen flow rates, i.e. 2.5 and 5 ml /min, is shown. Each figure is a representative extraction of a photo from a video taken of the single channel for different nitrobenzene

	Hydrogen (ml/min)	Nitrobenzene (g/h)
Case 1	2.5	30
Case 2	5	2.5

Table 3.1: Flow rates of hydrogen and nitrobenzene applied for simulations of the flow field

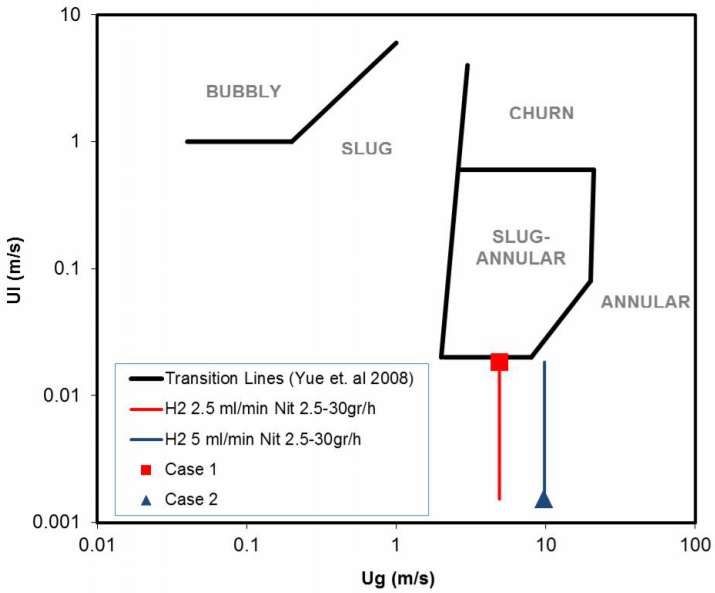

Figure 3.5: Universal transitional lines from Yue et al. [6] and applied experimental ranges. Case 1 and Case 2 represent numerical cases.

flow rates from 2.5 to 30 g/h. For all flow rates the gas bubble is located above the gas inlet. Pulsation, i.e. slug formation, has been observed at high liquid mass flows or/and high gas flow. However, the flow mostly is of annular type. At the high gas flow, i.e. 5 ml/min, there is a constriction of the gas flow at the hydrogen inlet. It is supposed that this is an effect of liquid film formation at higher gas inlet velocity. However, a contribution of the coating could be possible. The coating started somewhat above the hydrogen inlet hole. This space between inlet hole and coating avoided the blocking of the hole during catalyst preparation. Therefore a changing contact angle could influence the flow field. Table 3.1 indicates the cases which have been selected for simulation. Case

1 represents experiments with pulsation, Case 2 was selected as strictly annular.

Yue et al. [6] investigated flow regimes in minichannels having hydraulic diameters of 667, 400 and 200 μm. Flow patterns such as bubbly flow, slug flow, slug-annular flow, churn flow and annular flow were observed in these microchannels at the relevant gas and liquid superficial velocities as it is presented in Figure 3.5. They focused on to determine an empirical correlation based on the superficial liquid Weber numbers to interpret the transition from Taylor flow to unstable slug flow for vertical upward flow. In order to compare the experimental studies the experimental range of conditions is integrated in the universal transitional lines map from Yue et al. [6] (geometrical properties match well). The dark line in Figure 3.5 corresponds to experimental range for the Figure 3.3 while the grey (green) line represents the range for Figure 3.4. The flow regimes of experimental studies show good consistency with the study from Yue et al. [6].

Chapter 4

Mathematical modeling

4.1 Governing equations

The governing equations of fluid flow represent mathematical statements of the conversation law of physics. In this part mass conservation, momentum conservation will be explained step by step for a control volume.

Since the derivation of the system of partial difference equations (PDEs) will be presented in Cartesian (x,y,z) coordinates, mass of fluid in a control volume is expressed as m=$\rho\,\mathrm{d}V = \rho\,\mathrm{d}x\,\mathrm{d}y\,\mathrm{d}z$. A general expression for conservation of mass as applied to a control volume consists of rate of mass increase in fluid element and net rate of flow mass into the fluid element. This can be formulated a mass balance in a control volume (dV) for the fluid element as:

$$\frac{\partial \rho}{\partial t}\,\mathrm{d}x\,\mathrm{d}y\,\mathrm{d}z = \sum_{in} \dot{m} - \sum_{out} \dot{m} \tag{4.1}$$

An infinitesimal box-shaped control volume is considered aligned with the axes in Cartesian coordinates (see Figure 4.1). The dimensions of the box are dx, dy, and dz, and the center of the box is P. Velocity components are u, v, and w in a x,y,z coordinate system. After sum of mass flow rates into and out of the control volume through the faces using Taylor series expansion at the center of the box (point P), $\sum_{in} \dot{m}$ and $\sum_{out} \dot{m}$ in the right-hand side of Equation 4.1

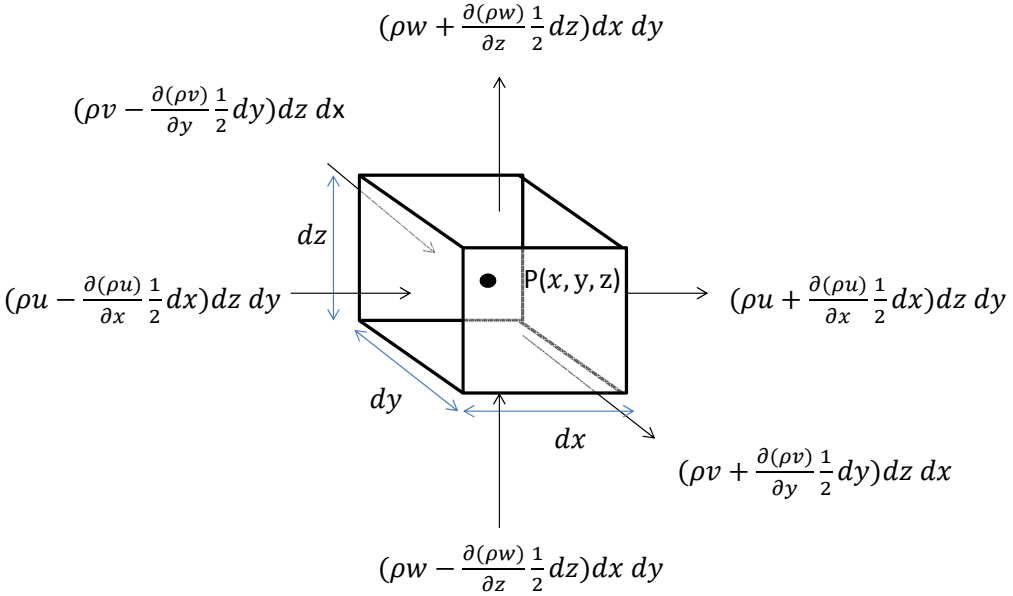

Figure 4.1: The inflow and outflow of mass through each face of a differential control volume in Cartesian coordinates

become

$$\sum_{in} \dot{m} = \left(\rho\, u - \frac{\partial(\rho u)}{\partial x}\frac{1}{2}dx\right) dy\, dz + \left(\rho\, v - \frac{\partial(\rho v)}{\partial y}\frac{1}{2}dy\right) dx\, dz + \left(\rho\, w - \frac{\partial(\rho w)}{\partial z}\frac{1}{2}dz\right) dx\, dy \tag{4.2}$$

$$\sum_{out} \dot{m} = \left(\rho\, u + \frac{\partial(\rho u)}{\partial x}\frac{1}{2}dx\right) dy\, dz + \left(\rho\, v + \frac{\partial(\rho v)}{\partial y}\frac{1}{2}dy\right) dx\, dz + \left(\rho\, w + \frac{\partial(\rho w)}{\partial z}\frac{1}{2}dz\right) dx\, dy \tag{4.3}$$

Combining equations 4.1 to 4.3 and combining and simplifying the terms give

$$\frac{\partial \rho}{\partial t}\,\mathrm{d}x\,\mathrm{d}y\,\mathrm{d}z = -\frac{\partial(\rho u)}{\partial x}dx\,dy\,dz - \frac{\partial(\rho v)}{\partial y}dx\,dy\,dz - \frac{\partial(\rho w)}{\partial z}dx\,dy\,dz \tag{4.4}$$

The volume, dx dy dz, appears in each term and can be eliminated. After rearrangement this yields the following differential equation for conservation of mass in Cartesian coordinates.

$$\frac{\partial \rho}{\partial t} = -\frac{\partial(\rho u)}{\partial x} - \frac{\partial(\rho v)}{\partial y} - \frac{\partial(\rho w)}{\partial z} \tag{4.5}$$

A nabla operation is a convenient mathematical notation and shorthand form for vectorial operators. It can be represented as:

$$\nabla = \frac{\partial}{\partial x} + \frac{\partial}{\partial y} + \frac{\partial}{\partial z} \tag{4.6}$$

After a usage of nabla in Equation 4.5 it becomes

$$\frac{\partial \rho}{\partial t} + \nabla \cdot \mathbf{U} = 0 \tag{4.7}$$

Newton's second law states that the rate of change of momentum of a fluid particle equals the sum of the forces on the particle. This can be defined as following:

$$\sum \vec{F} = \sum \vec{F}_{body} + \sum \vec{F}_{surface} \tag{4.8}$$

In the Equation 4.8 total force in a control volume is equal to

$$\sum \vec{F} = m\mathbf{a} \tag{4.9}$$

In the Equation 4.9 mass can be formulated as a function of density in the

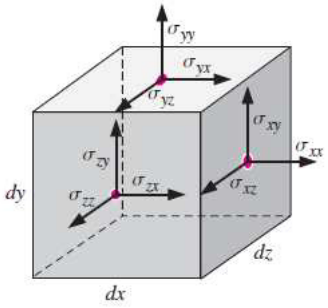

Figure 4.2: Positive components of the stress tensor in Cartesian coordinates on the positive (right, top, and front) faces of a control volume

control volume as it is expressed in Equation 4.10.

$$m = \rho dxdydz \tag{4.10}$$

In the Equation 4.9 acceleration is denoted in differential form

$$\mathbf{a} = \frac{\partial}{\partial t} \cdot \mathbf{U} + u\frac{\partial}{\partial x} \cdot \mathbf{U} + v\frac{\partial}{\partial y} \cdot \mathbf{U} + w\frac{\partial}{\partial z} \cdot \mathbf{U} \tag{4.11}$$

The left term on the right hand side of Equation 4.8 represents body forces and is expressed in long notation as

$$\sum \vec{F}_{body} = \int_{CV} \rho \mathbf{g} dxdydz \tag{4.12}$$

The right term on the right hand side of Equation 4.8 represents surface forces and is expressed in long notation as

$$\sum \vec{F}_{surface} = \int_{CS} \sigma_{ij} \cdot \mathbf{n} dA \tag{4.13}$$

Figure 4.2 shows the positive components at the stress tensor of a control volume. After rearrangements in the Equation 4.8 the general expression for

conservation of momentum as applied to a control volume, yields the following equation:

$$\sum \vec{F} = \int_{CV} \rho \mathbf{g} dV + \int_{CS} \sigma_{ij} \cdot \mathbf{n} dA = \int_{CV} \frac{\partial}{\partial t}(\rho \mathbf{U}) dV + \int_{CS} (\rho \mathbf{U}) \mathbf{U} \cdot \mathbf{n} dA \quad (4.14)$$

The divergence theorem defines that the outward flux of a vector field through a closed surface is equal to the volume integral of the divergence over the region inside the surface. After implementation of divergence theorem to Equation 4.14 it becomes

$$\sum \vec{F} = \int_{CV} \rho \mathbf{g} dV + \int_{CV} \vec{\nabla} \cdot \sigma_{ij} dV = \int_{CV} \frac{\partial}{\partial t}(\rho \mathbf{U}) dV + \int_{CV} \vec{\nabla} \cdot (\rho \mathbf{U}\mathbf{U}) dV \quad (4.15)$$

This is found by Cauchy and therefore it is called Cauchy's equation. In general form it is expressed in the following form:

$$\frac{\partial}{\partial t}(\rho \mathbf{U}) + \vec{\nabla} \cdot (\rho \mathbf{U}\mathbf{U}) dV = \rho \mathbf{g} + \vec{\nabla} \cdot \sigma_{ij} \quad (4.16)$$

4.2 Governing equations for two-phase flow

One phase field approach is used in VOF method. Validity of the continuity of mass conservation and momentum equation in both phases is provided by a mixture density, and mixture viscosity definition.

Mixture density

$$\rho = f_g \rho_g + (1 - f_g) \rho_l \quad (4.17)$$

Mixture viscosity

$$\mu = f_g \mu_g + (1 - f_g) \mu_l \quad (4.18)$$

Using the above mixture definitions, the equations governing the motion of the liquid and the gas phases as well as the dynamic boundary condition at the interface can be combined into one single set of continuity and momentum equations that are valid in the entire two-fluid domain in the VOF method.

In case of no mass transfer the mass conservation equation like the Equation 4.7 is

$$\frac{\partial \rho}{\partial t} + \nabla \cdot \mathbf{U} = 0 \tag{4.19}$$

For the void fraction of gas phase the same equation must be fullfilled according to:

$$\frac{\partial f_g}{\partial t} + \nabla \cdot f_g \mathbf{U} = 0 \tag{4.20}$$

Momentum equation for two phase flow (Equation 4.21) is the derivation of Cauchy's equation (4.16) to Navier-Stokes equation.

$$\frac{\partial}{\partial t}(\rho \mathbf{U}) + \nabla \cdot \rho \mathbf{U}\mathbf{U} = -\nabla p + \nabla \cdot \mu \left(\nabla \mathbf{U} + (\nabla \mathbf{U})^T\right) + \rho \mathbf{g} + \mathbf{f}_\sigma \tag{4.21}$$

For gas-liquid two phase flows, the volume fraction of gas f_g is obtained by numerically solving Equation 4.20, and the volume fraction of liquid f_l is simply computed from 1 - f_g.

In Equation 4.21, $\mathbf{g} = (0, 0, -g)^T$ is the gravity vector, $\mathbf{g} = 9.81 m/s^2$ is the gravitational acceleration and $\mathbf{f}$, standing for attractive forces (e.g. between nitrobenzene molecules), represents the surface tension force per unit volume. For the determination of the surface tension force, in this work the continuum surface force (CSF) model developed by Brackbill et al. [65] was applied. This is the standard model in all commercial computational fluid dynamic codes to consider surface tension forces in combination with VOF methods. The surface tension force in this code is written as

$$\mathbf{f}_\sigma = \sigma \frac{\rho \kappa \nabla f}{1/2(\rho_l + \rho_g)} \tag{4.22}$$

In this equation, σ is the surface tension coefficient of the liquid; ρ is the mixture density, ρ_l and ρ_g represent liquid and gas phase densities, respectively. κ is the surface curvature, which is important for the computations since the contact angle has an influence on the surface curvature. In the CSF model, a surface curvature due to surface tension force is computed from local gradients in the surface normal at the interface:

$$\kappa = \nabla \cdot \frac{\mathbf{n}}{|\mathbf{n}|} \tag{4.23}$$

where $\mathbf{n}$ is the surface normal in this equation. It can be normalized by help of the vector length

$$\widetilde{\mathbf{n}} = \frac{\mathbf{n}}{|\mathbf{n}|} \tag{4.24}$$

With this normalization, the wall adhesion angle or so called apparent contact angle, θ_w, between fluid and wall can be introduced with the following formula:

$$\widetilde{\mathbf{n}} = \widetilde{\mathbf{n}}_\mathbf{w} \cos\theta_w + \widetilde{\mathbf{t}}_\mathbf{w} \sin\theta_w \tag{4.25}$$

where $\widetilde{\mathbf{n}}_\mathbf{w}$ and $\widetilde{\mathbf{t}}_\mathbf{w}$ are the unit vectors normal and tangential to the wall, respectively. In the absence of other forces (such as no flow), θ_w will be identical to the static contact angle.

4.3 Governing equations for interfacial mass transfer

As phase exchange has also to be considered, the relevant governing equations (void fraction equation and mass conservation equation) should be modified by source terms:

$$\frac{\partial \rho}{\partial t} + \nabla \cdot \rho \mathbf{U} = S \tag{4.26}$$

The source S is the mass added to the liquid phase from the gas phase ($\dot{m}_{gl}$) due to dissolution of gas into liquid as well as the evaporation of liquid species to the gas ($\dot{m}_{lg}$).

$$S = \dot{m}_{gl} - \dot{m}_{lg} \tag{4.27}$$

Diffusion of liquid into gas is very small compared to gas dissolution therefore mass transfer from liquid to gas is not considered, $\dot{m}_{lg}$ is zero.

$$S = \dot{m}_{gl} \tag{4.28}$$

It should be noted that the liquid density does not change after the mass transfer since the influence of the gas species on liquid density is assumed to be very small.

The void fraction for the gas phase is consistently:

$$\frac{\partial f_g}{\partial t} + \nabla \cdot f_g \mathbf{U} = \frac{S}{\rho_g} \tag{4.29}$$

The volume fraction equation is solved for the liquid phase (continuous phase); the gas phase (dispersed phase) volume fraction is computed based on the following constraint:

$$f_g = 1 - f_l \tag{4.30}$$

The following species equations are solved for the liquid phase as well as at interface:

$$\frac{\partial}{\partial t}(\rho_l . f_l . M_i^l) + \nabla \cdot (\rho_l . f_l . M_i^l \vec{U}) = -\nabla \cdot f_l . \vec{J_i^l} + \dot{m}_{gl}^{ij} \tag{4.31}$$

In Equation 4.31 i denotes gas bulk and j is the dissolution of gas species in liquid. $\dot{m}_{gl}^{ij}$ is the mass transfer source between species gas and the liquid mixture from gas phase to liquid phase.

$$\dot{m}_{gl}^{ij} = \frac{-\nabla C D_l A}{V} \tag{4.32}$$

In Equation 4.32 A is the interfacial area and it can be calculated for each cell by multiplication of cell volume with the magnitude of the void fraction gradient:

$$A_{cell} = \sqrt{\left(\frac{\partial f}{\partial x}\right)^2 + \left(\frac{\partial f}{\partial y}\right)^2 + \left(\frac{\partial f}{\partial z}\right)^2} V_{cell} \tag{4.33}$$

It is important to know that the calculation of $\dot{m}_{gl}^{ij}$ at interface cells is only activated as long as the void fraction of the liquid phase is greater than 0.05 to keep the convergence. Otherwise the concentration gradient approaches infinity since the discretization length approaches easily zero without the liquid void fraction restriction. The gradient of concentration in Equation 4.32 is calculated by

$$\nabla C = \frac{C_{sat} - C_{dis}}{\Delta X} \tag{4.34}$$

where C_{sat} is the saturation concentration, C_{dis} is the dissolution concentration in liquid phase, and ΔX is the missing discretization length. Determination of the ΔX is based on the two alternative numerical concepts and they are explained in Figure 4.3. ΔX is calculated only in liquid phase when f_l is not equal to zero.

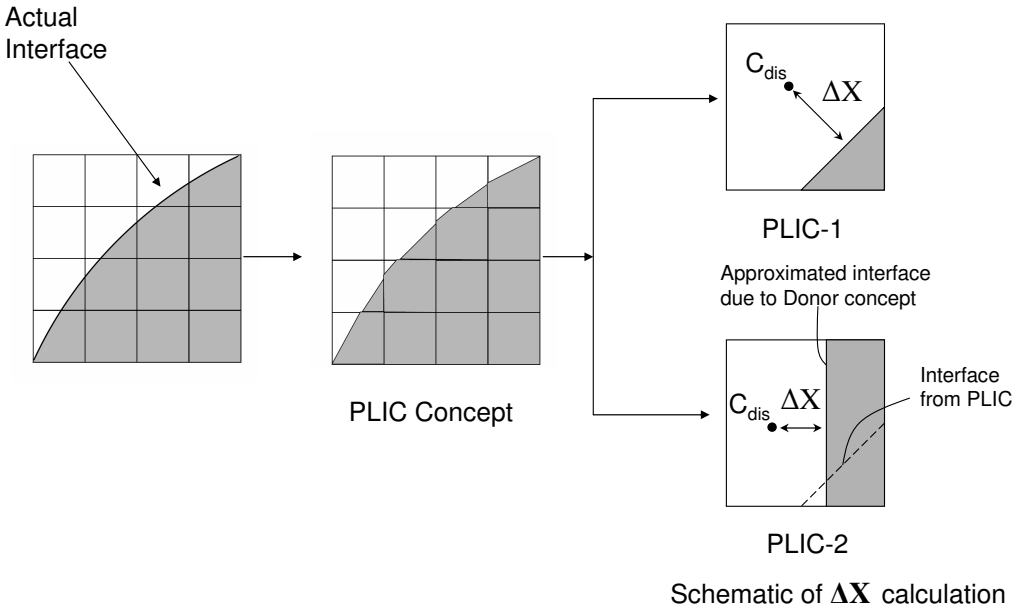

Figure 4.3: 2-D schematic of a real interfacial surface, the PLIC scheme applied in the VOF method as well as the two concepts tested for determination of the diffusion length (ΔX)

In the numerical concept of PLIC-1 ΔX is near to the reality due to the usage of the surface reconstruction with help of neighbor interface cells while in the concept of the PLIC-2 the discretization length is only approximated (fluid surface is assumed parallel to a certain interface cell).

In the PLIC-1 concept only the normal vector of the gas-liquid interface and the f-value are provided from the Fluent code to calculate ΔX. In order to identify the position of the interface in the cells the new code written in this work iterates. Starting with an initial point in the cell middle, the phase volumes are calculated with the normal vector and this initial point as a position of the interface plane. These phase volumes are compared with the f-value. If the phase volumes are not consistent to f, the position of the plane is changed until this criteria is fulfilled.

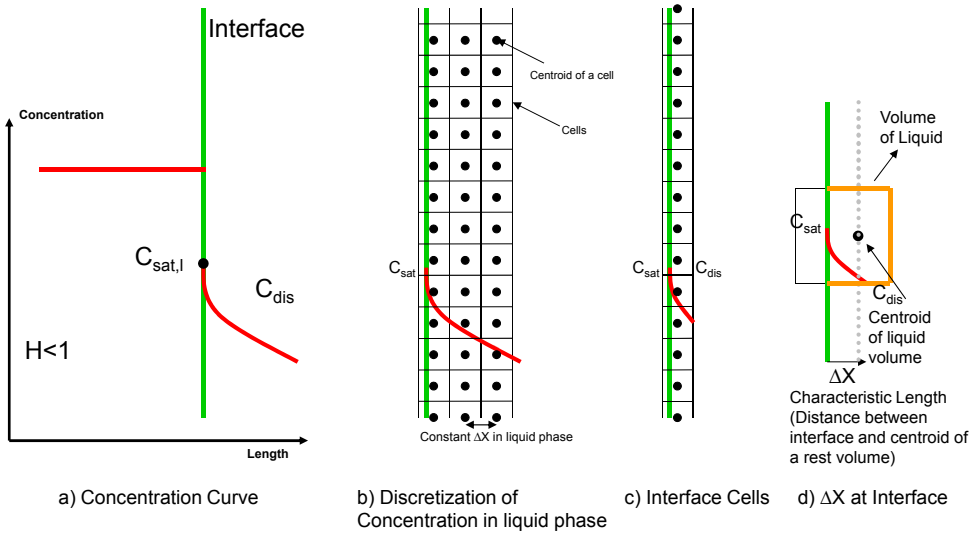

Figure 4.4: Discretization of numerical mass transfer at interface in detail

By this ΔX is determined. Determination of the discretization length based on the PLIC-2 conception is easier than in the PLIC-1 concept. Since cubic cells are applied in this work, the individual phases are separated into cuboids sections and the normal vector is rectangular to the one of the cell walls. The mathematics needed for the calculations of ΔX are described in more detail in the following subsections.

Like the study of Sato et al. [45] the saturation concentration at the interface cells was used as a boundary condition. In order to implement a discretization of the concentration at interface cells the discretization liquid length (distance between interface and centroid of the liquid volume) must be calculated using the two numerical concepts.

Figure 4.4 shows the method of discretization in gas / liquid systems. Since Sato's et al. [45] approach for concentration boundary at interface is applied, the missing part in the code is discretization of the concentration at interface cells as shown in Figure 4.4-d. Using two available data (normal vector of the gas / liquid interface and void fraction (f)) from the VOF code the discretization length ΔX between gas / liquid interface and centroid of the liquid volume can be determined based on the two suggested numerical concepts (PLIC-1 (Piece

Linear Interface Capturing); PLIC-2).

4.3.1 Determination of discretization length with PLIC-1 numerical concept in 3-D simulations

In this part implementation of the PLIC-1 concept will be presented in detail. Details of PLIC-2 can be found in section 4.3.2.

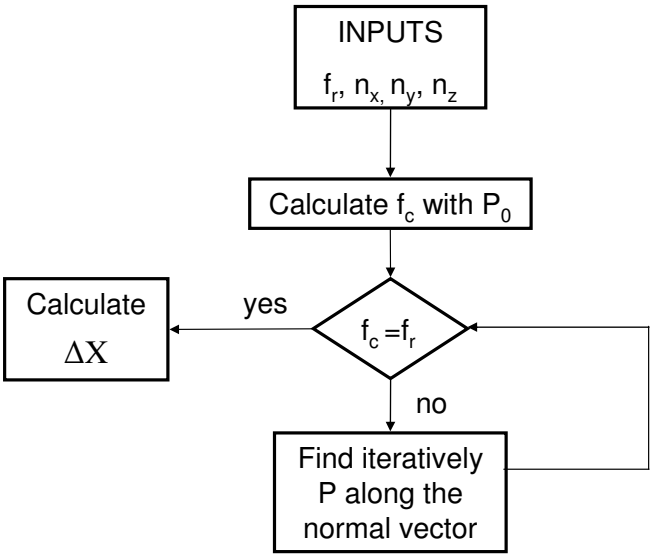

Figure 4.5: Flowchart of the ΔX calculation in the PLIC-1 concept

The programming and verification of the calculation of the method was done in C code. The flowchart of the program is shown in Figure 4.5. In the PLIC-1 concept the normal vector of the gas-liquid interface and the f-value from Fluent code are applied to calculate ΔX. f_r is f value delivered from Fluent, and f_c is f value calculated iteratively in the flowchart. The iteration is necessary to identify the position of the interface in the cells. Demonstration of iteration progress is shown in Figure 4.6. The cell middle is used as point (P_0) of the interface plane during the initialization to calculate a first phase volume of the gas or the liquid respectively. The phase volume is compared with the f-value. If the phase volume deviates from f, the position of the plane is changed along the normal vector until this criteria is fulfilled. Then ΔX is calculated.

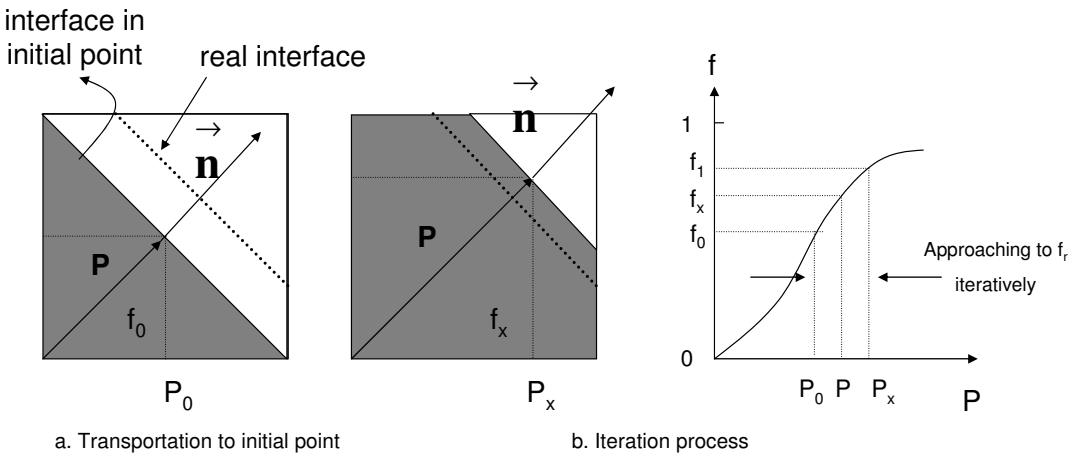

Figure 4.6: Demonstration of iteration progress to determine the position of the interface plane with interface normal vector and a starting point for calculation in the cell middle point P_0

In the subroutine the cell edge points in the global coordinates have to be handled. These 8 points on the cells (in x, y, z Cartesian coordinates) are written in a matrix 8x3 form. An example is shown in Figure 4.7. For this specific example the matrix is:

$$\text{Edge Points}[i][k]= \begin{bmatrix} 0 & 1 & 1 & 0 & 0 & 1 & 1 & 0 \\ 0 & 0 & 1 & 1 & 0 & 0 & 1 & 1 \\ 0 & 0 & 0 & 0 & 1 & 1 & 1 & 1 \end{bmatrix} \quad 0 \leq i<8,\ 0 \leq k<2;$$

In order to allow an easier calculation of ΔX a transformation of the coordinates was used like in [66, 67]. In this transformation the normal vector was applied as a new (local) z' direction. By this approach it is not necessary to calculate the cut points of the interface plane with the cell in each iteration.

A new normal vector was also introduced in the calculation method for further simplification. This new vector $\vec{N}$ has unit length:

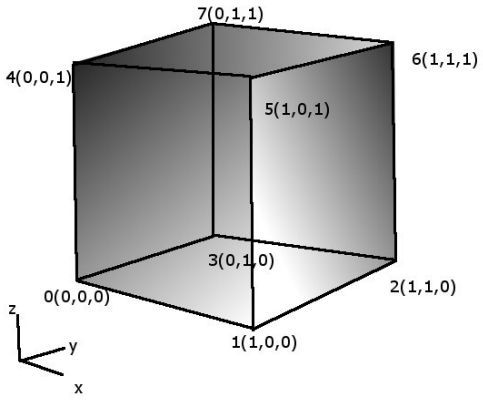

Figure 4.7: Example of a cubic cell for explaining the edge point matrix for calculation of ΔX

$$\vec{N} = \frac{\vec{n}}{|\vec{n}|} \tag{4.35}$$

$\vec{T}$ and $\vec{S}$ vectors were defined to represent the new $y^{'}$ axe, $x^{'}$ axe according to the right hand rule (see Figure 4.8) and to have a full transformation matrix.

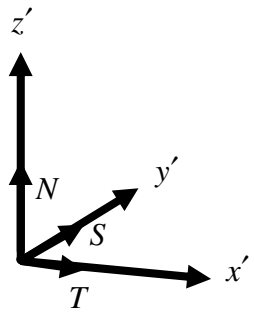

Figure 4.8: Definition of the transformation vectors of the coordinate system

$\vec{T}$, $\vec{S}$ was defined randomly on the interface plane and calculated by help of Equation 4.36.

$$\vec{T} = \vec{S} \times \vec{N} \tag{4.36}$$

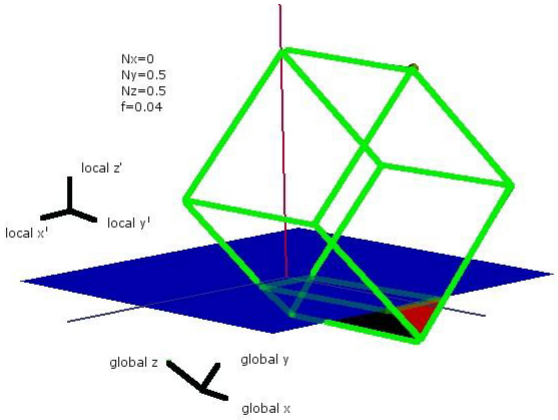

Figure 4.9: Example of a transformation of global into local coordinates and calculation of the cut volume for determination of ΔX

Figure 4.9 further explains the strategy of the calculation for the phase volumes. The volume of the cell below the interface plane represents the liquid volume (cut volume) whereas the volume above the interface plane represents the gas volume. The interphase plane is shifted during the iteration along the $z^{'}$ axis.

In order to compute the void fraction of the interface cells, the cut volume needs to be determinated. The cut volume as well as the centroid of the cut volume were calculated by a triangle prism methodology [66, 67]. Each cut volume is divided to triangle prisms as it is demonstrated in Figure 4.10.

Volume of triangle prism is calculated using the formula:

$$V = Ah\frac{1}{3} \tag{4.37}$$

Both, surface A and height h are a function of the edge points P_0, P_1, P_2, P_3 of the triangle prism (see Figure 4.11).

h is calculated in two steps. In the first step three vectors $\vec{k}$,$\vec{j}$,$\vec{d}$ are defined due to the triangles prism points:

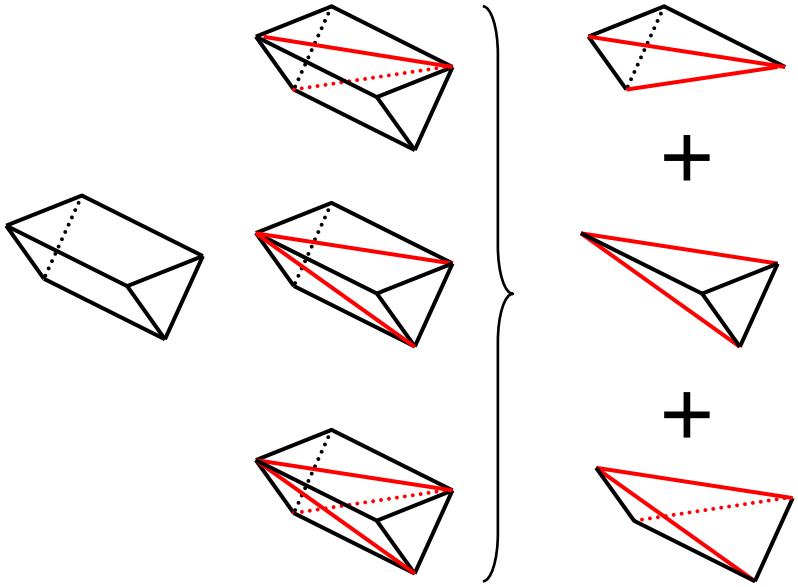

Figure 4.10: Division of the cut volume by triangle prisms in the course of determination of ΔX

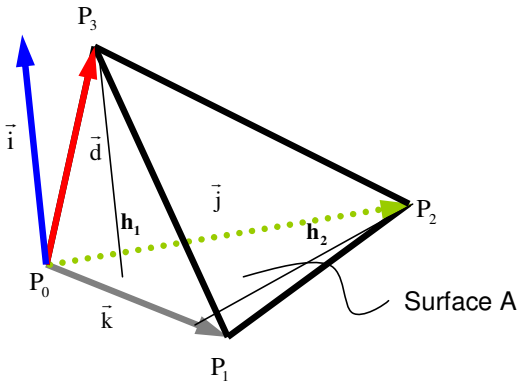

Figure 4.11: Definition of the prism vectors for determination of the prism height h in the routines for determination of ΔX

$$\vec{k} = P_1 - P_0 \tag{4.38}$$

$$\vec{j} = P_2 - P_0 \tag{4.39}$$

$$\vec{d} = P_3 - P_0. \tag{4.40}$$

The vectoral multiplication gives the normal vector $\vec{i}$

$$\vec{i} = \vec{k} \times \vec{j} \tag{4.41}$$

After normalization of $\vec{i}$ via;

$$\vec{I} = \frac{\vec{i}}{|\vec{i}|} \tag{4.42}$$

$\vec{I}$ can be used in a second step to determine h using scalar vectoral multiplication:

$$h_1 = \vec{d} \cdot \vec{I} \tag{4.43}$$

The surface area (A) is calculated as follows:

$$A = |\vec{k}|h_2/2 \tag{4.44}$$

The sum of V_i of triangle prism volumes gives the cut volume V;

$$V = \sum_{i=0}^{n-1} V_i \tag{4.45}$$

ΔX is the length between the centroid of the cut volume to the interface plane. In order to find the centroid point of the cut volume, it is necessary to find the centroid of the triangles of the prism and then to find the centroid of prism volumes first.

As it is shown in Figure 4.12, vectors $\vec{k}$,$\vec{c}$ are the edges of the surface A and $\vec{m}$ is the vector which divides $\vec{c}$ into two equal parts.

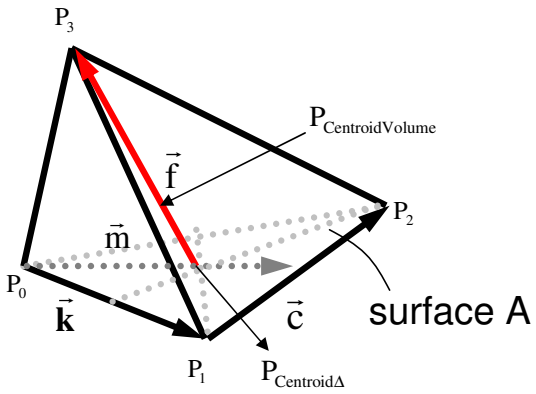

Figure 4.12: Schematic for determination of the centroid point of a triangle prism in the routines for determination of ΔX

$$\vec{c} = P_2 - P_1 \tag{4.46}$$

P_{12} is the middle point of $\vec{c}$ and can be calculated according to

$$P_{12} = (P_2 + P_1)/2 = P_0 + \vec{k} + \vec{c}/2 \tag{4.47}$$

$$\vec{m} = P_{12} - P_0 \tag{4.48}$$

The centroid of the triangle is then calculated by

$$P_{Centroid\Delta} = P_0 + 2/3\vec{m} = P_0 + 2/3(\vec{k} + \vec{c}/2). \tag{4.49}$$

$\vec{f}$ is the vector between the centroid of the triangle and P_3 (see Figure 4.12):

$$\vec{f} = P_3 - P_{Centroid\Delta} \tag{4.50}$$

The centroid of the triangle prism is

$$P_{CentroidVolume} = P_{Centroid\Delta} + 1/4\vec{f}. \tag{4.51}$$

By replacement it becomes:

$$P_{CentroidVolume} = \frac{3}{4}P_{Centroid\Delta} + \frac{1}{4}P_3. \tag{4.52}$$

The centroid vector of cut volume $\vec{V}$ can be calculated further from the centroids of the triangle prisms $\vec{V_i}$ using:

$$\vec{V} = \frac{1}{V}\sum V_i\vec{V_i}. \tag{4.53}$$

4.3.2 Determination of discretization length with PLIC-1 numerical concept in 2-D simulations

In 2-D the calculation of ΔX is much simpler since no triangle prisms have to be calculated. However the flowchart of the program is the same as it is shown in Figure 4.5.

Again, the interface plane (line) is transferred to an initial point in the cell middle, and the phase volumes are calculated with the normal vector (see Figure 4.6). The position of the plane is changed until the phase volumes are consistent to the phase ratio f.

The cell boundaries are defined with linear equations of the following type:

$$ax + by = c \tag{4.54}$$

wherein the coefficients are exemplary shown in Table 4.1.

Coefficients	a	b	c
for x=0	1	0	0
for x=1	1	0	1
for y=0	0	1	0
for y=1	0	1	1

Table 4.1: Coefficients for linear equations of cell boundaries in 2D

The interface can be defined by a point and a normal vector in 2D. If P_0 is taken as the initial point, the following equation represents the interface plane equation:

$$n_x(x - P_{x,0}) + n_y(y - P_{y,0}) = 0 \tag{4.55}$$

It can be rewritten as

$$n_x x + n_y y = d \tag{4.56}$$

with d=$P_0(n_x + n_y)$.

Using the Cramer's rule in matrix form, which is used for the solution of a system of linear equations, the cut points x, and y at cell boundaries can be found with the set of the following equations:

$$\begin{bmatrix} a & b \\ n_x & n_y \end{bmatrix} \begin{bmatrix} x \\ y \end{bmatrix} = \begin{bmatrix} c \\ d \end{bmatrix} \tag{4.57}$$

$$x = \begin{vmatrix} c & b \\ d & n_y \end{vmatrix} / \begin{vmatrix} a & b \\ n_x & n_y \end{vmatrix} \tag{4.58}$$

$$y = \begin{vmatrix} a & c \\ n_x & d \end{vmatrix} / \begin{vmatrix} a & b \\ n_x & n_y \end{vmatrix} \tag{4.59}$$

Due to the coordinate transformation there are only 4 cases in 2-D cases as it is explained in Figure 4.13. The polygon of one phase in the cell is defined by its edge points with coordinates (x_i,y_i), i=0 to Z-1. The last edge point (x_Z,y_Z) is the same as the first. The following equation can be used for the area calculation:

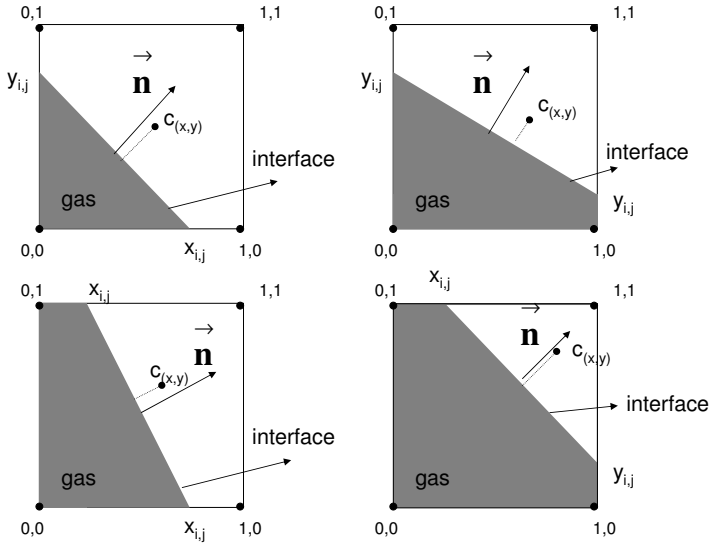

Figure 4.13: Different cases of interface position in 2D with consequences on the phase shape (polygon type).

$$A = \frac{1}{2}\sum_{i=1}^{Z-1}(x_i y_{i+1} - x_{i+1} y_i). \tag{4.60}$$

The centroid c of the rest of the liquid area is also calculated via the polygon

assuming equal density in the cell. Then following equations are used for the calculation of center points in x and y coordinates:

$$c_x = \frac{1}{6A}\sum_{i=1}^{Z-1}(x_i + x_{i+1})(x_i y_{i+1} - x_{i+1} y_i) \tag{4.61}$$

$$c_y = \frac{1}{6A}\sum_{i=1}^{Z-1}(y_i + y_{i+1})(x_i y_{i+1} - x_{i+1} y_i) \tag{4.62}$$

4.3.3 Determination of discretization length with PLIC-2 numerical concept

Determination of the discretization length based on PLIC-2 is easier than the PLIC-1 concept. Since cubic cells were used for the simulations the individual phases are separated into cuboids sections and the normal vector is rectangular to one of the cell walls. Thus the ΔX can be calculated according to following equation for a unit cell:

$$\Delta X = \frac{1-f}{2}.L \tag{4.63}$$

Here the L, corresponds to mesh size, is the characteristic length.

Chapter 5

Two Phase Flow Results

5.1 Computational domains for two phase flows

If hydrogen and nitrobenzene are premixed and subsequently fed to a reactor, segregation and maldistribution of gas and liquid can occur. To avoid a high gas to liquid ratio with annular flow and lower mass transport due to reduced interfacial area and thus to increase the residence time of the liquid at constant reactor volume (higher conversion), sequential feeding of hydrogen in the microreactor alternatively can be applied (see Figure 5.1). By this approach it is further possible to control the bubble size and the flow regime.

Furthermore hydrogen addition and consumption can be adjusted to each other and the space time yield in the reactor can be maximized without loosing overall stoichiometric conditions and saturation of the liquid with pure reactant gas.

The catalyst concept can be two-fold: wall might be coated with catalyst or the microreactor can be filled with catalyst particles. Advantages and disadvantages of the different catalyst integration methods are shown in Table 5.1.

Since the wall coated catalyst has more numerical and experimental advantages, this integration method was selected for the investigations in this thesis. Moreover Bauer et al. [68] studied the performance of monolith reactors with different flow regime (Taylor flow and film flow) and compared it to trickle bed reactors. The authors found that the monolith reactor has more advantages than

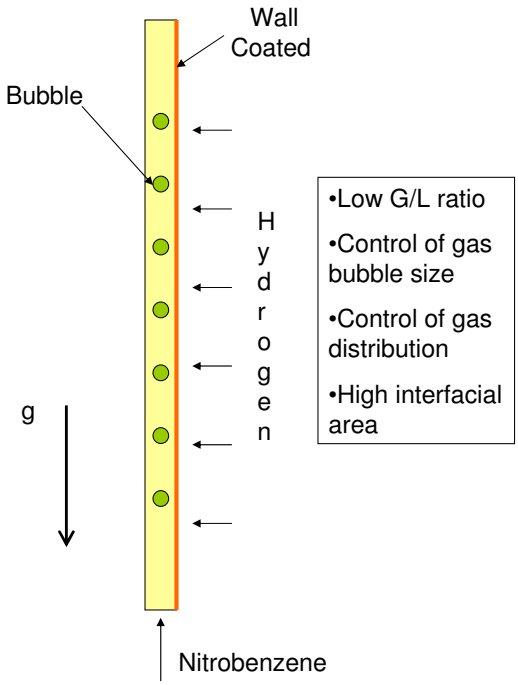

Figure 5.1: Scheme and advantages of sequential feeding of gas in microreactor

Catalyst wall coated	**Filling with catalyst particles**
Industrial Advantages and Disadvantages	
+ Low amount of highly active catalyst	+ Catalysts is changeable in case of deactivation
- Microstructured elements need to be changed in case of irreversible deactivation	+ Standard catalyst is applicable
Numerical Advantages and Disadvantages	
+ Chemical reactions take place on effectively cooled wall	- Catalyst particles are typically too small (dp=0.04 mm) to be resolved as individual particles
+ Relatively easier to verify simulation	- High calculation time
Experimental Advantages and Disadvantages	
+ Physical and chemical phenomena can eventually be observed with optical access to the microchannel.	- Physical and chemical phenomena can not be observed easily because of catalysts particles in microreactor.

Table 5.1: Advantages and disadvantages of different catalyst integration methods in microreactors

the trickle bed reactors and that film flow gives higher conversion per pass at the same reactor length in monolith reactors. Similar conclusions can be found in other articles [68, 69]. Monolith reactors possessed a three time higher productivity while using four times fewer catalyst.

Figure 5.2 shows the microstructured reactor applied in the laboratory in this thesis. Figure 5.3 shows a scanning electron microscope (SEM) picture of the gas inlet into the microchannels. For the numerical studies two different diameters of gas inlet have been considered: 40 μm, 100 μm.

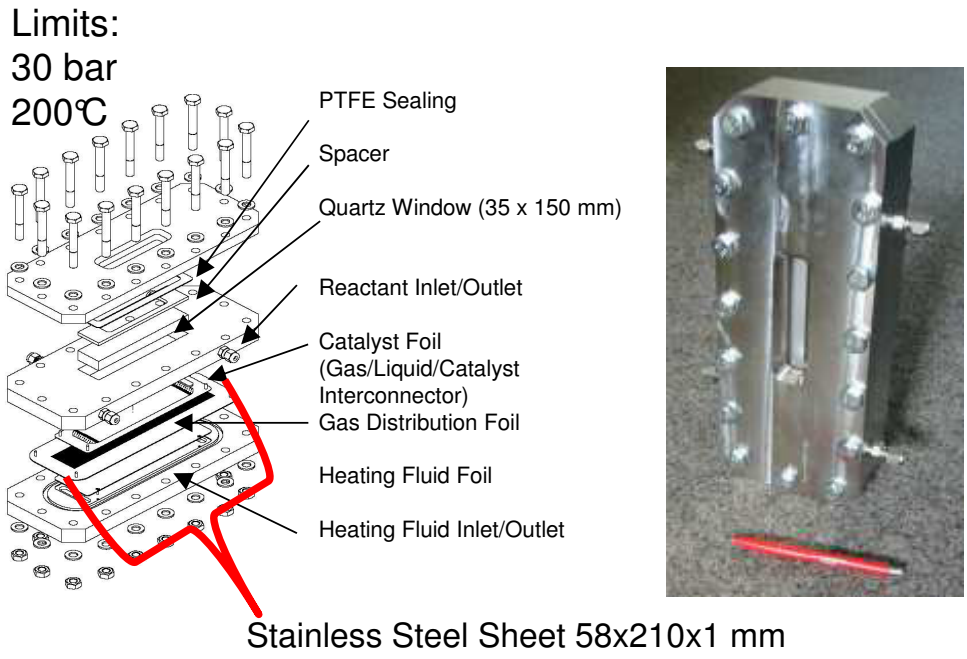

Figure 5.2: Exploded view (CAD) and assembled test reactor

A relevant computational domain was chosen in order to minimize computational time for investigating the effects on bubble formation in the microreactor.

Figure 5.4 shows the computational domain representing a part of one of the microchannels inside the microchannels inside the microreactor. The diameter of the hydrogen inlet is 40 μm and is modelled as a cylinder. The length of the hydrogen inlet hole is 0.1 mm. The dimension of the computational domain is 2.92, 0.4, and 1 mm in the z-, y-, and x-direction, respectively. Two mid-planes

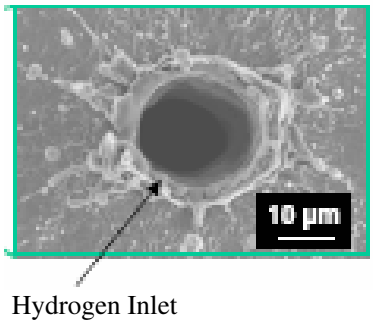

Figure 5.3: Hydrogen inlet into the microchannels of the stainless steel inside the microreactor

are also shown in Figure 5.4 - the so called YZ and YX planes.

The computational domain consists of two geometries; a rectangular channel and a cylindrical inlet. In term of mesh creation in transition between these two different geometric forms a structural mesh method was chosen since it gives a better convergence. For the rectangular channel the interval mesh size is 0.02 mm in each direction (x, y, z). This corresponds to 50 x 20 x 146 structural hexahedral cells in the computational domain. For the hydrogen inlet 12 mesh cells on the inlet hole cross-section and 5 mesh along the 0.1 mm length are used. A "Pave Type" mesh was applied to the inlet face of hydrogen gas and a structural mesh was used along the length of the hydrogen inlet. To prevent and minimize a divergence at the junction of the hydrogen inlet and the rectangular channel a mesh combination and consistence between the computational domain of the hydrogen inlet and the rectangular channel was provided. As the surface tension force might be relevant for the simulations, a quadrilateral and hexahedral mesh structure was applied according to recommendations of the ANSYS FLUENT user guide [70]. The QUICK scheme for momentum discretization was applied since it is more accurate on structured grids aligned with the flow direction. Since the simulation is transient, a PISO scheme was used for pressure-velocity discretization.

The applied hydrogen mass flux amounts to 2.56 kg/m^{2}s in the y-direction (referring to the cross-section of the inlet hole), and nitrobenzene is supplied

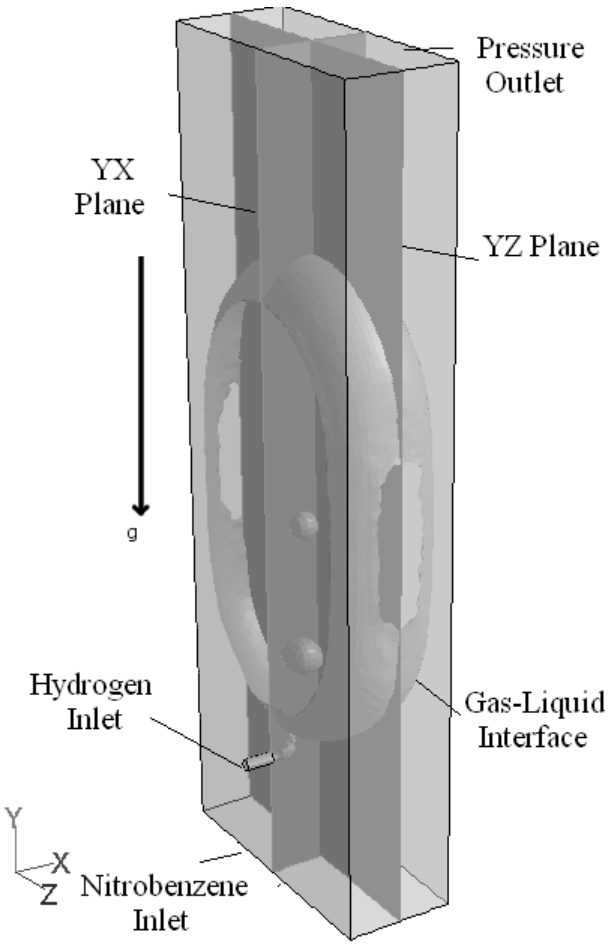

Figure 5.4: Computational domain for two phase flow investigations with respect to the mixing zone

with a 1.14 kg/m^{2}s mass flux in the z-direction (referring to the rectangular inlet surface at the channel bottom). These values are chosen for the desired ratio of reactants (stoichiometric conditions) and experimental circumstances for the validation of the hydrodynamic simulations with the specific gas-liquid-solid system. Average velocities at the inlets are about 5 m/s and 0.001 m/s for hydrogen and nitrobenzene, respectively, assuming operating conditions of 120^0 C degree and 10 bar for the hydrogenation reaction.

5.2 Results of two phase flows

5.2.1 Influence of surface tension, flow direction, inlet velocity, and wettability on flow regime

This section addresses the major influences on the generation of bubbles in a microstructured reactor since the mixing and the reaction zone is combined in the reactor approach. One of the main interests concerning the generation is the shape of the bubbles since bubble train flow would yield the highest interfacial area inside the microreactor. Another focus is also on how to handle bubble detachment in the microreactor and how to avoid coalescence. All together also provides efficiently design of gas-liquid reactors.

The following parameters were chosen for investigation in terms of bubble formation:

1. Flow direction of inlet
2. Surface tension effect
3. Influence of gravity
4. Co- or counter-current flow concept
5. Critical inlet liquid velocity to create bubble train flow

Investigation of influence of wettability will be reported separately in Chapter 5.2.2.

The following restrictions and assumptions for the computational domain have been made:

- Non-slip wall condition.
- Wall roughness is neglected.
- Both fluids are incompressible (densities are almost constant at 120 ^{0}C and 10 bar over the short channel length simulated).

- Contact angle between gas and liquid varied in steps between 15^0, 90^0, and 165^0 to cover a set of different situations.

Table 5.2 shows physical properties of nitrobenzene and hydrogen at 120^0C and 10 bar. No influence of system pressure has been implemented for the physical properties in the microreactor, and the maximum pressure drop in the computational domain is very small with respect to system pressure.

Hydrogen viscosity	1.065x10^{-05} Pa.s
Hydrogen density	0.618 kg/m^3
Hydrogen mass flow flux	2.56 kg/m^2s
Nitrobenzene viscosity	61.3x10^{-05} Pa.s
Nitrobenzene density	1101.4 kg/m^3
Nitrobenzene mass flow flux	1.14 kg/m^2s
Surface Tension Coeeficient	0.0325 N/m

Table 5.2: Physical properties of the system Nitrobenzene -Hydrogen at 10 bar and 120^0C (see Appendix A for the calculations)

In terms of reliability and thus correct description of the interface geometry by the applied code, it is possible to rely on own previous studies [35, 71]. It was found that for determination of the interface between gas and liquid phases, the method of VOF (volume-of-fluid) in combination with the geometrical reconstruction method to trace interface between phases is validated against experiments.

Influence of surface tension, buoyancy, inlet angle and flow direction are shown in Figure 5.5 calculated for 10 milliseconds after start of hydrogen supply with a static contact angle (SCA) of 15^0. Influence of surface tension is very important, as shown in Figure 5.5-A. The interface lines are different for the "normal" case, i.e. with surface tension, in comparison to calculated interface lines with zero surface tension. This is coherent with the relevant dimensionless numbers. Relevant numbers are:

Capillary number

$$Ca = \frac{\mu_l U_{bub}}{\sigma} = 4.10^{-4}$$

Weber number

$$We = \frac{\rho_l L U_{bub}^2}{\sigma} = 0.012$$

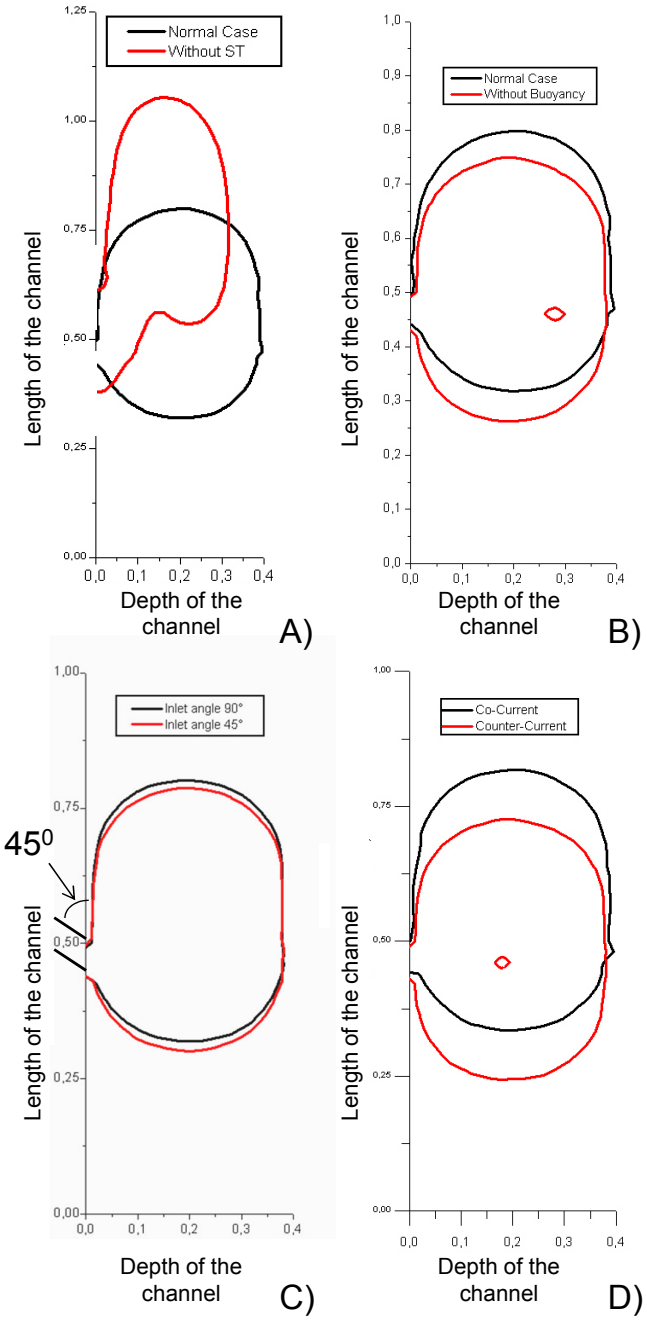

Figure 5.5: Gas-liquid interface shape in YX plane (3D); A: Influence of surface tension, B: Influence of buoyancy, C: Influence of inlet angle (between nitrobenzene and hydrogen), D: Influence of nitrobenzene flow direction

Since both numbers are smaller than 1, surface tension can not be neglected [72]. The buoyancy effect is shown in Figure 5.5-B. The "normal" case (gravity against flow direction, i.e. downward) is strongly different to the case in which gravity is zero in the computations. A pushing effect to the bubble by the liquid flow is recognizable due to a slightly higher vertical position of the bubble without buoyancy. To understand whether there is an influence of the inlet direction of hydrogen into the microreactor on the flow field, two different inlet angles (between hydrogen and nitrobenzene flow direction) have been simulated. A 45^0 angle and a 90^0 angle are compared in Figure 5.5-C. The Figure shows that the inlet angle does not play a significant role in the computations. This might be different for other velocity ratios between hydrogen and nitrobenzene. The Figure 5.5-D shows the comparison of co- and counter-current flow of hydrogen and nitrobenzene. The bubble shape in counter-current flow is different to those in co-current flow. The extent of influence of the flow direction is similar to the influence of buoyancy. In some of the above simulations very small liquid drops in gas phase can be observed (Figure 5.5-D). It is assumed that the reason is numerical diffusion, i.e. a shortcoming of the applied time step size in the gas entry region. The velocity is rather high in that region.

In order to get smaller bubbles an increase in nitrobenzene mass flow is possible. However, this is not desired for the chemical reaction since liquid flow has to be recycled at high liquid flow rate in order to complete the reaction. Nevertheless, to investigate the effect, an the increase of the liquid flow rate from stoichiometric conditions to a factor of 10, 100, and 1000 higher liquid reactant flow rate at constant gas flow rate was simulated (Figure 5.6). At a factor of 100 a critical mass flow rate is obtained to detach the bubble and obtain bubble train flow. One option to keep the stoichiometric balance (maintaining both flow rates) is apply an extra force on the liquid, for example by a pulsation (sinusoidal). This has, however, not been simulated.

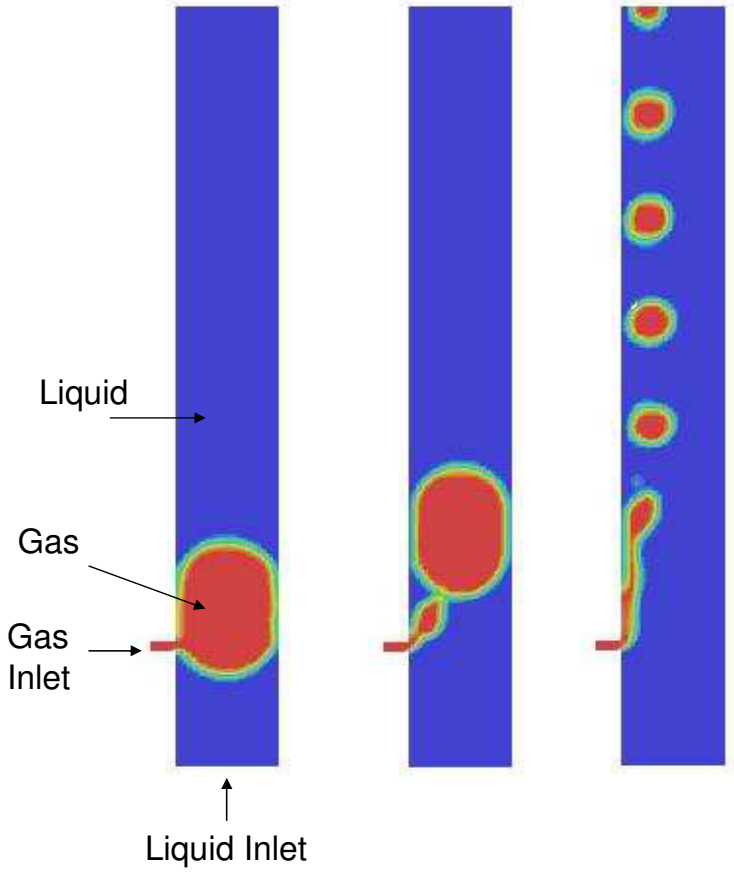

Figure 5.6: Lateral views of bubble generation in a microchannel at 10 milliseconds. From left to right: Liquid mass flow rate is increased by a factor of 10, 100, and 1000 compared to conditions in Table 5.2

5.2.2 Numerical investigation on dependence of flow regime on static contact angle

Since the static contact angle plays a big role to determine the fluid regime in microreactors [41] the influence of the static contact angle is discussed in this section in more detail.

Figure 5.7 shows three cases of computations for generation of bubbles at the hydrogen inlet with different contact angles: 15^0, 90^0 and 165^0. All computations represent a time of 10 ms after start of hydrogen feeding. The contact angle, which is a result of surface forces, is strongly influenced by the channel material.

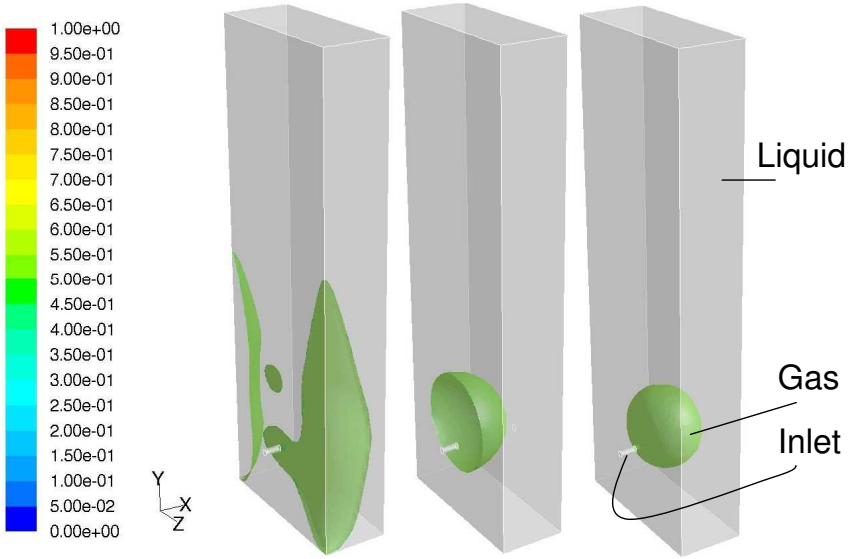

Figure 5.7: Influence of static contact angle on bubble formation at hydrogen inlet for conditions according to Table 5.2. 165 ^{0}, 90 ^{0}, 15^0 contact angle from left to right

Because the results obtained with 15^0, 5^0 and 0^0 are equal, a static contact angle of 15^0 is used to represent the bubble shape for all lower contact angles. Fluids with high contact angles of $\Theta > 90\ ^0$, i.e. poor wettability, lead to a situation where the bubble/gas touches the channel walls, which can be verified by experiments from literature [62]. Small contact angles of $0^0 < \text{SCA} < 90^0$ allow wetting of the channel walls and result in semicircular bubbles at the inlet. These findings are similar to those by Takamasa et al. [62].

The strong influence of the contact angle is due to code, it can establish a constant contact angle between wall and fluid by Equation 4.25.

Since the liquid flow velocity is low in all simulations the friction is not high enough to separate bubbles from the hydrogen inlet; the bubbles grow extremely large and a slug-annular flow is the prominent flow regime.

In the above simulations, the Reynolds numbers calculated with the diameter of the hydrogen inlet or the hydraulic diameter of the channel and the individual single phase properties, are 10.6 (Re_{H2}) and 1.02 (Re_{NB}) at the inlets of hydrogen and nitrobenzene, respectively. Under the assumption of laminar flow, the

channel length needed for fully developed flow, i.e. the minimum entrance length L_e, can be estimated by the formula

$$L_e = 0.06 Re D_h \tag{5.1}$$

where D_h is the hydraulic diameter [35]. In both cases, this length is shorter than the entrance length (hole length of the gas supply and liquid inlet length, respectively) in the simulations. This gives the confidence that none of the observed effects are induced by a non-fully developed flow before the mixing zone.

SCA (^{0})	165	90	15	12	5	0
$U_g(m/s)$	0.19	0.027	0.027	0.030	0.026	0.029
Ca	n.d.	n.d.	$3.4\ 10^{-4}$	$3.7\ 10^{-4}$	$3.7\ 10^{-4}$	n.d.

Table 5.3: Axial gas velocity and capillary number at various SCAs, determined at 10 ms and 100 ms simulation time respectively.

Table 5.3 shows the axial gas velocities at 10 ms and dimensionless capillary numbers at 100 ms after start of hydrogen dosing determined from mean cell values in the computations. Since the mean axial bubble velocity is higher directly after the initiation of the hydrogen flow, i.e. in the transient section (up to 10 ms, see also Figure 5.9), the dimensionless capillary number of the bubbles was calculated at a higher time after start of hydrogen dosing. The missing values have not been calculated due to the long computation time for 100 ms of dosing time and because the cases are expected to be similar to the others, especially for SCA 0^0. The velocities of gas bubbles with a contact angle of $\leq 90\ ^0$ are very similar whereas the velocity at $165\ ^0$ is much lower than in the other cases. It is possible to attribute this to the effect that gas starts moving along the wall under the liquid surface pressure.

Bubble formation in flow devices at constant physical properties is influenced by the ratio between the volumetric gas flow rate (Q_g) and the volumetric liquid flow rate (Q_l), the material of the channel, and geometrical properties [17, 65, 73]. In the computations, the ratio $Q_g : Q_l = 176$ was chosen for stoichiometry reasons. Larger ratios might lead to even longer and bigger bubbles [17]. As the Capillary number describes the dominant forces, which determine the shape of the bubble

and flow regime in the channels, it can be applied to explain the simulation results.

Since the Capillary numbers are very small the surface tension is dominant, and the acceleration forces on the bubble are small. Buoyancy is the primary acceleration factor since the liquid flow rate is very low.

In order to produce smaller bubbles, the ratio between the volumetric flow rates of gas and liquid should be close to unity [17]. The only parameter that can be controlled in the Capillary number is the mean bubble velocity, while viscosity and surface tension are physical constants for a given system. Bubble velocity can be increased by raising either the gas or the liquid inlet velocity. These measures will also result in an increase in the film thickness. In particular, enhancing the liquid velocity not only yields thicker films, but also causes a reduction of the bubble size. However, this results in non-stoichiometric conditions for the reaction under consideration.

Simulation results for static contact angles SCA $\leq 15^0$ are shown in Figure 5.8 at 100 ms dosing time on the YZ plane (at the middle of channel depth 0.2 mm) and on the YX plane (at the middle of width 0.5 mm, see section Numerical Approach on page 52, i.e. Figure 5.4) to explain the wetting issue in more detail.

The bubble views plotted in Figure 5.8 are determined from the curvature term (Equation 4.23 page on 32) and the surface tension force equation (Equation 4.22). Due to the combination with other forces in Equation 4.21, the curvature term and moving contact line on the wall can be changed by dynamic forces such as pressure driven flow and buoyancy forces. This means that code calculates a dynamic behaviour due to the force balance near the walls and not by a dynamic boundary condition such as a dynamic contact angle. Since the axial mean velocity at SCA 5^0 is slightly higher than at other SCAs, it is accelerated to a higher extent. Smaller contact angles provide higher film thickness (see Figure 5.8). On the YZ plane to the channel wall: 0.024 mm, 0.025 mm, and 0.026 mm film thickness are obtained at SCAs of 15^0, 12^0, and 5^0, respectively.

This thin film on the YZ plane corresponds to an apparent angle of 0^0; on the YX plane the gas touches the wall and yields an apparent contact angle greater than the static contact angle. The correct determination of the film thickness is a key issue for simulation of the reaction on the channel wall. Slightly higher

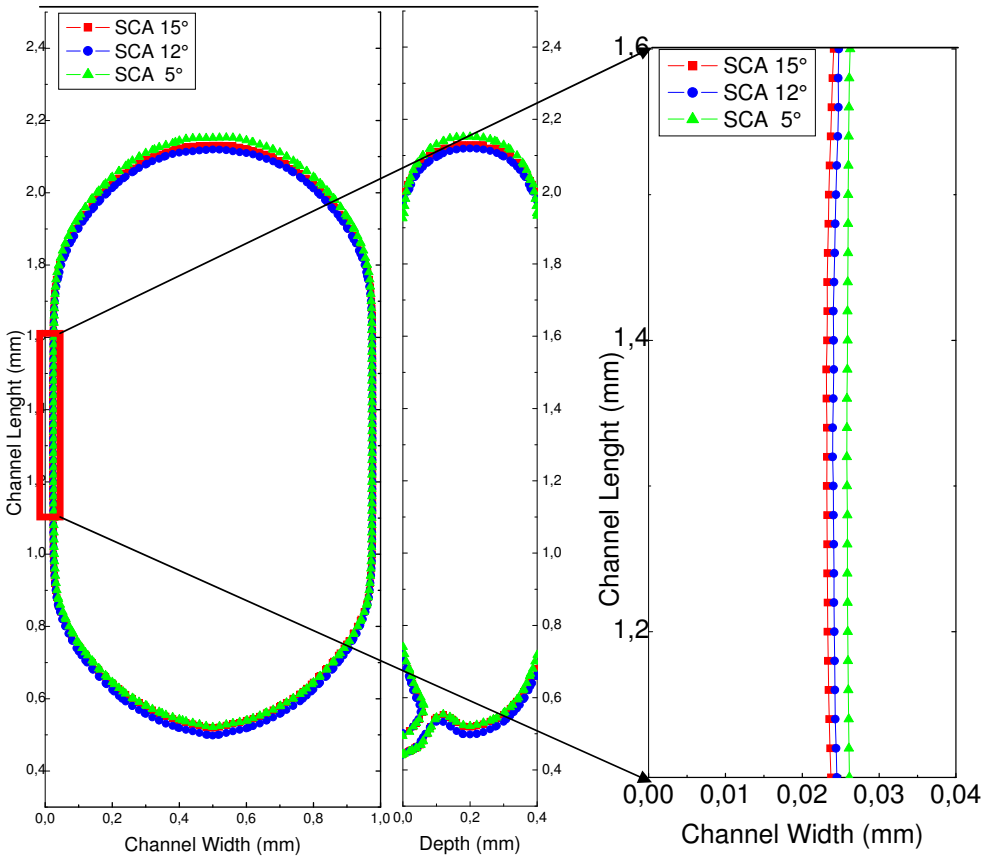

Figure 5.8: Bubble shapes with different SCA on the YZ (left) and YX (right) planes at 100 ms dosing time; detail of bubble shape on YZ plane at 100 ms dosing time. Conditions according to Table 5.2

values for SCA may yield also in a gas-solid contact at the YZ plane.

Figure 5.9 shows the velocity of the growing bubble in the y-direction at different contact angles. At starting conditions the velocity of the bubble certainly increases but then decreases with time with the trend to a constant value. In some cases it was observed that the bubbles reach a terminal axial velocity at about 140 ms. In a comparison of static contact angles $\leq 15^{0}$, the axial bubble velocities between 0 and 100 ms are almost the same; however, the SCAs play an important role with respect to the film thickness as shown in Figure 5.8.

The fact that there is no liquid film around the bubble at static contact angles smaller than 15^{0} is furthermore consistent with the values of the dimensionless

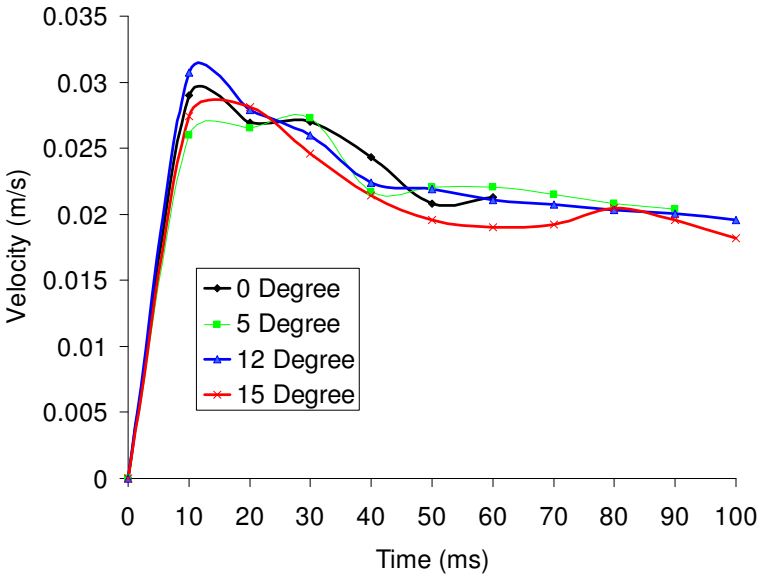

Figure 5.9: Mean bubble velocity in flow direction as function of time for SCAs $\leq 15^0$.Conditions according to Table 5.2

numbers Ca and We both being much smaller than unity. Unfortunately, there are no data available in literature for rectangular channels, which would be helpful to elucidate in experimental studies the thickness of the film normal to the channel wall. So far, video imaging systems are not able to determine the film thickness [74]. This issue may be explained by the study of Wong et al. [75]. They determined a pressure-velocity relation of bubble flow in polygonal capillaries for low values of the capillary number (Ca $\rightarrow$ 0). It is reported there that drag force dominates over gas motion and liquid flows through the corners of the channel. Wong et al. calls this behaviour a "leaky piston". Liquid flow cannot push the bubble, and instead, liquid flows around the bubble from the corners. However, such a behaviour would be undesired for the chemical reaction since a thin liquid film between the gas phase and wall provides higher rates of mass and heat transfer. Another issue to be solved in this circumstance is the relatively "coarse mesh" in the domain. Approximately one month is needed to solve one simulation for 100 ms with 7 parallel options in 8 CPUs with dual processors and 16 GB RAM. If a homogeneous half mesh interval (10 micron) size is implemented for higher resolution, about 8 months of CPU time would be required for each case

at the same conditions.

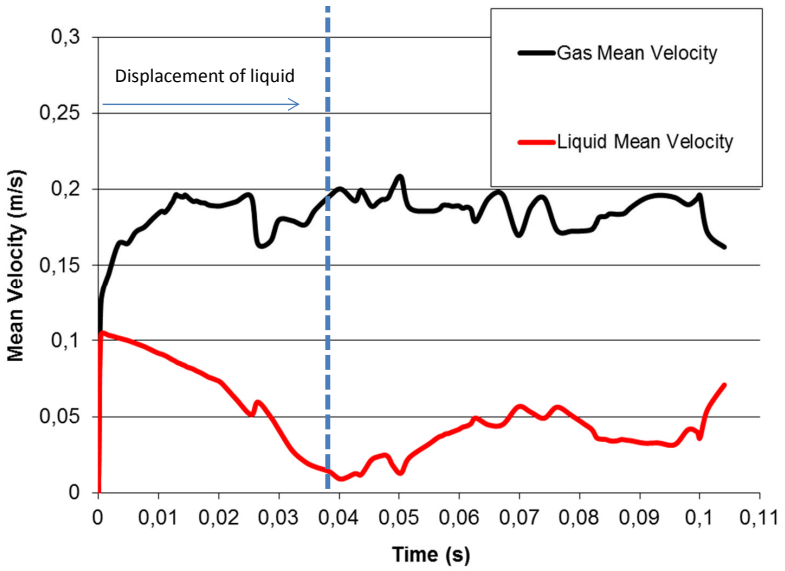

Figure 5.10: Mean velocities of gas and liquid for Case 1

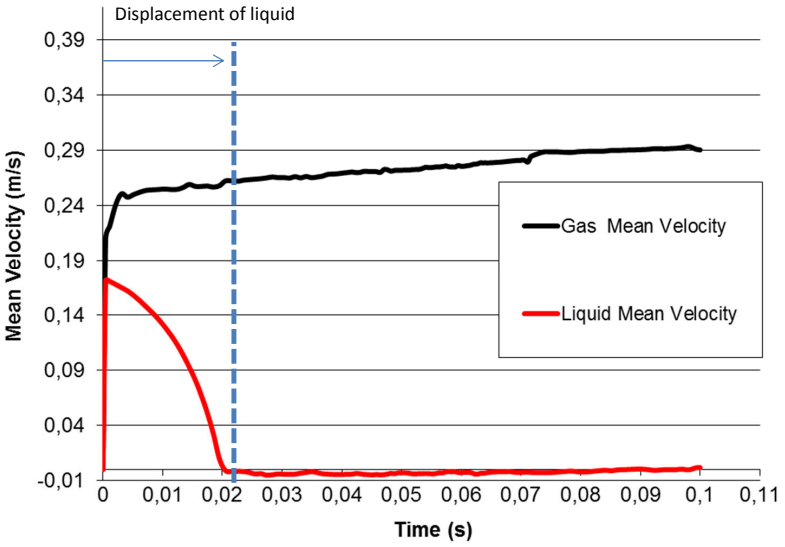

Figure 5.11: Velocities of gas and liquid for Case 2

	Hydrogen (ml/min)	Nitrobenzene (g/h)
Case 1	2.5	30
Case 2	5	2.5

Table 5.4: Flow rates of hydrogen and nitrobenzene applied for simulations of the flow field

5.2.3 Numerical investigation of flow regime

In order to investigate numerically multiphase flows, two extreme cases have been selected, namely Re_H= 2.41, Re_{NB}=22.4 for Case 1 and Re_H=4.82, Re_{NB}=1.94 for Case 2 (see Table 5.4 for information of the corresponding flow rates). The computational domain is similar as it is shown in Figure 5.4. The only changes are that the diameter of hydrogen inlet is 100 μm and the length of the channel is 6 mm. Physical values have been calculated at 1 bar and 110^0 C. The correlations for these calculations can be found in Appendix A.

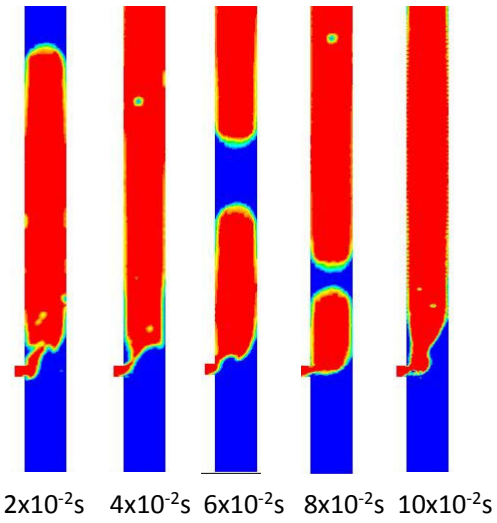

Figure 5.12: Snapshot of the simulation from 0.02 to 0.1 s for Case 1

Numerical results are very similar to experimental observations. Both extreme cases are consistent with experimental observations. Slug-annular flow has been obtained in Case 1 while annular flow is the flow pattern in Case 2 (Figure 5.12 and Figure 5.13,respectively). Since the flow patterns are near a transitional region,

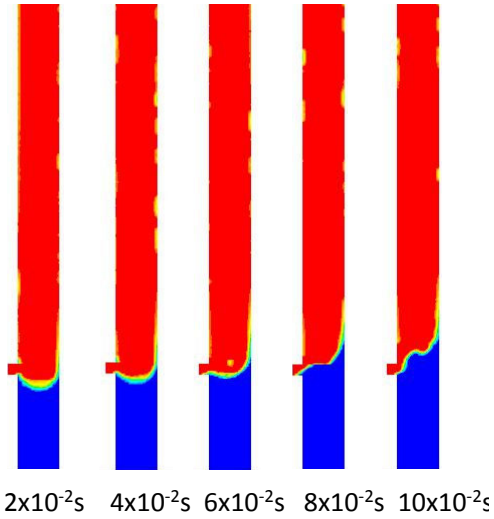

Figure 5.13: Snapshot of the simulation from 0.02 to 0.1 s for Case 2

gas and liquid mean velocities vary slightly over time. In the first section of the figures liquid displacement occurs. In the second part either annular flow or slug-annular flow is indicated. Some drops in gas velocity in Figure 5.10 correspond to bubbles break-up. Slight pulsation and an expansion of the gas bubble to a position below the gas inlet hole in experimental observation can be explained by a negative liquid mean velocity value in Figure 5.11.

Chapter 6

Direct Numerical Simulation of Interfacial Mass Transfer

6.1 Computational domain for interfacial mass transfer

The rise of an air bubble in a water-glycerol system is simulated in order to investigate the implementation of the mass transfer. The oxygen transfer in air is considered for interfacial mass transfer. The results for mass transfer are compared against the numerical approach published by Bothe et al. (2003) [46] and a Sherwood correlation by Chao [28, 76] and Calderbank and Moo-Young [29]. The approach of Bothe et al. (2003) is applied here for a 16 x 32 x 16 mm 3D computational domain, discretized with 50 x 100 x 50 uniform cubic mesh cells. In 3-D simulations it was adhered to use the computational domain of Bothe's benchmark for one-to-one comparison. However, the computational domain in 2-D is modified to avoid the influence of the wall on bubble rise velocity. Therefore channel diameter in 2-D simulations is increased to 32 mm. Influence of wall boundary condition (b.c.) on bubble velocity will be discussed in results section. A locally uniform square mesh refinement is provided in 2-D simulations in the center in order to investigate the influence of grid resolution on mass transfer. After the refinement process the mesh size is 1.6 10^{-4} mm in the first mesh refinement and 0.8 10^{-4} mm in the second mesh refinement and 0.4 10^{-4} mm in

the third mesh refinement for a size of 16 x 32 mm (Figure 6.1 and Figure 6.2). In order to minimize difference of the velocity gradient between unchanged mesh cells and mesh refinement cells the mesh size is step by step reduced.

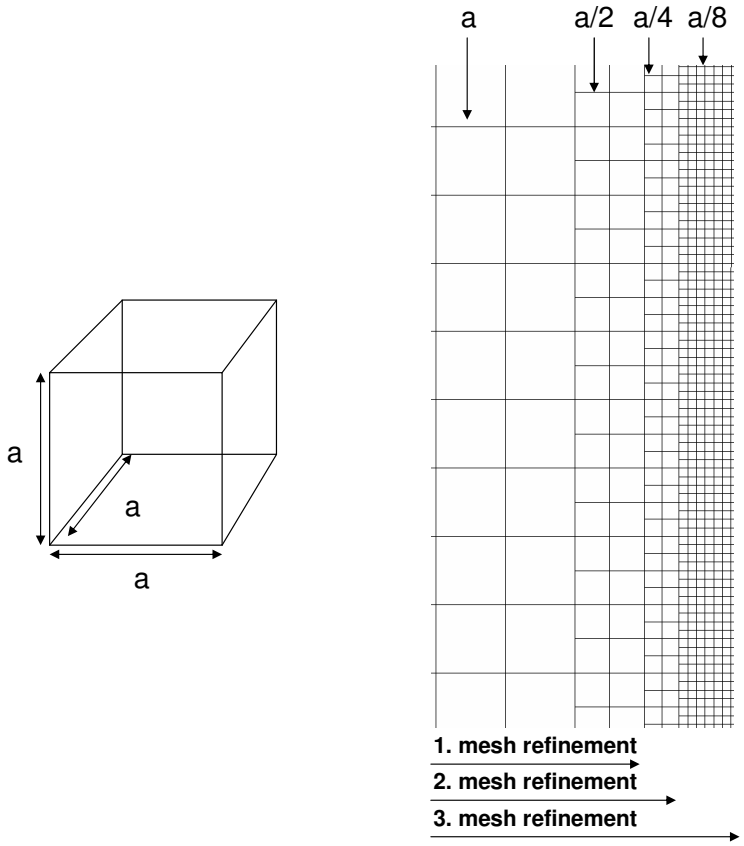

Figure 6.1: A typical uniform cubic mesh cell 3-D(left), uniform quadratic mesh cells for 2-D and mesh refinement strategy (right) for mass transfer simulations

The bubble is at fluid rest at x,y,z= (8, 8, 8) mm position in 3-D and h,r= (8, 0) mm position in 2-D cylindrical coordinates (Figure 6.2). The four sides and the bottom wall are defined with no-slip boundary conditions while a boundary condition of pressure outlet is implemented on the top side.

In the present research external mass transfer from air into a miscible water-glycerol mixture at 1 bar and room temperature is investigated. Physical properties at 1 bar and room temperature under simulation are listed in Table 6.1.

Water-glycerol mixture viscosity	$7.5x10^{-2}$ Pa.s
Water-glycerol mixture density	1205 kg/m^3
Air viscosity	$18.24x10^{-06}$ Pa.s
Air density	1.122 kg/m^3
Oxygen diffusivity in water-glycerol mixture	62.24 x 10^{-8} m^2/s
Surface tension coefficient	0.063 N/m
Saturation concentration	0.008 kg/m^3

Table 6.1: Physical properties of the fluids at 1 bar and room temperature applied in the mass transfer simulations

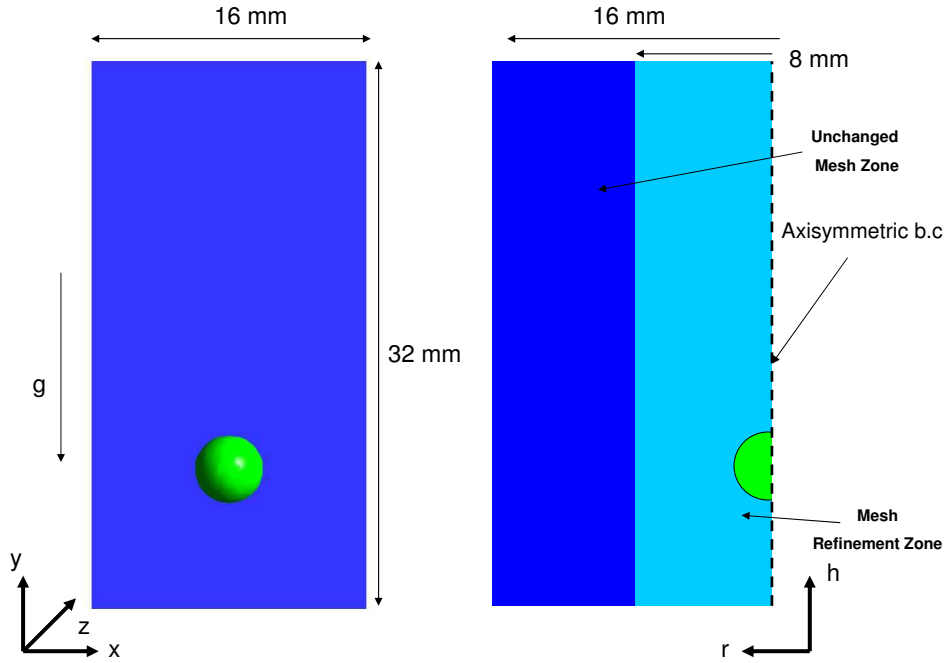

Figure 6.2: Cross section of computational domain at z=8 mm in 3-D(left), Computational domain of 2-D (right)

Initial bubble diameter should have been 4 mm according to Bothe's benchmark setup. In our calculations it was possible to initialize the bubble diameter as 3.84 mm using the mesh size 3.2 10^{-4} mm. In all simulations for the pressure-velocity coupling scheme the Pressure-Implicit with Splitting of Operators (PISO), which is based on the higher degree of the approximate rela-

tion between the corrections for pressure and velocity, is implemented. First order scheme for species and momentum equations is used in 3-D simulations. After a comparison of the mass transfer results delivered from first order and Quadratic Upstream Interpolation for Convective Kinematics (QUICK) scheme implemented into species and momentum equations, QUICK scheme is used in 2-D simulations while the results for mass transfer with first order scheme is over-predicting. This will be discussed in the results section. The convenient time step size for 3-D simulations is 10^{-4} s while for 2-D simulations it is 10^{-6} s. The convergence criteria for scaled residuals are set to 10^{-3} for continuity, momentum, and species equations. Reynolds number is calculated according to

$$Re_{bub} = \frac{\rho_l d_{bub} U_{bub}}{\mu_l} \tag{6.1}$$

where d_{bub} is diameter of the bubble and U_{bub} is bubble velocity calculated by

$$U_{bub} = \frac{\sum_{x=1}^{N_x} \sum_{y=1}^{N_y} \sum_{z=1}^{N_x} f^g_{x,y,z} v_{y:x,y,z}}{\sum_{x=1}^{N_x} \sum_{y=1}^{N_y} \sum_{z=1}^{N_x} f^g_{x,y,z}} \tag{6.2}$$

Here, v is the y-component of the velocity in all gas cells. The subscripts x, y and z denote the mesh cell index in x-,y-, and z-direction, respectively, and N_x , N_y and N_z denote the number of mesh cells in these directions within the computational domain.

The Schmidt number physically relates the relative thickness of the hydrodynamic layer and mass-transfer boundary layer.

$$Sc = \frac{\mu_l}{\rho_l D} \tag{6.3}$$

The Schmidt number for this case is 100, but Schmidt numbers of 10 and 1 are also considered with artificial increasing of diffusion coefficients. The results of mass transfer for the Schmidt numbers in the range of 1 to 100 will be discussed in the results and discussion section.

Using the governing equations for interfacial mass transfer in Chapter 4 the

VOF method with combination of mass transfer is solved for the free rising bubble. The flow is treated as incompressible since the pressure drop along the reactor is small (ca. 4 Pa) except for one case in order to investigate the influence of compressible gas on bubble volume. This will be discussed in result section.

The PLIC scheme defines the interface between fluids using a piecewise-linear approach at interface cells. In Ansys Fluent this scheme is the most accurate one to solve void fraction equation. It assumes that the interface between two fluids has a linear slope in cells, and uses this linear shape for calculation of the advection of fluid through the cell faces [70, 72]. This scheme has three steps to solve void fraction equation of dispersed phase [70, 72]. The first step is calculating the position of the linear interface based on information about the volume fraction and its derivatives in the cell. The second step is calculating the advection amount of fluid through each face using the computed linear interface representation and information about the normal and tangential velocity distribution on the face. The third step is calculating the volume fraction in each cell using the balance of fluxes calculated during the previous step.

6.1.1 Minimum length scales

For the direct numerical simulations the consistency of the minimum length scale is essential. The Kolmogorov length scale should be provided for velocity gradients. Thus, implementation of the Kolmogorov length scale avoids viscosity domination and provides the smallest scales of turbulence. In addition for the concentration field the Batchelor scale describes the smallest length scales of large fluctuations in concentration before molecular diffusion dominates. The Batchelor length scale provides a coincidence for diffusive transport of species equation and momentum equation [46, 77]. Therefore for precise direct numeric simulations the length scale of the unit cell and thus in the interface cell should be in the range of the Kolmogorov length and/or the Batchelor length scales should be considered for velocity and concentration gradients.

The correlation of Kolmogorov length scale is:

$$L_{Kol} = \left(\frac{\nu^3}{\epsilon}\right)^{0.25} \tag{6.4}$$

where ν is the kinematic viscosity. The energy dissipation ϵ can be calculated from

$$\epsilon = U_{bub}.g \tag{6.5}$$

The Kolmogorov length scale is 6.7 10^{-4} m calculated with determined U_{bub} of 0.12 m/s (see Figure 6.12) and the physical properties given in Table 6.1. The Batchelor length is the ratio of Kolmogorov length scale to root of Schmidt number.

$$L_{Bat} = \frac{L_{Kol}}{\sqrt{Sc}} \tag{6.6}$$

The Batchelor length ($0.67\ 10^{-4}$ m) is 10 times smaller than the Kolmogorov length scale for this case. It can be seen that in the case of mass transfer simulations Schmidt number play a significant role to determine the mesh size in the computational domain when Schmidt number is greater than unity.

6.2 Results and Discussion

6.2.1 Influence of compressible gas on bubble volume change in 3-D

The bubble volume changes physically due to mass transfer and also due to a pressure drop in the minichannel. In order to find out the importance of the pressure difference on bubble volume change in the minichannel, gas is treated as a compressible gas in a simulation. The static pressure between outlet and inlet

can be calculated using following equation:

$$P_{cal} = \rho_l g h = 9.81x1205x3.2x10^{-4} = -3.8\,Pa \tag{6.7}$$

where h is the length of the channel. The simulated pressure difference between outlet of the channel and bottom of the wall is only ca. -4 Pa. Figure 6.3 shows change of normalized diameter of the bubble over time for the calculation of compressible. The normalized diameter is calculated as:

$$d_{norm} = \frac{d_{bub}}{d_{bub_0}} \qquad d_{bub} = \sqrt{\frac{6V}{\pi}}^3 \tag{6.8}$$

The dotted line corresponds to the calculation of the normalized diameter of bubble change for compressible gas assumption in Figure 6.3. At the beginning of the simulation there is an artificial transient zone due to initiation of the calculation. After a while the bubble diameter stabilizes and then it increases due to pressure drop and static pressure difference while the bubble moves upward. Total change due to pressure difference in compressible gas calculation is very small ca. 0.025 % which may not be taken in account in mass transfer calculation. Therefore, all simulations for the investigation of volume change due to the mass transfer were performed as incompressible fluids in order to reduce the CPU time.

6.2.2 Comparison of the PLIC methods in 3-D simulations

Figure 6.4 shows the progression of the normalized diameter of the bubble (Equation 6.8) due to mass transfer calculated by PLIC-1 and PLIC-2 methods with a 50x100x50 cells and uniform mesh. The concentration profile at the middle line of the computational domain is shown in Figure 6.5.

In order to better understand the reason of similar results delivered by PLIC-1 and PLIC-2 the calculated discretization length s (ΔX/a) in the interface cells is plotted in Figure 6.6 and Figure 6.7. The x axis in Figure 6.7 corresponds to the cell index of Figure 6.6.

s in the Figure 6.7 denotes the ratio of ΔX and mesh size. PLIC-1 and PLIC-2 methods delivered interestingly almost the same results within a deviation of only

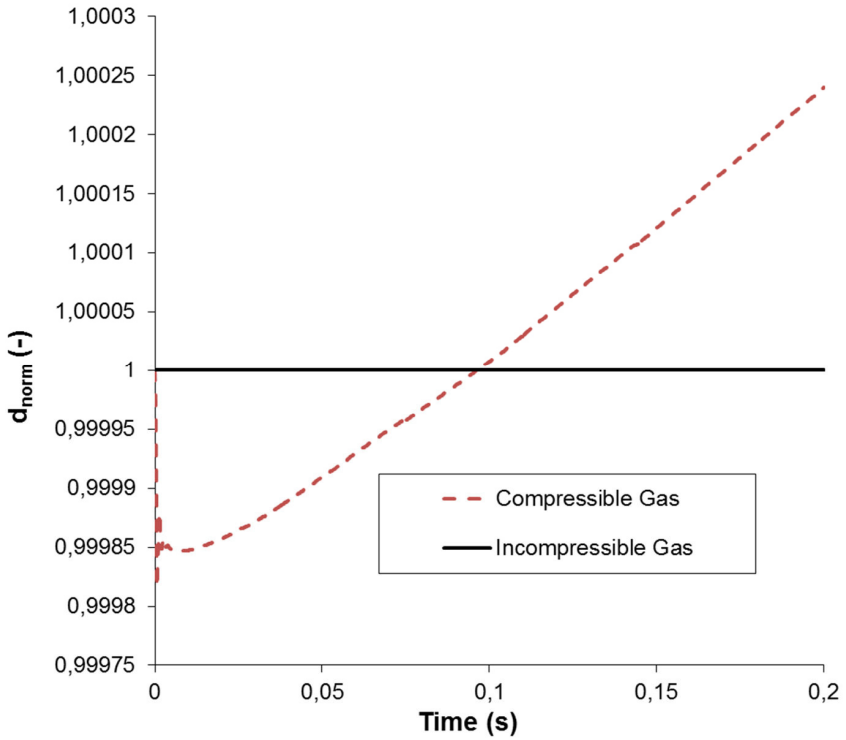

Figure 6.3: Change of normalized diameter for compressible gas during the free rising bubble using 50x100x50 mesh cells in 3-D

up to 1% for the average discretization length (mean value) in the interface cells (Figure 6.7). Calculation of the ΔX using the same void fractions in cubic cells give similar results. PLIC-1 has more accuracy but on the other hand calculation time of ΔX in PLIC-2 is fast since the iteration progress is not needed. On the other hand PLIC-2 results for calculated Sherwood number is not stable as much as PLIC-1 as it is shown in Figure 6.8.

Consistent results are obtained in comparison to results from literature [46, 78] as it is displayed in Table 6.2. Due to the small bubble size shrinkage (Figure 6.4) the bubble aspect ratios and bubble velocities of the different numerical analyses which do not consider volume shrinkage are very near to our results. This is not very surprising. However, the consistency in the CWL is an indication of correct implementation of the calculation of ΔX from the interface normal vector and the void fraction. The hydrodynamic results as well as the aspect ratio of the bubble show good agreement also with the experimental observation from Raymond and

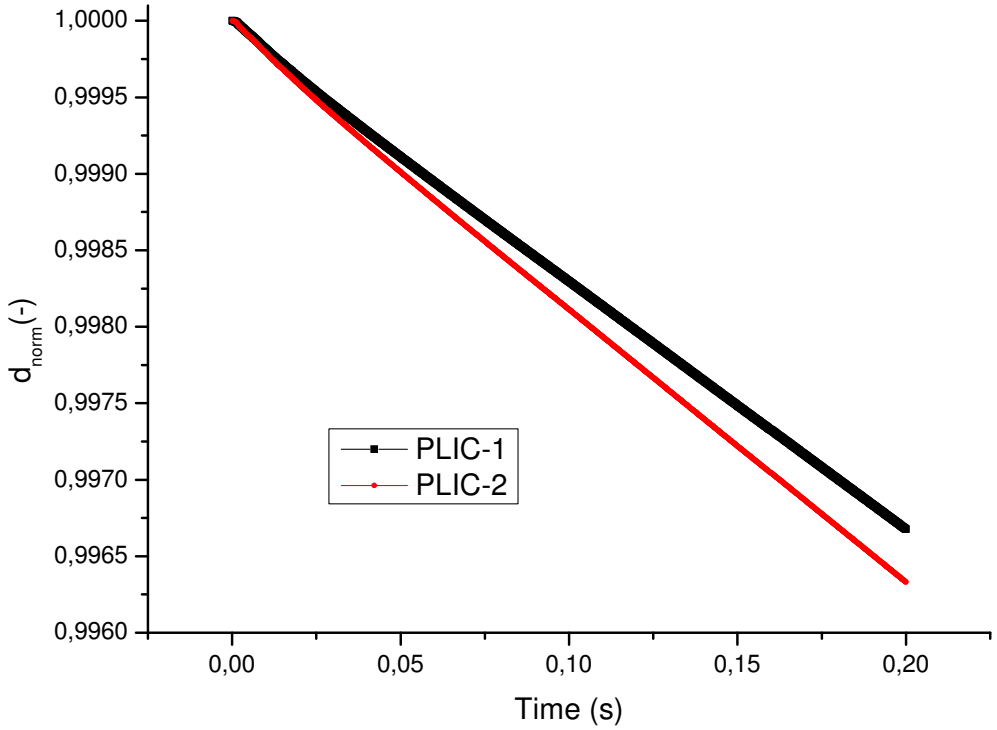

Figure 6.4: Normalized diameter of the free rising bubble with the two different ΔX distance calculation methods. Time indicates the duration of the free rising bubble. Mesh resolution: 50x100x50 cells

Rosant (2000) published in [78].

There is no available experimental data to compare the concentration distributions. One of the difficulties lies in measuring concentration distribution and values in spatial and time resolution. Investigations of bubble dissolution in continuous phases are under development [79]. However, in the numerical results some assumptions are still made which may produce differences to the experiment; for example piecewise incompressible fluids, contaminants influence and Marangoni effect are not considered. Therefore the results are compared with theoretical correlations to prove the models under parameter variation.

A well known Sherwood correlation from Calderbank and Moo-Young ([29]) for free rising bubbles (d_b>2.5 mm) is;

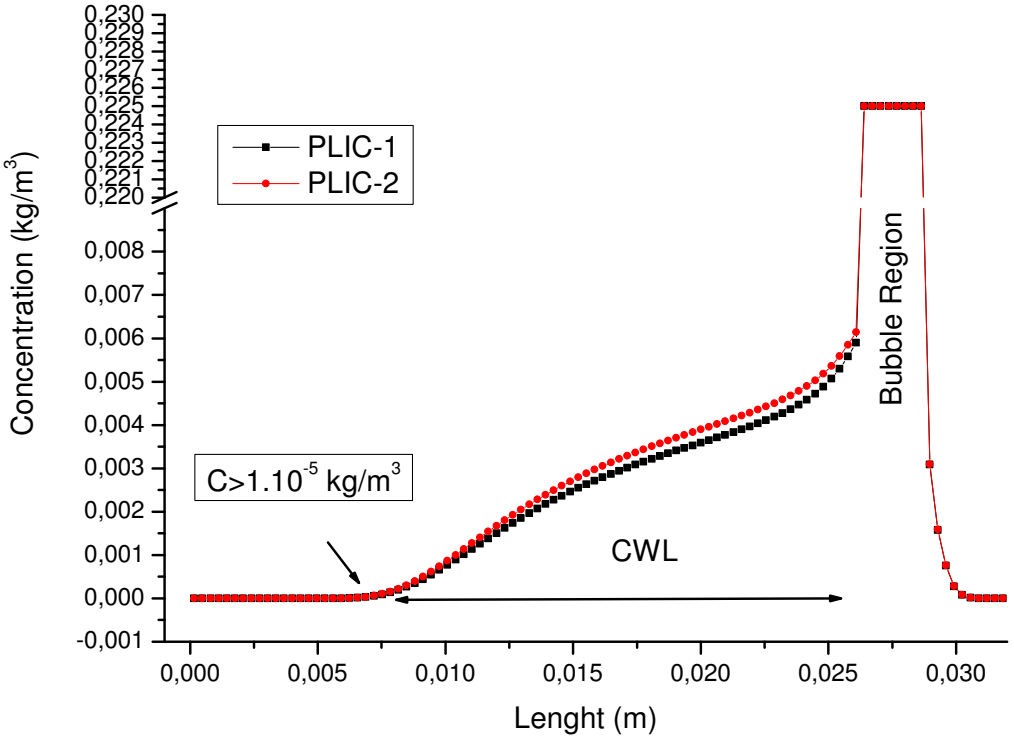

Figure 6.5: Concentration profile in flow direction (y axis) in the middle of the channel using PLIC-1 and PLIC-2 method with First Order scheme. Mesh resolution: 50x100x50 cells

$$Sh = 0.42\ Gr^{1/3}\ Sc^{1/2} \tag{6.9}$$

where Grashof (Gr) number is;

$$Gr = \frac{d_{bub}^3 . \Delta\rho . \rho_l . g}{\mu_l^2} \tag{6.10}$$

Sherwood number correlation from Chao (1962) [28, 76] is a function of Re and Sc for bubble spheres with mobile interfaces as follows:

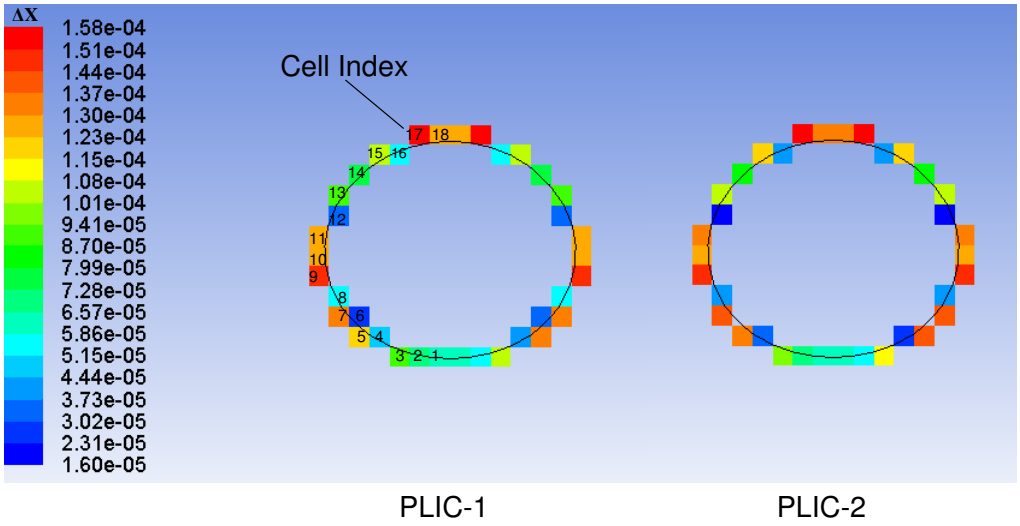

Figure 6.6: Discretization lengths with PLIC-1 calculation (left) and with PLIC-2 calculation (right). Mesh resolution: 50x100x50 cells

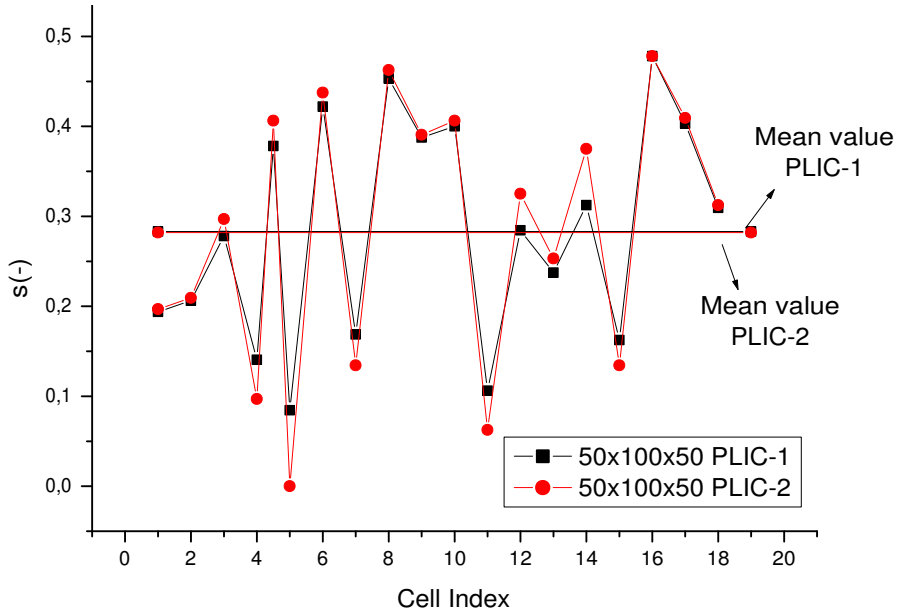

Figure 6.7: Comparison of discretization lengths with PLIC-1 and PLIC-2 method. X axis corresponds the circular of cell index of Figure 6.6

$$Sh = 1.13 \left[1 - \left(\frac{2 + 3\mu_g/\mu}{1 + (\rho_g \mu g/\rho\mu)^{0.5}}\right) \frac{1.45}{Re^{0.5}}\right] Pe^{1/2} \tag{6.11}$$

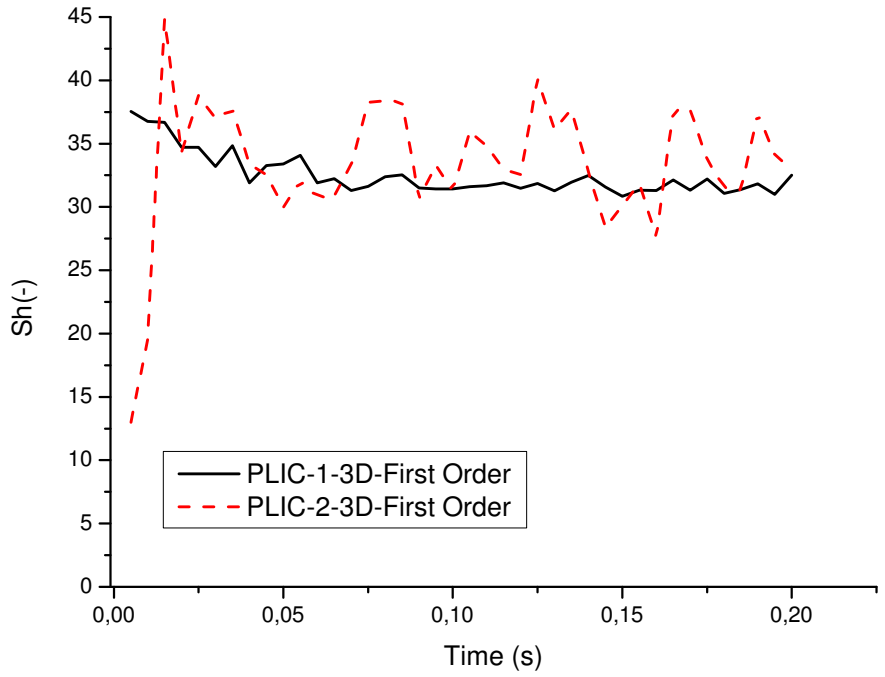

Figure 6.8: Influence of PLIC-1 and PLIC-2 method on Sherwood number

In order to compare the numerical results with the empirical correlations the diffusion coefficient was artificially altered by a factor of 10 and 100 (corresponding to Sc=10 and Sc=1 respectively). Figure 6.9 shows that numerical results with first order scheme are slightly overestimating the mass transfer.

Figure 6.10 shows the concentration gradients in the liquid at Re =7.06 for different Sc numbers. For Sc=1 a very long concentration wake length and width can be observed. The concentration gradient at Sc=10 is less compared to concentration gradient at Sc=1. Concentration length and width is also smaller. In the real physical case (at Sc=100) the concentration length and width are qualitatively similar to experimental observations by Francois (2010) and Bork (2001) [79, 80].

	Bothe (2003)	Onea (2006)	Raymond (2000)	Results with PLIC
CWL (m)	0.014	0.018	-	0.018
AR	0.86	0.87	0.86	0.87
U_{bub}(m/s)	0.12	0.11	0.13	0.11

Table 6.2: Comparison of results with data in literature at 0.2 s absorption time. (CWL=Concentration wake length of traceable gaseous species in the liquid, AR= Aspect Ratio of bubble)

6.2.3 Comparison of First order and QUICK scheme results for mass transfer in 3D simulations

The comparison of QUICK and first order schemes for mass and species equations is shown in Figure 6.11 by plotting the numerical Sherwood number against bubble rising time. In first-order schemes quantities at cell faces are determined by assuming that the cell-center values of any field variable represent a cell average value and the face quantities are identical to the cell quantities. For quadrilateral and hexahedral meshes ANSYS FLUENT also provides the QUICK scheme for computing a higher-order value of the variable at a face. QUICK-type schemes are based on a weighted average of second-order-upwind and central interpolations of the variable and give more accurate solutions on structured meshes. From Figure 6.11 it can be seen that the numerical Sherwood number is high at the beginning of the bubble rise since there is almost no gas concentration in the liquid phase. In the comparison of the schemes the numerical Sherwood number with QUICK scheme is between the theory of Chao (Eq.6.11) and the theory of Calderbank&Moo-Young (Eq.6.9), whereas the first order scheme is overestimating mass transfer.

6.2.4 Influence of wall distance on bubble velocity in 2-D

For the geometry of the computational domain it was adhered to the system of Bothe et al. (2003) [46] for one-to-one comparison in 3-D simulations. However, investigations for the influence of wall b.c. on bubble rise velocity have been done in 2-D using an interval mesh size 3.2 10^{-4}m. The diameter of the

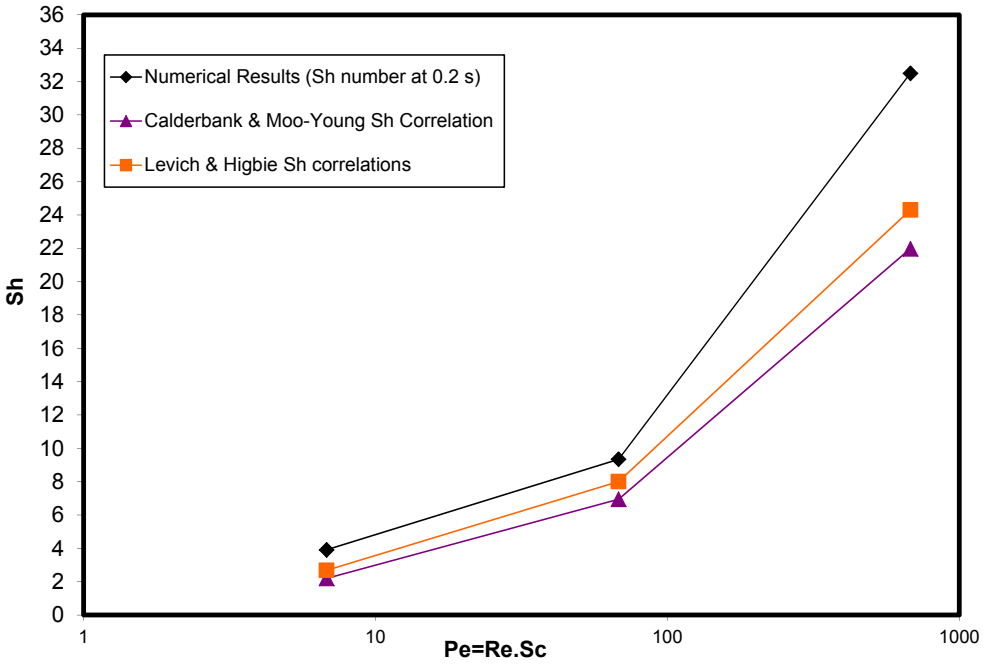

Figure 6.9: Comparison of numerical results with empirical Sherwood correlations. In numerical results PLIC-1, First order scheme for momentum and species equation and 50x100x50 mesh resolution are used.

channel was varied between approximately twofold and eightfold of the bubble diameter. The line W=16 mm corresponds the system of Bothe et al. [46] in Figure 6.12. Increasing of the channel diameter increases the bubble rise velocity. The influence of channel diameter on bubble velocity minimizes after sixfold of bubble diameter and it almost disappears at channel diameter of 32 mm. Bubble velocity at steady-state zone approaches to 0.13 m/s, which is in accordance with experimental observations from Raymond (2000) (Table 6.2). Influence of the pressure outlet (P.0.) on bubble velocity can be observed after 0,17 s when the channel diameter is greater than 16 mm. Bubble velocity increases till 0.012 s at the channel diameter of 8 mm. It reaches a steady state earlier. If the channel diameter is greater than 8 mm, the required time of transient zone increases. Since the channel diameter of 32 mm has almost no influence on bubble rise velocity, it was selected for investigation of interfacial mass transfer calculations. Further results will be shown at 0.15 s in order to avoid influence of pressure outlet.

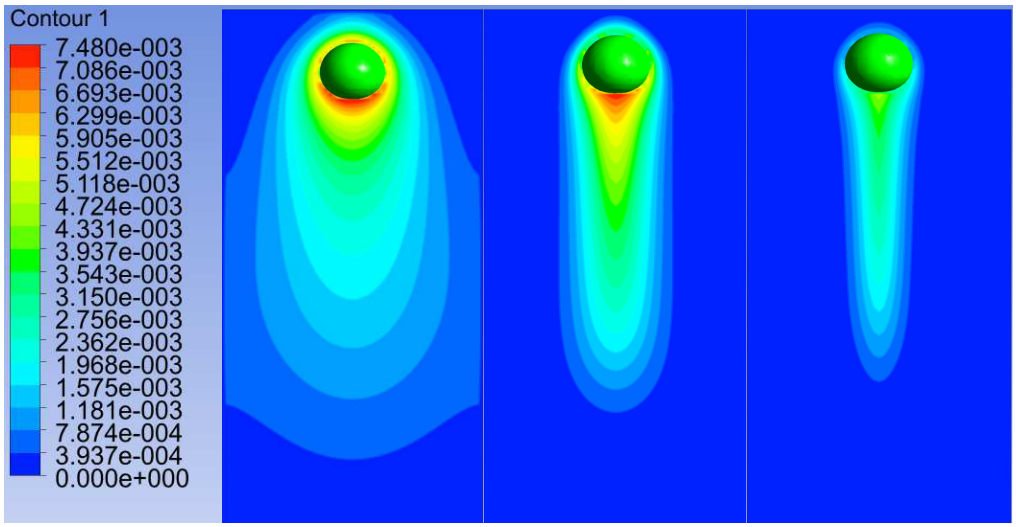

Figure 6.10: Concentration distribution at Sc=1 (left), Sc=10 (middle), Sc=100 (right) at 0.2 s. (The coloured scale is the concentration of oxygen in kg/m^3). PLIC-1, First order scheme for momentum and species equation and 50x100x50 mesh resolution are used.

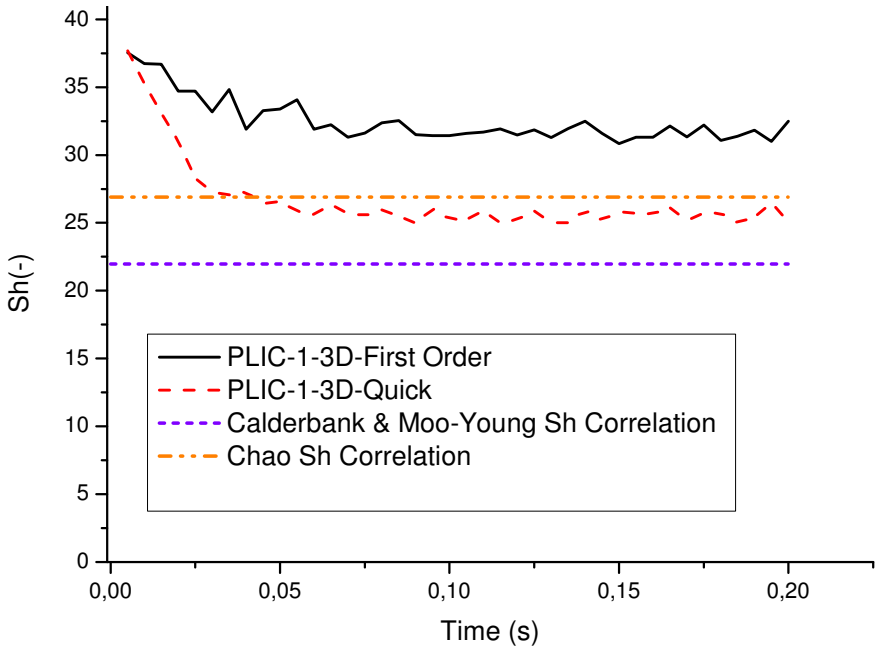

Figure 6.11: Influence of spatial discretization on mass transfer in 3-D. Mesh resolution: 50x100x50. Time indicates the duration of the free rising bubble.

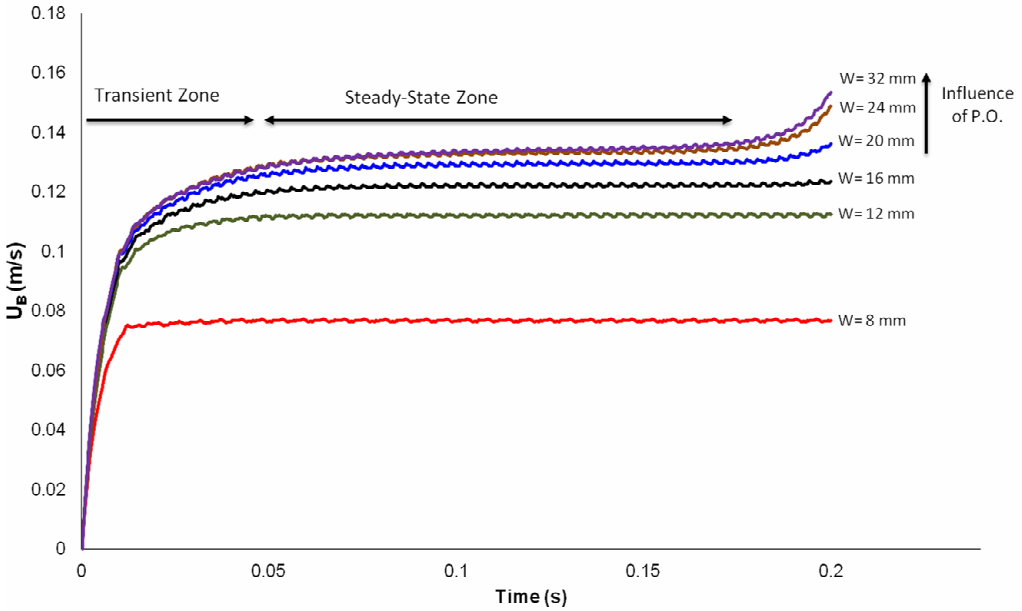

Figure 6.12: Temporal evolution of bubble velocity for different channel diameters with interval mesh size 3.2 10^{-4}m in 2-D, (W=channel diameter). Time indicates the duration of the free rising bubble. P.O = pressure outlet

6.2.5 Influence of mesh size on mass transfer in 2-D Simulations

In order to continue the investigations on the influence of mesh size on mass transfer it was switched to axis-symmetric 2-D simulations and PLIC-1 method was implemented. A time step size (10^{-6} s) on mass transfer for the smallest mesh size (0.4 10^{-4} m) was implemented in all 2-D simulations. Physical properties from Table 6.1 were also used during the 2-D simulations. For momentum and species equations Quadratic Upstream Interpolation for Convective Kinetics (QUICK) scheme was implemented.

Influence of mesh size on Sherwood number is shown in Table 6.3. Numerical average Sherwood number between 0.05 and 0.15 s (in steady state zone) in Table 6.3 is calculated as follows:

$$Sh_{avg} = \frac{\sum_{n=1}^{n} \frac{k_{avg}.d_{bub}}{D}}{n} \tag{6.12}$$

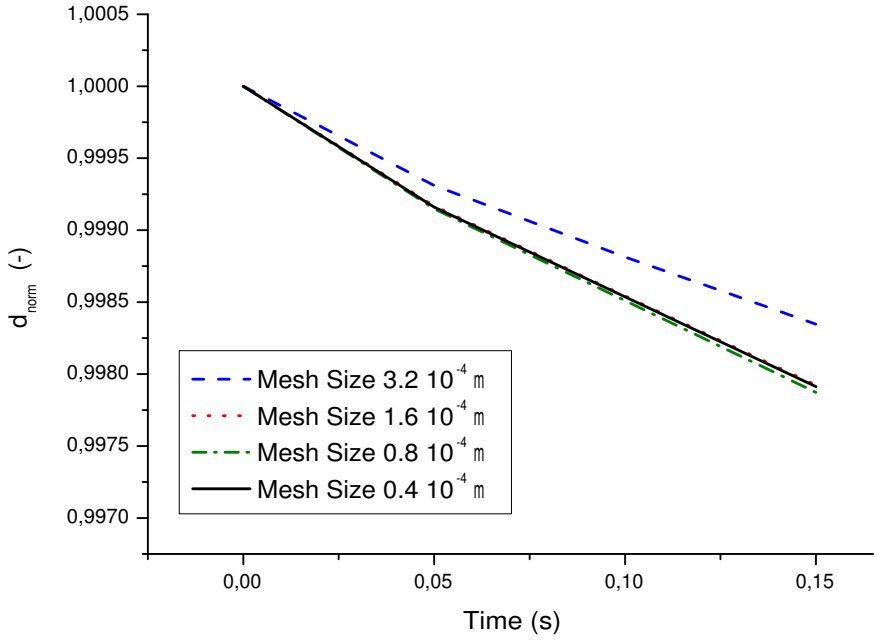

Figure 6.13: Influence of mesh size on normalized diameter of the free rising bubble versus time with PLIC-1 concept in 2-D simulations.

where n is the number of selected time points. k_{avg} is the average mass transfer coefficient calculated by

$$k_{avg} = \frac{\dot{m}_{avg}}{A(C_{sat} - C_{avg})} \tag{6.13}$$

According to the Batchelor length scale the required minimum mesh size is 0.67 10^{-4} m for having the realistic concentration gradients in this case. Independent mass transfer on mesh size was found in the range of Batchelor length scale. The influence of the mesh size on decrease of bubble diameters (calculated with an assumption of spherical bubble) is shown in Figure 6.13. Influence of mesh size on bubble diameter disappears after the second mesh refinement. Figure 6.14 shows the influence of the grid resolution on the numerical Sherwood number against time. Oscillations are observed at lower grid resolution perhaps due to the parasitic currents and/or huge concentration difference at interface cells. They disappear only with the finest mesh size. After the second mesh refinement

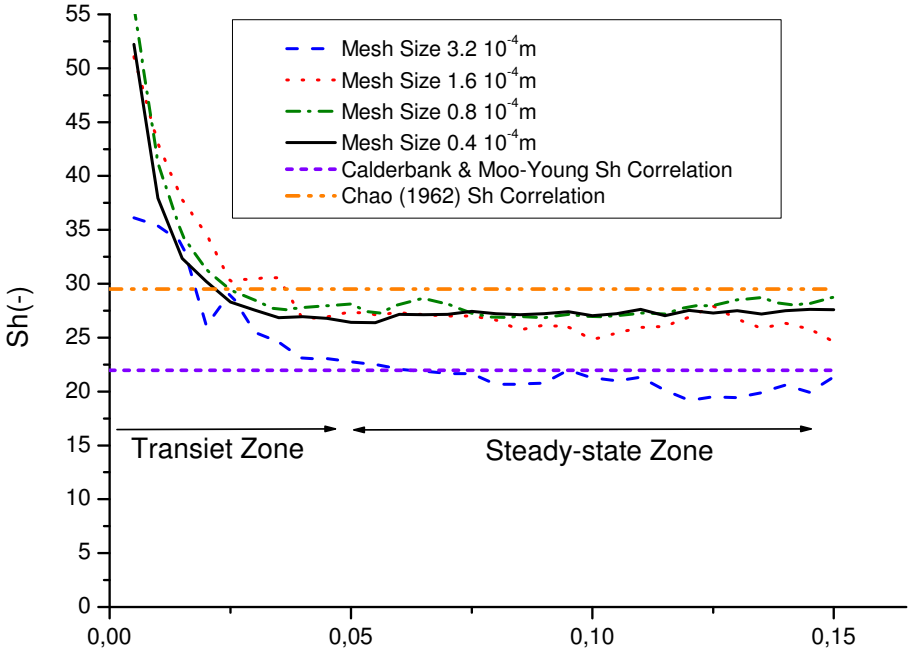

Figure 6.14: Influence of grid resolution on the numerical Sherwood number with PLIC concept. Time indicates the duration of the free rising bubble.

Mesh size (m)	$3.2\ 10^{-4}$	$1.6\ 10^{-4}$	$0.8\ 10^{-4}$	$0.4\ 10^{-4}$
$\dot{m}_{avg}$ (kg/s)	$1.12\ 10^{-9}$	$1.4\ 10^{-9}$	$1.44\ 10^{-9}$	$1.4\ 10^{-9}$
k_{avg} (m/s)	$3.5\ 10^{-3}$	$4.3\ 10^{-3}$	$4.4\ 10^{-3}$	$4.3\ 10^{-3}$
Sh_{avg} (-)	20.1	26.3	27.7	27.2

Table 6.3: Influence of grid resolution on mass transfer

the Sherwood number approaches 27. Refinement of the mesh size at interface cells approaches a stable mass flow rate. The corresponding values are detailed in Table 6.3.

Conclusions

In the present work the static contact angle of hydrogen-nitrobenzene on stainless steel and on a carbon surface has been measured using a static droplet method. Observation of two phase flow in microreactors has been done. Influence of surface tension, geometrical properties, static contact angle on immiscible two phase flows have been explored in microreactors using the VOF method. One of the most important goals of this research was to model mass transfer mechanism from gas phase to liquid phase through interface in the VOF method. Influence of mesh size, schemes and different Sc numbers on mass transfer mechanism were investigated for a free rising bubble in a minichannel in order to compare the numerical results with the simplified derivations of the differential equations and correlations from theoretical results.

One of the difficulties is still to handle viscosity singularity in VOF methods if a contact line occurs in microreactors. In order to correctly model the physical motion of the contact line between three phases (here gas-liquid-solid) depending on the wall boundary conditions, additional user effort will be needed to implement the required boundary condition into codes; e.g. for slip length and dynamic contact angle there is no universal model available. Standard CFD codes work with a non-slip boundary condition on walls and thus an infinite divergence depending on the viscosity may occur leading to a viscosity singularity near the walls. It should be noted here that non-slip boundary condition does not mean that the contact line will not move, but the presented results may thus have up to 5% error due to an applied non-slip boundary condition compared to calculations with slip boundary condition. However, for the latter boundary condition artificial slip lengths must be chosen, which are generally one magnitude smaller than the applied mesh size [81, 82]. Another possible approach to avoid

viscosity singularity is integration of an analytical calculation of the velocity field in a truncated domain which may reduce the influence of the mesh dependence in such an approach [83].

Direct numerical mass transfer investigation for a free rising bubble using two numerical concepts (PLIC-1 and PLIC-2) to discretize concentration gradients at interface cells has been done. Results obtained from these two numerical concepts are almost identical. PLIC-1 approach has more accuracy but is more time consuming than the PLIC-2 approach. The mass transfer source term was linked to void fraction and mass conservation equation to implement the bubble shrinking due to mass transfer. Results of the numerical Sherwood number are in accordance with theoretical results as long as sufficient grid resolution and high order schemes for spatial discretization with low time step sizes are implemented. Comparison of numerical results with experimental research shows qualitatively good agreement. However, the challenge of direct measurement of local concentration field in two phase flows makes it difficult to evaluate quantitatively the numerical results in comparison to the experimental results.

For the discretization with the two numerical concepts (PLIC-1, PLIC-2), a code was introduced into Fluent to determine the characteristic length between gas- liquid interface and center of liquid in the interface cells. The code included the geometrical calculations since Fluent only provides the normal vector and the gas-liquid ratio for the interface cells. However, the diffusion length ΔX is required to introduce diffusion from the interface as major transport mechanism in the interface cells. In the numerical concept of PLIC-1 ΔX is almost an exact solution while in the PLIC-2 concept the characteristic length is approximated. On the other hand PLIC-1 is more time consuming than PLIC-2 approach. Nevertheless, delivered results from PLIC-1 and PLIC-2 concept are interestingly almost identical within a deviation of only up to 1% for the average characteristic length in the interface cells. The species conservation equation and mass conservation equation was evaluated with analytical results. It was shown that in order to obtain reasonable results, the cell size should be in the order of the Batchelor length scale. This was proven by the influence of mesh size on mass transfer. Mass transfer approaches a steady state value at Batchelor length scale of the cell size. In the comparison of the schemes the numerical Sherwood

number with QUICK scheme is between the theory of Chao (Eq.6.11) and the theory of Calderbank&Moo-Young (Eq.6.9), whereas the first order scheme is over-predicting mass transfer.

As a consequence VOF method gives an opportunity to define mass transfer mechanism due to a diffusion mechanism at interface cells. However, due to high CPU times it is only possible to model a piece of the reactor and only a time less than one second of real time. Another drawback of VOF method is smearing at interface cells. This smearing does not allow the definition of interface area accurately. A geometrical interfacial area might be implemented to reduce the mesh influence on mass transfer.

Appendix A

Physical Data

A.1 Determination of densities

$$\rho(kg/m^3) = \frac{A}{B^{1+\left(1-\frac{T/K}{C}\right)^D}} \tag{A.1}$$

	Nitrobenzene	Aniline	Water
A	1.9545	0.3475	1.5054
B	0.0366	0.017	0.0364
C	773.898	730.870	617.774
D	0.1236	0.0814	0.0587

Table A.1: Density Constants for Nitrobenzene, Aniline, Water

Hydrogen density can be determined using ideal gas equation;

$$pV = nRT \tag{A.2}$$

with

$$n = \frac{m}{M} \quad and \quad \rho = \frac{m}{V} \tag{A.3}$$

$$\rho = \frac{MP}{RT} \tag{A.4}$$

A.2 Determination of viscosities

In VDI Waermeatlas viscosity of gas and liquid can be determined with a general formula for gases and liquids as following;

$$ln\frac{\mu}{Pa.s} = A + \frac{B}{T/K} + C\frac{T}{K} + D\left(\frac{T}{K}\right)^2 + E\left(\frac{T}{K}\right)^3 \tag{A.5}$$

$$\frac{\mu}{Pa.s} = A + B\frac{T}{K} + B\left(\frac{T}{K}\right)^2 + D\left(\frac{T}{K}\right)^3 + E\left(\frac{T}{K}\right)^4 \tag{A.6}$$

	Nitrobenzene	Aniline	Water
A	-12.928	-44.572	-22.968
B	1807.75	7434.03	3275.89
C	0.001140	0.02835	0.017637
D (*10^3)	0.0028	0.1145	0.00693
E (*10^6)	-	-0.174	-0.012933

Table A.2: Viscosity Constants for Nitrobenzene, Aniline, Water [7]

	Hydrogen
A ($*10^5$)	0.18024
B ($*10^7$)	0.27174
C ($*10^{10}$)	-0.13395
D ($*10^{12}$)	0.00585
E ($*10^{15}$)	-0.00104

Table A.3: Viscosity Constants for Hydrogen [7]

A.3 Determination of surface tension

$$\frac{\sigma}{N/m} = A\left(1 - \frac{T}{T_c}\right)^B \tag{A.7}$$

	A	B	T_c(K)
Nitrobenzene	0.07946	1.13667	719

Table A.4: Surface Tension Constants for Nitrobenzene [7]

A.4 Determination of hydrogen saturation in nitrobenzene

Equation A.8 is only an approximation, and should be used only when no experimentally derived formula is available for a given gas. p is given atmospheres and c is given in $mol.(m^3)^{-1}$. However comparison of the following equations with experimental research by Radhakrishnan et al. (1983) [84] between 298- 343 K for hydrogen solution in nitrobenzene shows consistent results.

$$p = H_{pc}\, c \tag{A.8}$$

Radhakrishnan et.al (1983) [84] published the hydrogen solubility in nitrobenzene at 101 kPa and 298 K;

$$C_{H_2,NB} = 1.574 \frac{mol}{m^3}$$

Then Henry constant at 1 atm and 298 K for hydrogen in nitrobenzene is ;

$$H_{pc,H_2,NB} = 0.654 \frac{m^3}{atm/mol}$$

Temperature dependence of the Henry constant can be derived by integrating the van 't Hoff equation [85]

$$H_{pc}(T) = H_{pc}(T_{std}).e^{C\left(\frac{1}{T} - \frac{1}{T_{std}}\right)} \tag{A.9}$$

- H_{pc} for a given temperature is the Henry's Law constant,
- T is the thermodynamic temperature,
- T_{std} refers to the standard temperature (298 K),
- C is a constant and 500 K for the hydrogen [85].

H_{pc} (383.15 K) is 0.45 m^3.atm/mol. The saturation concentration at 1 atm and 383.15 K is :

$$C_{H_2,NB}\ (383.15K) = 2.286\ \frac{mol}{m^3} = 4.57 \frac{g}{m^3}$$

A.5 Oxygen saturation in water

Henry number is

$$H = \frac{C_{sat}}{C_{O_2,Air}} \tag{A.10}$$

$$C_{sat} = C_{O_2,Air}.H = 0.2688.0.03 \frac{kg}{m^3} = 0.008 \frac{kg}{m^3}\ [78]$$

A.6 Determination of hydrogen diffusion coefficient

Wilke and Chang [86, 87] describe the binary diffusion coefficient of a solute A in a solvent B in a dilute solution as

$$D_{A,B} = \frac{7.4\ 10^{-8}\,(\phi M_B)^{0.5}\,T}{\mu_B(cP)V_A^{0.6}} \tag{A.11}$$

In Equation A.11 A denotes hydrogen while B corresponds nitrobenzene. $D_{A,B}$ is given cm^2/s while M_B is given in (kg/kmol) and T is given (K).

	ϕ	M_B(kg/kmol)	V_A (-)
Values	1	123.06	14.3

Table A.5: Applied constants in diffusion coefficient correlation

A.7 Nitrobenzene and hydrogen mass flux

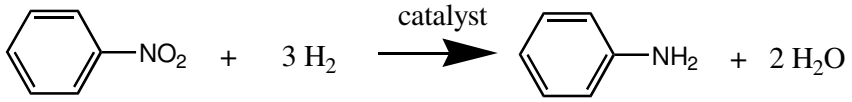

Figure A.1: Hydrogenation of nitrobenzene to aniline

This lab micro reactor is supposed to have 40 channels. Overall nitrobenzene flow rate in this inlet is supposed to be 1 ml/ min. Density of nitrobenzene is 1101.4 $\frac{kg}{m^3}$ at 10 bar and 120^{0}C. Viscosity of nitrobenzene is 61.3 10^{-5} $\frac{kg}{s.m}$.

$$\dot{V}_{NB,single\ channnel} = \frac{1}{40}\frac{ml}{min}$$

This is equal to 4.16 10^{-4} ml/s. The corresponding mass flow rate is:

$$\dot{m}_{NB,single\ channnel} = 1.1014\frac{g}{cm^3}\ 4.16\ .10^{-4}\frac{ml}{s} = 4.5810^{-7}\frac{kg}{s}$$

The inlet area of one channel is A=0.4mm*1mm=4 10^{-7} m^2. Thus mass flux is 1.145 $\frac{kg}{m^2 s}$.

The average nitrobenzene velocity at inlet is:

$$v = \frac{\dot{m_{NB}}}{\rho_{NB}.A} = \frac{4.5810^{-7}}{1101.4\ 4\ 10^{-7}}\frac{m}{s} = 1\ 10^{-3}\frac{m}{s} \tag{A.12}$$

The mol flow is:

$$\dot{n} = \frac{\dot{m_{NB}}\rho_{NB}}{M_{NB}} = \frac{1\ 1.101}{123}\frac{mol}{min} = 0.00895\frac{mol}{min} \tag{A.13}$$

Due to the reaction stoichiometry the hydrogen mole flow should be 0.0089.3= 0.0268 mol/min. The volume flow under standard conditions is:

$$\dot{V_{H_2}} = 0.0268\frac{mol}{min}.22400\frac{ml}{mol} = 601.44\frac{ml}{min}$$

Since the operating pressure is 10 bar and the operating temperature is 120 ^{0}C, the flow rate under working conditions is:

$$\frac{P_1\dot{V_1}}{T_1} = \frac{P_2\dot{V_2}}{T_2} \tag{A.14}$$

$$\dot{V_2} = \frac{1 * 601.44 * 393}{10 * 273} = 86.6\frac{ml}{min} \tag{A.15}$$

As this flow is distributed over 40 hydrogen inlet holes, the flow rate is 2.165

ml/min for each hydrogen inlet. The mass flow for each hole is 9.667 10^{-5} mol/min * 2 g/mol =3.22 10^{-9} kg/s. With a diameter of 40 μm the corresponding mass flux is 2.56 $\frac{kg}{s.m^2}$. The velocity is:

$$v_{H_2} = \frac{\dot{m_{H_2}}}{\rho_{H_2}.A} = \frac{3.22.10^{-9}}{0.618\pi 0.02^2 10^{-6}} \frac{m}{s} = 4.15 \frac{m}{s} \tag{A.16}$$

Appendix B

Validation of the code

B.1 Validation of numerical results with analytical results

In order to verify the species conservation and implementation of mass transfer rate in the code, five test cases have been considered. Analytical comparison has been employed in first four tests while in the last test a code to code comparison is provided. In the first test diffusion term in Equation B.1 (the first term on the left hand side) has been tested with analytical results provided by Crank [88]. Secondly, comparison of numerical results and analytical results for convective term of species conservation equation in Equation B.1 (the second term on the left hand side) as well as homogeneous reaction term have been done. Void fraction, e.g Equation 4.19, has been also compared with analytic results.

As phase change has also considered, void fraction equation Equations 4.20 on page 31 should be modified by source terms as it is also written on page 33.

The mass species conservation equation for multiphase flow in general form can be represented in the following equation for phase q:

$$\frac{\partial}{\partial t}(\rho^q f^q M_i^q) + \nabla \cdot \rho^q f^q \vec{v^q} M_i^q = -\nabla \cdot f^q \vec{J_i^q} + f^q R_{hmg}^{q_i} + f^q S_i^q \tag{B.1}$$

where $R_{hmg}^{q_i}$ is the net rate of production of homogeneous species i by chemical reaction for phase q. In addition, f^q is the volume fraction for phase q and S_i^q is the rate of creation from user-defined sources.

B.2 Test of diffusive term

Diffusive term in a 1-D problem has been tested with analytical solution which is provided by Crank [88]. Two media separated by an interface has been modelled for the test problem as it is shown in Figure B.1. 100x 100 cell grid resolution is implemented in the numerical studies. Mass transfer occurs only in one direction from Phase 1 to Phase 2. The concentration of Phase 1 is $C_0 = 1$ (dimensionless) and conserves this value during the mass transfer while the initial concentration in Phase 2 is zero at the beginning and increases by time.

The analytical concentration distribution has been introduced by Crank [88];

$$C = C_0.erfc\left(\frac{x}{2\sqrt{Dt}}\right) \tag{B.2}$$

with satisfying the boundary condition:

$$C = C_0, x = 0, t > 0 \tag{B.3}$$

and initial condition:

$$C = 0, x > 0, t = 0 \tag{B.4}$$

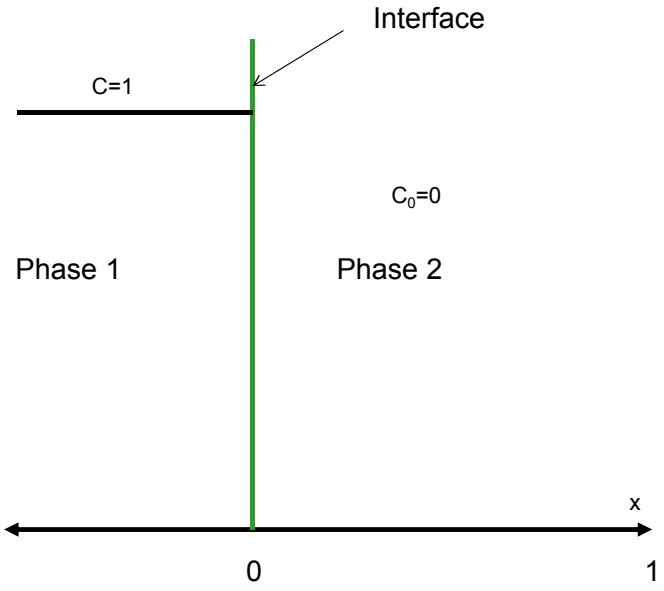

Figure B.1: Geometry of 1-D study

where x distance from the interface to Phase 2, t time, D is the diffusion coefficient ,which is $10^{-}9$ m^2/s used in analytical and numerical problems.

The Equation B.1 for diffusive problem becomes:

$$\frac{\partial}{\partial t}(\rho^q f^q M_i^q) = -\nabla \cdot f^q \vec{J_i^q} \tag{B.5}$$

where $\vec{J_i^q}$ is :

$$\vec{J_i^q} = -\rho^q D_{i,m} \nabla M_i^q \tag{B.6}$$

The concentration curves in Figure B.1 obtained analytically and numerically are shown in Figure B.2. Lines with squares in Figure B.2 correspond to numerical solutions while the lines with dots display the analytical solutions. A finer case, i.e. 200x200, has been also investigated as it is discussed in Appendix B.2.

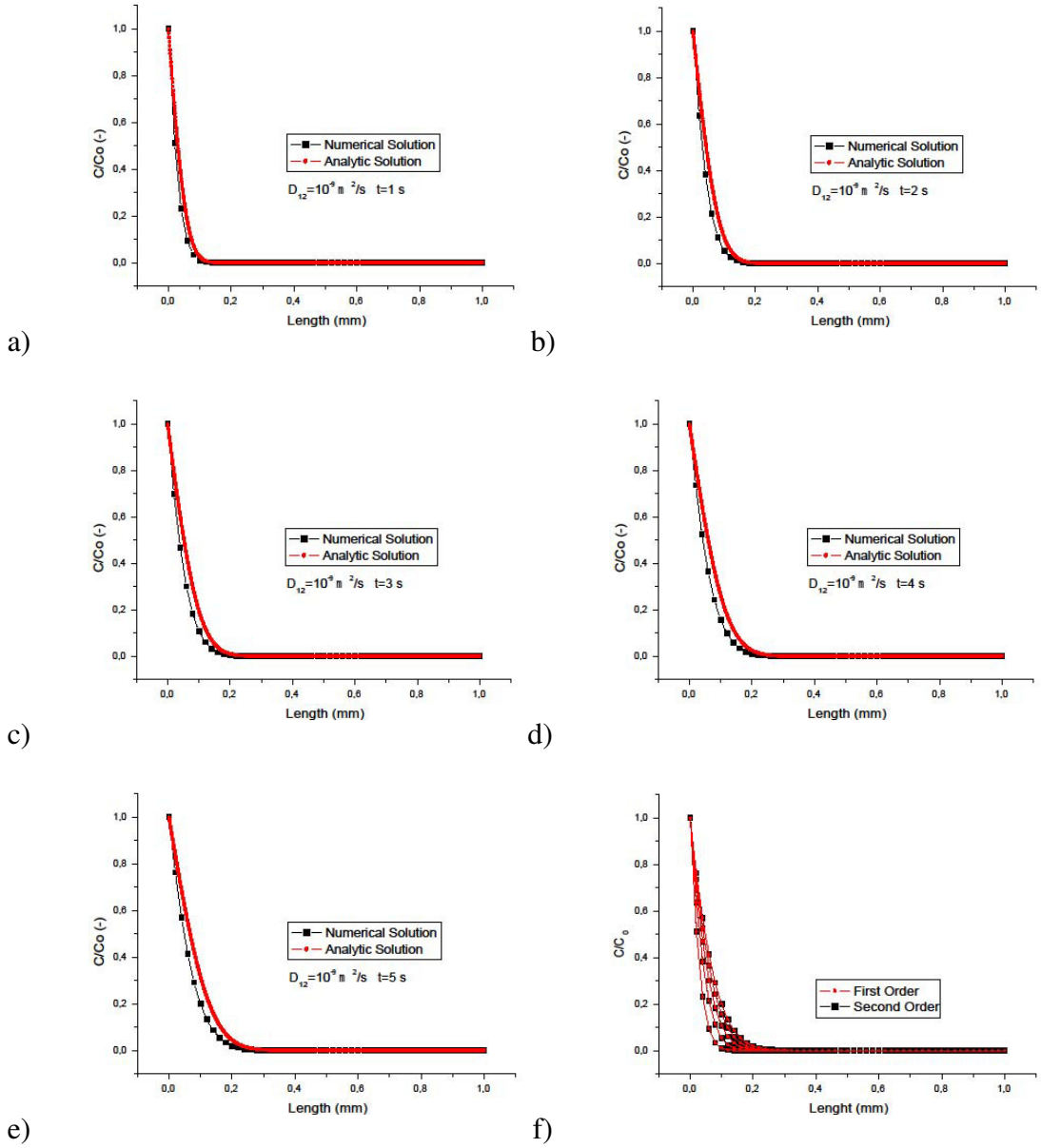

Figure B.2: 1-D study on the influence of the diffusive term comparison of numerical and analytic results with 1st order for species convervation a) at t=1 s b) at t=2 s c) at t=3 s d) at t=4 s e) at t=5 s f) Numerical results from t=1 s to t=5 s with 1st order and 2nd order for species discretization

Comparison of the results does not fit exactly but show underestimation of numerical results compared to analytical solutions particularly with increasing time as it is presented in Figure B.2 a-e. Evaluation of first and second order spatial discretization for a transferred species conversation from 1 to 5 second does not show any differences.

B.2.1 Mesh size study for diffusive term

As discussed before, the influence of mesh size on diffusive term was investigated as it is shown in Figure B.3. There is no influence of mesh size on diffusive term at different time.

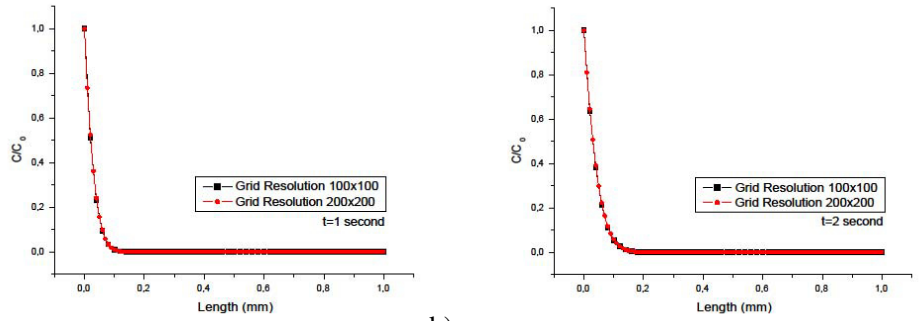

a) b)

Figure B.3: Grid influence on diffusive term obtained in a 1- D study; 1st order species conservation a) at t=1 s b) at t=2 s

B.3 Test of convective term

In order to test the convective term in Equation B.1 analytical solution of mass transfer in uniform flow published by Apelblat (1980) [89] has been used. Figure B.4 shows the computational domain for the numerical case. 100x 100 cell grid resolution is implemented in the numerical studies. Bellow the bottom wall a constant concentration and overall a uniform steady state velocity (plug flow)is implemented at the inlet with a user defined function. To provide the plug flow, a moving wall boundary conditions at the bottom and top wall have been applied.

Table B.1 shows the physical properties, as well as the inlet boundary conditions of the test problem.

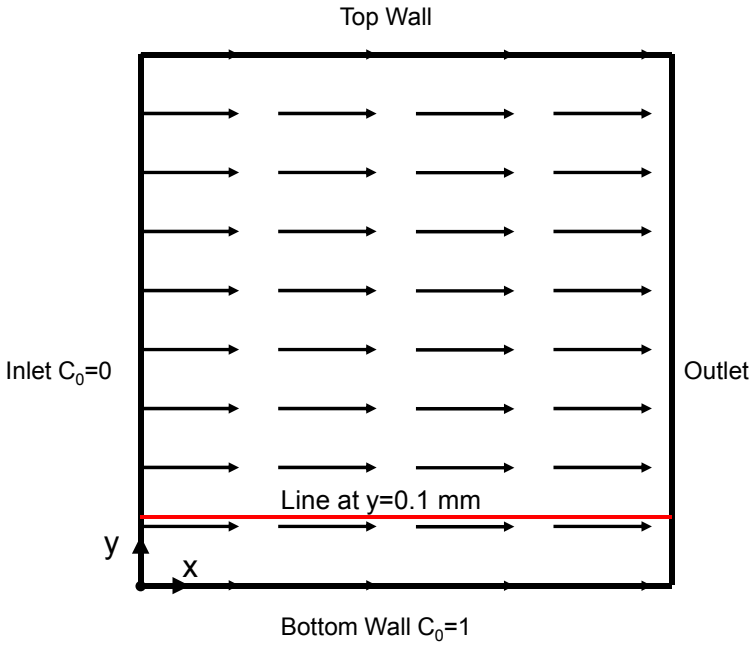

Figure B.4: Geometry of 2-D study on the convective term

ρ_g	1 kg/m^3
ρ_l	1 kg/m^3
μ_g	1.10^{-5}Pa.s
μ_l	1.10^{-5}Pa.s
D_{gl}	1.10^{-5}m^2/s
u_0	1 and 0.1 m/s

Table B.1: Physical properties of gas and liquid for the test case (2-D) of the convective term.

Analytical solution for convective term is [89]:

$$\frac{C(X,Y)}{C_0} = 1 - erf\left(\frac{Y}{2\sqrt{X}}\right) \tag{B.7}$$

where Y, and X are;

$$Y = \frac{y}{\sqrt{D}} \quad X = \frac{x}{U_0} \tag{B.8}$$

Differential equation (Eq.B.1) for convective problem is:

$$\nabla \cdot \rho^q f^q \vec{v^q} M_i^q = -\nabla \cdot f^q \vec{J_i^q} \tag{B.9}$$

Figure B.5 shows the concentration plots in the 2-D region with different flow velocity.

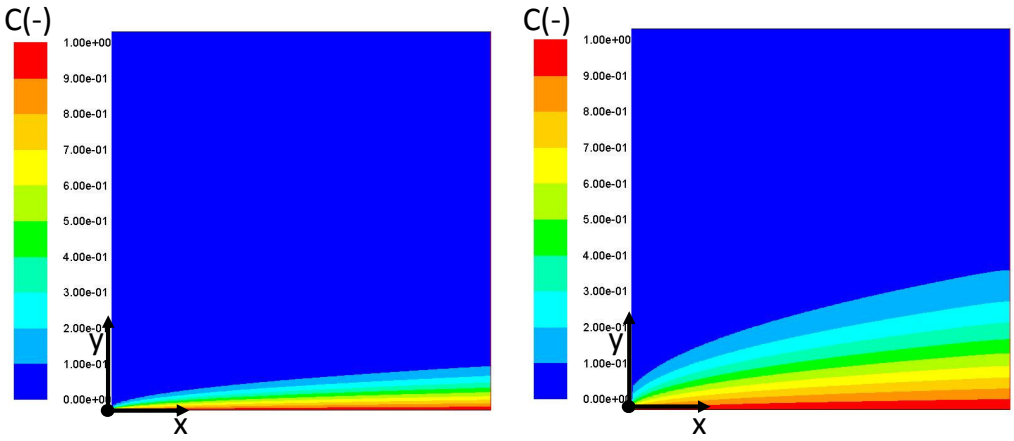

Figure B.5: Numerical results of the concentration in 2-D study of the convective term for a) Inlet velocity 1 m/s b) Inlet velocity 0.1 m/s

Numerical and analytical results show good agreement as it is shown in Figure B.6. It should be noted that in order to plot the numerical solutions, node based data have been used.

In Appendix B.3.1 one can also the find comparison of the numerical results based on node and cell values.

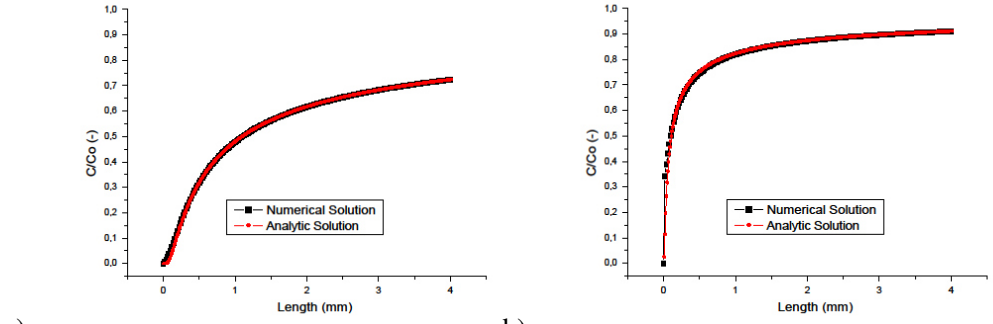

Figure B.6: Comparison of numerical and analytical results in 2-D study on the convective term at y=0.1 mm a) Inlet velocity 1 m/s b) Inlet velocity 0.1 m/s; Node values are used for the numerical plots.

B.3.1 Comparison of node and cell based results for convective term

Node based results have been used during the comparison of the numerical results with theoretical results (Figure B.6). The difference between node based and cell based results for the 2-D study on the convective term can be seen in Figure B.7.

B.4 Test of mass balance

Three interfacial mass transfer theories are known: film theory, penetration theory (Higbie model), and surface renewal theory. The first two models are convenient for laminar flows and the latter is valid more for turbulent flows.

For the first model the determination of the mass transfer coefficient is the key issue. In order to determine the mass transfer coefficient three different approaches are eligible. A mass transfer coefficient could be calculated from the Sherwood number depending on local physical and geometrical parameters [40]. Experimental correlations are needed therefore [90]. A mass transfer coefficient based on the penetration model can also be adapted with knowledge of physical and geometrical parameters [40]. The better way, however, is based on a rigorous numerical approach with a mass transfer coefficient depending on the numerical

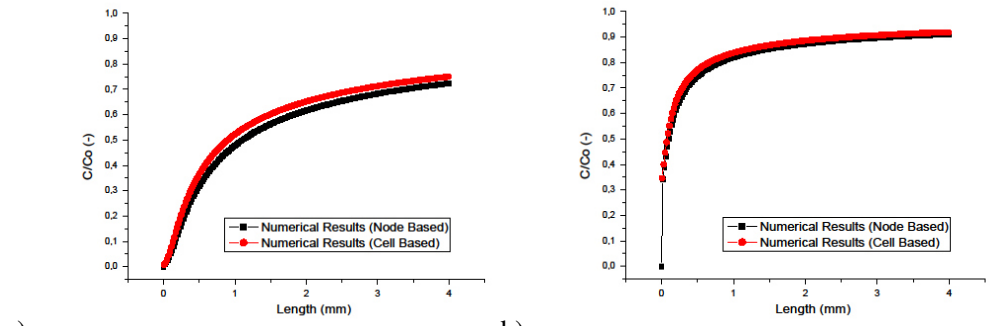

Figure B.7: Comparison of numerical results of node based and cell based concentrations at y=0.1 mm a) Inlet velocity 1 m/s b) Inlet velocity 0.1 m/s: 2-D study on convective term

concentration gradients [47].

In the following the film theory approach with a constant mass transfer coefficient is considered in order to validate the mass balance with a virtual problem for which, in certain cases, an analytical solution exists for mass balance. A user defined function inserted into code in order to calculate the gas bubble shrinkage in the VOF method due to mass transfer coefficient.

For comparison with the analytical solution a mass transfer problem from the book of Diffusion from Cussler [91] has been chosen. Oxygen bubble diameter is 0.05 cm at the beginning and after 420 second it becomes 0.02 cm. Physical properties at STP for oxygen have been implemented. The mass transfer for the analytical solution and the transfer in the interface cell have been written as:

$$S = \frac{d(m_g)}{d(t)} = kA\Delta C = kA(C_{sat} - C_{dis}) \tag{B.10}$$

A analytical solution is possible, when $C_{liq} = 0$ is assumed at any time. Then

the mass transfer coefficient gets

$$k = 1.6 \times 10^{-5} \frac{m}{s}$$

The interfacial area has been calculated in the user defined function using Equation **??**. The mass transfer source term (Equation B.10) has been added into the calculation of the void fraction (Equation 4.19) by help of a user defined function. The mass term is negative for the gas phase and positive for the liquid phase. In this study it is also assumed that the concentration of species is so low that it does not change the phase density, which remains therefore constant.

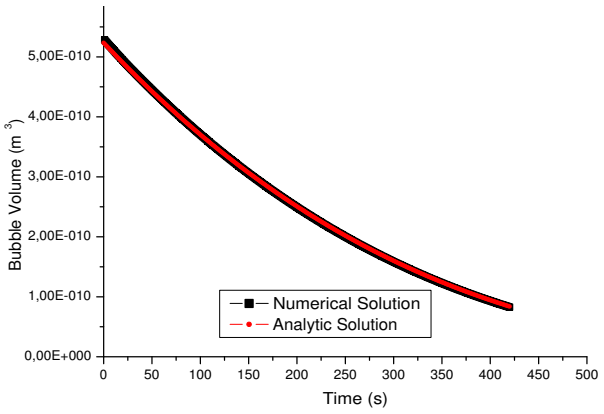

Figure B.8: Comparison of bubble volumes with analytic and numerical solution; a constant mass transfer coefficient of k=$1.6 \times 10^{-5} \frac{m}{s}$,$C_{liq} = 0$ and a grid with 40x40x40 cells is used.

The line with dots in Figure B.8 represents the analytical solution while the line with squares corresponds to the numerical result. These two lines are perfectly fitting each other.

B.4.1 Influence of mesh size on mass balance

The coarse mesh size may influence the preciseness of the numerical results compared to the analytical solution as it is shown in Figure B.9. It is possible to reach independency of mesh size for mass balance equation at a grid with 40x40x40 cells

using the constant mass transfer coefficient applied in section B.4.

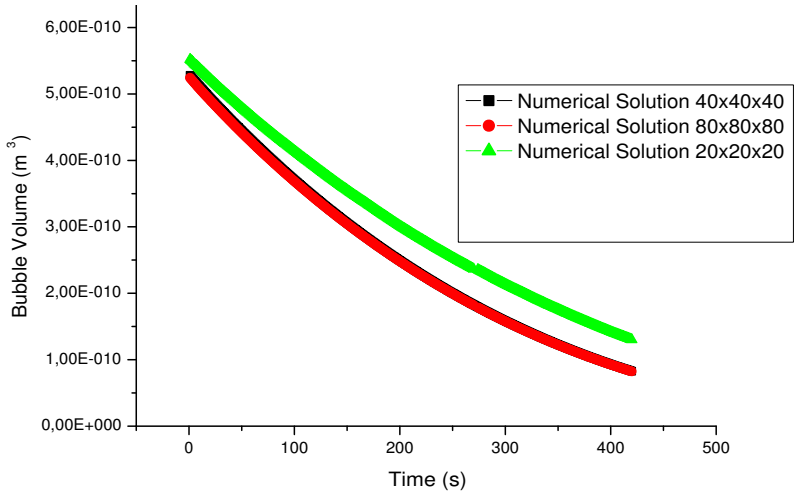

Figure B.9: Influence of mesh size on mass balance a constant mass transfer coefficient of k=1.6×10^{-5}

B.5 Test of first order homogeneous reaction

The same test problem as shown in Figure B.4 has been considered to compare the numerical results of first order homogeneous reaction with analytical results which have been published by Apelblat (1980).

In the case of first order homogeneous reaction, reaction occurs in entire computational domain. Therefore the equation of species conservation (Equation B.1) with accounting homogenous reaction can be read:

$$\nabla \cdot \rho^q f^q \vec{v^q} M_i^q = -\nabla \cdot f^q \vec{J_i^q} + f^q R_{hmg}^{q_i} \tag{B.11}$$

where $R_{hmg}^{q_i}$ is :

$$R_{hmg}^{q_i} = -k_{hmg}^{q} C \tag{B.12}$$

Analytical solution for convective term with homogenous reaction is [89]:

$$\frac{C(X,Y)}{C_0} = \left[exp\left(-a\right) erfc\left(b - c^{1/2}\right) + exp\left(a\right) erfc\left(b + c^{1/2}\right)\right]/2 \tag{B.13}$$

where Y, X, a, b and c are;

$$Y = \frac{y}{\sqrt{D}} \quad X = \frac{x}{u_0} \quad a = k^{1/2}Y \quad b = \frac{Y}{2\sqrt{X}} \quad c = kX \tag{B.14}$$

Figure B.10 shows the results of numerical case with boundary condition of 1 and 0.1 m/s velocity at inlet and homogeneous reaction rate k=1 s^{-1} and 500 s^{-1} respectively.

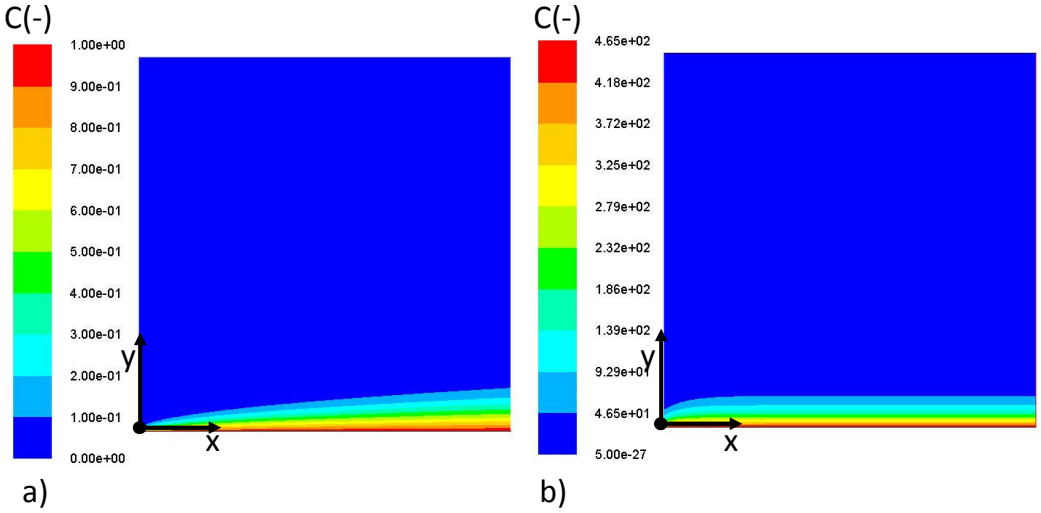

Figure B.10: Numerical results of concentrations in the test on first order homogeneous reaction term in geometry of Figure B.4 a) Inlet velocity 1 m/s, k=1 s^{-1} b) Inlet velocity 0.1 m/s, k=500 s^{-1}

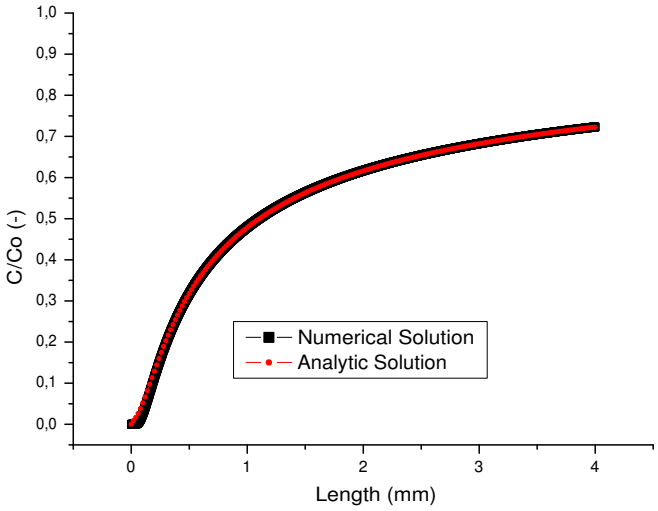

Figure B.11: Comparison of numerical and analytic solution of concentration alon line y=0.1 mm for inlet velocity 1 m/s and k=1 s^{-1}: Test on homogenous 1st order reacion term

	1-D	2-D	3-D
ΔX_{PLIC-2}	0.25	0.25	0.25
ΔX_{PLIC-1}	0.25	0.2356	0.2345

Table B.2: Comparison of calculated ΔX with PLIC-1 and PLIC-2 in 1-D, 2-D and 3-D for f=0.5

B.6 Comparison of PLIC-1 and PLIC-2 concept for a f=0.5

Investigation of similarity of the results from PLIC-1 and PLIC-2 method shows that the the error of the PLIC-2 method for characteristic length is maximum 6 % at f=0.5 as it is summarized in Table B.2 and is displaced in Figure B.12. Therefore the results of PLIC-1 and PLIC-2 for mass transfer are always very similar.

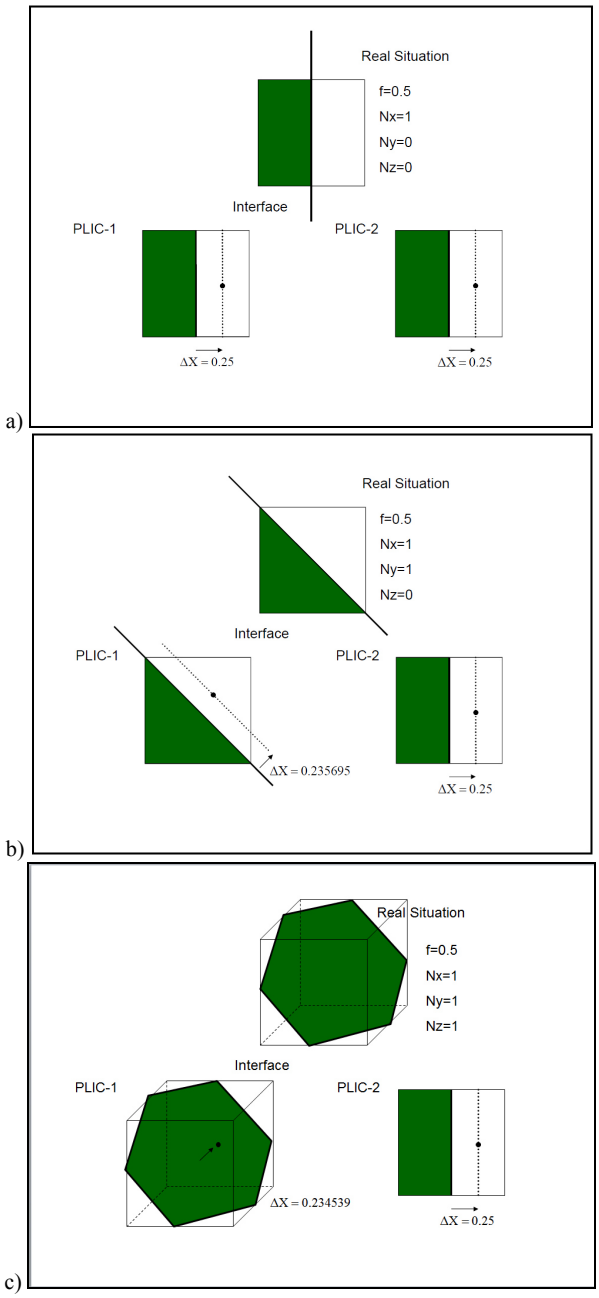

Figure B.12: Calculation of characteristic length using PLIC-1 and PLIC-2 method at f=0.5 for different possible cases of the real interface position a)n_x=1,n_y=0,n_z=0 (1-D) b)n_x=1,n_y=1,n_z=0 (2-D) c)n_x=1,n_y=1,n_z=1 (3-D)

Appendix C

User Defined Functions

As user inputs saturation concentration of gas in liquid phase, mesh size and diffusion coefficient should be given. Define Adjust Macro can be used for different purposes. Here it is used to calculate the interface cells where gas species are exchanged to the liquid phase. Using the same macro concentration of gas in liquid phase and bubble rise velocity are calculated. Define Init is used to initialize the bubble in the domain. Define Mass Transfer macro provides the gas dissolution in the liquid phase due to the concentration difference. Define Volumetric Reaction Rate is used to model reaction mechanisms.

```
/* UDF to define Mass Transfer */
#include "udf.h"
#include "para.h"
#include "math.h"
#include "stdio.h"
#include "prf.h"
/*******************************/
/*USER INPUTS*/
static double Csat=8e-3, D=62.24e-8,maxmesh=3.2e-4;
/*******************************/
```

```
/*GLOBAL VARIABLES THROUGH UDF*/
/* for Define on demand (on_demand_calc)*/
static double Udrp,Udrp2,Uliquid;
/* for Define Adjust (dispersed_V)*/
static double Udrp_V;
/* for Define Adjust (average_C_liq)*/
static double ave_C_liq;
/*Global variable. Time step is never <0 for Define Adjust (dispersed_V)*/
static int last_ts_U = -1, last_ts_V = -1, last_ts_V2 = -1,last_ts_W =
-1, last_ts_V_c = -1, last_ts_C = -1;
/*calculation of discretization length based on void fraction and normals*/
extern double GetVolumenSchwerpunkt(double Volumen, double Normale[3]);
/*******************************/
/*Determination of dispersed phase area*/
DEFINE_ADJUST(store_gradient, domain)
{
Thread *t;
Thread **pt;
cell_t c;
int phase_domain_index = 0.;/*0 dispersed phase */
Domain *pDomain = DOMAIN_SUB_DOMAIN(domain,phase_domain_index);
{
Alloc_Storage_Vars(pDomain,SV_VOF_RG,SV_VOF_G,SV_NULL);
Scalar_Reconstruction(pDomain,SV_VOF,-1,SV_VOF_RG,NULL);
Scalar_Derivatives(pDomain,SV_VOF,-1,
SV_VOF_G,SV_VOF_RG, Vof_Deriv_Accumulate);
}
mp_thread_loop_c (t,domain,pt)
if (FLUID_THREAD_P(t))
{
Thread *ppt = pt[phase_domain_index];
begin_c_loop (c,t)
{
```

```
C_UDMI(c,t,0)=NV_MAG(C_VOF_G(c,ppt));
C_UDMI(c,t,1)=C_VOF_G(c,ppt)[0];
C_UDMI(c,t,2)=C_VOF_G(c,ppt)[1];
C_UDMI(c,t,3)=C_VOF_G(c,ppt)[2];
C_UDMI(c,t,4)=C_VOF(c,ppt);
}
end_c_loop (c,t)
}
Free_Storage_Vars(pDomain,SV_VOF_RG,SV_VOF_G,SV_NULL);
}
/*******************************/
/*Initialization of bubble*/
DEFINE_INIT(my_init_function, domain)
{
Thread *t;
Thread **pt;
Thread **st;
cell_t c;
Domain *pDomain = DOMAIN_SUB_DOMAIN(domain,P_PHASE);
Domain *sDomain = DOMAIN_SUB_DOMAIN(domain,S_PHASE);
real xc[ND_ND], y, x,z;
mp_thread_loop_c (t,domain,pt)
if (FLUID_THREAD_P(t))
{ Thread *tp = pt[P_PHASE];
begin_c_loop_int (c,t) { C_CENTROID(xc,c,t);
x=xc[0];
y=xc[1];
z=xc[2];
if ( 0.00192< sqrt((pow(x-0.008,2)+
pow(y-0.008,2)+pow(z-0.008,2))))
C_VOF(c,tp) = 0;
else
C_VOF(c,tp) = 1;
```

```
} end_c_loop_int (c,t) }
mp_thread_loop_c (t,domain,st)
if (FLUID_THREAD_P(t)) {
Thread *sp = st[S_PHASE];
begin_c_loop_int (c,t) {
C_CENTROID(xc,c,t);
x=xc[0];
y=xc[1];
z=xc[2];
if ( 0.00192< sqrt((pow(x-0.008,2)+pow(y-0.008,2)+pow(z-0.008,2))))
C_VOF(c,sp) = 1;
else
C_VOF(c,sp) = 0;
}
end_c_loop_int (c,t)
}
}
/*******************************/
/*Calculation of dispersed concentration in continuous phase */
DEFINE_ADJUST(max_C_liq, domain)
{
Thread *t;
Thread **pt;
cell_t c;
real C_liq,C_liq_pt;
real m_f,m_f_C,m_f_t,m_f_t_C;
int phase_domain_index = 1.;/*1 mixture*/
Domain *pDomain = DOMAIN_SUB_DOMAIN(domain,phase_domain_index);
mp_thread_loop_c (t,domain,pt)
if (FLUID_THREAD_P(t))
{
Thread *ppt = pt[phase_domain_index];
begin_c_loop (c,t)
```

```
{
/*m_f=species mass fraction of dispersed phase at actual time*/
m_f=C_YI(c,ppt,0);
C_UDMI(c,t,5)=m_f; if (C_VOF(c,ppt) !=0)
m_f=C_YI(c,ppt,0);
else
m_f=0;
C_UDMI(c,t,6) = m_f;
C_UDMI(c,t,7) = m_f*1205/18;/*concentration H202-02 kmol/m3*/
m_f_C=m_f*1205;/*concentration kg/m3*/
C_UDMI(c,t,8) =m_f_C ;/*concentration kg/m3*/
if (m_f_C>=C_sat)
m_f_C=C_sat;
else
m_f_C=m_f_C;
C_UDMI(c,t,9) =m_f_C ;/*concentration kg/m3*/
if (C_VOF(c,ppt) !=0)
C_liq=m_f_C;/*C_liq is the Concentration of 02 in the liquid phase at actual time*/
else
C_liq=0;
C_UDMI(c,t,10) =C_liq;/*C_liq kg/m3 the value of C in liquid at t*/
C_UDMI(c,t,11) =C_liq/18;/*C_liq kmol/m3 the value of C in liquid at t*/
}
end_c_loop (c,t)
}
}
/*******************************/
/*Mass transfer from disperped phase to continuous phase*/
DEFINE_MASS_TRANSFER(mstr_d_erg,cell,thread,
from_index,from_species_index, to_index,to_species_index)
{
Thread *gas = THREAD_SUB_THREAD(thread,from_index);
```

```
Thread *liq = THREAD_SUB_THREAD(thread, to_index);
double m_lq=0.0;
double volume_liquid=0.;
double Nx;
double Ny;
double Nz;
double Erg=0.0;
double Erg1=0.0;
double Normale[3];
double Volumen;
volume_liquid=C_VOLUME(cell,thread)*C_VOF(cell,liq);
C_UDMI(cell,thread,17)=volume_liquid;
Nx=C_UDMI(cell,thread,1);
Ny=C_UDMI(cell,thread,2);
Nz=C_UDMI(cell,thread,3);
Normale[0]=Nx;
Normale[1]=Ny;
Normale[2]=Nz;
Volumen=C_VOF(cell,liq);
C_UDMI(cell,thread,18)=Volumen;
if (C_VOF(cell,liq) !=0)
{
Erg= fabs(maxmesh*GetVolumenSchwerpunkt(Volumen, Normale));
}
else
Erg=0.0;
C_UDMI(cell,thread,19)=Erg;
if (C_VOF(cell,liq) >0.05 && Erg>(maxmesh*1e-3) && C_sat>C_UDMI(cell,thread,10))
m_lq=C_UDMI(cell,thread,0)*(D/Erg)*(C_sat-C_UDMI(cell,thread,10));
else
m_lq=0;
C_UDMI(cell,thread,20) =m_lq;
return m_lq;
```

```
}
/*******************************/
/*Calculation of bubble rise velocity*/
DEFINE_ADJUST(dispersed_V, domain)
{
int phase_domain_index = 0;/*0 dispersed phase*/
int curr_ts;
real a_V,b_V,a_tot_V,b_tot_V;
FILE *pf;
/* "Parallelized" Sections */
#if !RP_HOST /* Compile this section for computing processes only (serial
and node) */
Thread *t;
Thread **pt;
cell_t c;
Domain *pDomain =
DOMAIN_SUB_DOMAIN(domain,phase_domain_index);
#endif /* !RP_HOST */
curr_ts = N_TIME;
/* Send the Domain value to all the nodes */
host_to_node_int_1(phase_domain_index);
/* Does nothing in serial */
#if !RP_HOST /* SERIAL or NODE */
/* thread is only used on compute processes */
mp_thread_loop_c (t,domain,pt)
if (FLUID_THREAD_P(t))
{
Thread *ppt = pt[phase_domain_index];
begin_c_loop_int (c,t)
{
a_V =C_VOF(c,ppt)*C_V(c,t);
b_V =C_VOF(c,ppt);
} a_tot_V +=a_V;
```

```
b_tot_V +=b_V;
end_c_loop_int (c,t)
}
# if RP_NODE /* Perform node synchronized actions here*/ /*Does nothing in Serial */
a_tot_V = PRF_GRSUM1(a_tot_V);
b_tot_V = PRF_GRSUM1(b_tot_V);
# endif /* RP_NODE */ #endif /* !RP_HOST */
/* Pass the total velocity and void fraction from nodes to the Host for averaging */
node_to_host_real_3(a_tot_V,b_tot_V,Udrp_V);
/*Does nothing in SERIAL */
node_to_host_real_2(a_tot,b_tot);*/
#if !RP_NODE /* SERIAL or HOST */
pf=fopen("velocity", "a");
if (last_ts_V != curr_ts)
{
last_ts_V = curr_ts;
fprintf(pf,"Udrp_V=%lf ab: %lf %lf %lf %lf
\ n",Udrp_V, a_tot_V, b_tot_V,
a_tot_V/b_tot_V,CURRENT_TIME );
}
fclose(pf);
#endif /* !RP_NODE */ }
```

C.1 Extern macro for 2-D

```
#include <stdio.h>
#include <stdlib.h>
#include <math.h>
static double Nx1;
static double Ny1;
```

```
static double xk[4];
static double yk[4];
#define min(a,b) ( (a<b) ? a:b)
/*-----------------------------------------------------
Case 1; Nx=1 Ny=1 para=0.25
Case 2; Nx=0.1 Ny=1 para=0.25
Case 3; Nx=1 Ny=1 para=0.8
Case 4; Nx=1 Ny=0.1 para=0.25
crtical case Nx=1 Ny=1 para=0.5
critical case Nx=1 Ny=0 para=0;
critical case Nx=1 Ny=0 para=1;
critical case Nx=0 Ny=1 para=0;
critical case Nx=0 Ny=1 para=1;
critical case Nx=1 Ny=1 para=1;
critical case Nx=1 Ny=1 para=0;
*/
void linearequation(double nx1, double ny1,
double nx2, double ny2,
double d1, double d2,
double *x, double *y,
double *det);
void areacalculation(double *x, double *y,
double *area);
void lengthcalculation(double *x, double *y,
double *length);
void centroidxcalculation(double *x, double *y,
double *centroidx,double *area);
void centroidycalculation(double *x, double *y,
double *centroidy,double *area); int main()
int iter;
double darea;
double givenarea;
double para,pl,pr,pm;
```

```
double nx1,nx2,ny1,ny2,d1,d2,det;
printf("Give the givenarea: ");
scanf("%lf", &givenarea);
printf("Give the Nx: ");
scanf("%lf", &Nx1);
printf("Give the Ny: ");
scanf("%lf", &Ny1);
double area;
double length;
double centroidx;
double centroidy;
double distance;
iter=0;
para=0.5;
pl=0;
pr=1;
pm=0.5;
while (iter<500)
{
//Line equation with a point and a normal vector nx(x-x0)+ny(y-y0)=0
/*Normalization*/
nx1 = fabs (Nx1 /sqrt( pow(Nx1,2)+pow(Ny1,2) ));
ny1 = fabs (Ny1 /sqrt( pow(Nx1,2)+pow(Ny1,2) ));
//para=0.5;
d1=para*(nx1+ny1);
/* y=0*/
nx2=0.0;
ny2=1.0;
d2=0.0;
linearequation(nx1,ny1,nx2,ny2,d1,d2, &xk[0],&yk[0],&det);
/* y=1*/
nx2=0.0;
ny2=1.0;
```

```
d2=1.0;
linearequation(nx1,ny1,nx2,ny2,d1,d2, &xk[1],&yk[1],&det);
/* x=0*/
nx2=1.0;
ny2=0.0;
d2=0.0;
linearequation(nx1,ny1,nx2,ny2,d1,d2,
&xk[2],&yk[2],&det);
/* x=1*/
nx2=1.0;
ny2=0.0;
d2=1.0;
linearequation(nx1,ny1,nx2,ny2,d1,d2,
&xk[3],&yk[3],&det);
iter++;
areacalculation(&xk[0],&yk[0],&area);
darea=givenarea-area;
if (fabs(darea)<1e-6) break;
if (givenarea>area) { pl=pm; pr=pr; } else { pl=pl; pr=pm; } pm=(pl+pr)/2;
para=pm; } /**/
if (xk[0]>0.99 && yk[0]==0 && xk[1]>0.99 && yk[1]==1)
/*para 1 Nx 1 Ny 0*/
{
area=0;
xk[0]=1e-6;
xk[1]=1e-6;
para=0; }
else
{
area=area;
xk[0]=xk[0];
xk[1]=xk[1];
para=para;
```

```
}
if (xk[1]>0.99 && yk[1]==1 && xk[3]==1 &&
yk[3]>0.99 ) /*para 1 Nx 1 Ny 1*/
{
area=0;
xk[0]=9.76e-4;
yk[0]=0;
xk[1]=0;
yk[1]=0;
xk[2]=0;
yk[2]=9.76e-4;
xk[3]=0;
yk[3]=0;
para=0;
}
else
{
area=area;
xk[0]=xk[0];
xk[1]=xk[1];
yk[0]=yk[0];
yk[1]=yk[1];
xk[2]=xk[2];
yk[2]=yk[2];
xk[3]=xk[3];
yk[3]=yk[3];
para=para;
}
if (
xk[0]==0 && yk[0]==0 &&
xk[1]==0 && yk[1]==0 &&
xk[2]==0 && yk[2]==0 &&
xk[3]==0 && yk[3]==0 ) /*para 0 Nx 0 Ny 0*/
```

```
{
area=0;
xk[0]=0;
yk[0]=0;
xk[1]=0;
yk[1]=0;
xk[2]=0;
yk[2]=0;
xk[3]=0;
yk[3]=0;
para=0;
distance=0;
}
else
{
area=area;
xk[0]=xk[0];
xk[1]=xk[1];
yk[0]=yk[0];
yk[1]=yk[1];
xk[2]=xk[2];
yk[2]=yk[2];
xk[3]=xk[3];
yk[3]=yk[3];
para=para;
/**/
lengthcalculation(&xk[0],&yk[0],&length);
centroidxcalculation(&xk[0],&yk[0],&centroidx,&area);
centroidycalculation(&xk[0],&yk[0],&centroidy,&area);
/*output*/
if (
xk[0]==0 && yk[0]==0 &&
xk[1]==0 && yk[1]==0 &&
```

```
    xk[2]==0 && yk[2]==0 &&
    xk[3]==0 && yk[3]==0 ) /*para 0 Nx 0 Ny 0*/
    {
    distance =0;
    }
    else
    {
    distance=fabs( (nx1*centroidx) + (ny1*centroidy)- d1) / sqrt( pow(nx1,2)+pow(ny1,2)
);
    }
    printf("**********************************\ n");
    printf("* Results\ n");
    printf("**********************************\ n");
    printf(" xk[0]=%3.3e yk[0]=%3.3e \ n", xk[0],yk[0] );
    printf(" xk[1]=%3.3e yk[1]=%3.3e \ n", xk[1],yk[1] );
    printf(" xk[2]=%3.3e yk[2]=%3.3e \ n", xk[2],yk[2] );
    printf(" xk[3]=%3.3e yk[3]=%3.3e \ n", xk[3],yk[3] );
    printf(" para=%3.3e \ n", para );
    printf(" distance=%3.3e \ n", distance );
    system("PAUSE");
    return 0; }
    void linearequation(double nx1, double ny1,
    double nx2, double ny2,
    double d1, double d2,
    double *x, double *y,
    double *det) { double xq,yq;
    //Cramer's rule
    *det = ( nx1 * ny2 ) - ( ny1 * nx2 );
    xq = ( d1 * ny2 ) - ( ny1 * d2 );
    yq = ( nx1 * d2 ) - ( d1 * nx2 );
    *x= xq / *det;
    *y= yq / *det;
    if ( (*x>=0.0 ) && (*x<=1.0) && (*y>=0.0 )
```

```
&&(*y<=1.0))
{
*x=*x;
*y=*y;
}
else
{
*x=0;
*y=0;
}
//printf("* Results");
//printf(" det=%3.3e",*det);
//printf(" nx1=%3.3e ny1=%3.3e
d1=%3.6e",nx1,ny1,d1);
//printf(" nx2=%3.3e ny2=%3.3e
d2=%3.6e",nx2,ny2,d2);
//printf(" xq=%3.3e yq=%3.3e \n ",xq ,yq );
}
void areacalculation(double *x, double *y,
double *area)
// test case
{
double ek1,ek2,eb;
ek1=min(yk[3],yk[2]);
ek2=min(xk[1],xk[0]);
if (xk[1]==0 && yk[1]==0 && xk[3] ==0
&& yk[3]==0 ) /*case 1 */
*area=xk[0]*yk[2]/2;
else if (xk[0]==0 && yk[0]==0 &&
xk[1] ==0 && yk[1]==0 ) /*case 2*/
*area=ek1+((fabs(yk[2]-yk[3]))/2.0);
else if (xk[0]==0 && yk[0]==0 &&
xk[2] ==0 && yk[2]==0 ) /*case 3*/
```

```
*area=1-((1-xk[1])*(1-yk[3])/2.0);
else if (xk[2]==0 && yk[2]==0 &&
xk[3] ==0 && yk[3]==0 ) /*case 4*/
*area=ek2+((fabs(xk[0]-xk[1]))/2.0);
else if (xk[0]==xk[3]==1 && yk[1]==yk[2]==1 )
/*critical case Nx=1 Ny=1 para=0.5*/
*area=1.0/2.0;
printf("*****************************************************\ n");
printf("* Results\ n");
printf("*****************************************************\ n");
printf(" area=%3.3e \ n", *area );
}
void lengthcalculation(double *x, double *y,
double *length)
{
if (xk[1]==0 && yk[1]==0 && xk[3] ==0 && yk[3]==0 )
*length=sqrt(pow(xk[2]-xk[0],2)+pow(yk[2]-yk[0],2));
else if (xk[0]==0 && yk[0]==0 && xk[1] ==0 && yk[1]==0
) *length=sqrt(pow(xk[3]-xk[2],2)+pow(yk[3]-yk[2],2));
else if (xk[0]==0 && yk[0]==0 && xk[2] ==0 && yk[2]==0
)
*length=sqrt(pow(xk[3]-xk[1],2)+pow(yk[3]-yk[1],2));
else if (xk[2]==0 && yk[2]==0 && xk[3] ==0 && yk[3]==0
)
*length=sqrt(pow(xk[1]-xk[0],2)+pow(yk[1]-yk[0],2) );
else if (xk[0]==xk[3]==1 && yk[1]==yk[2]==1)
/*critical case Nx=1 Ny=1 para=0.5*/
*length=sqrt(pow(xk[1]-xk[0],2)+pow(yk[1]-yk[0],2));
printf("*****************************************************\ n");
printf("* Results\ n");
printf("*****************************************************\ n");
printf(" length=
}
```

```
void centroidxcalculation(double *x, double *y,
double *centroidx,double *area)
{ double Poly_A;
if (1.0-*area<1e-5)
*area=1.0;
else
*area=*area;
Poly_A=(1.0/(6.0*(1.0-*area)));
if (xk[1]==0 && yk[1]==0 && xk[3] ==0
&& yk[3]==0)/*N=5 Cx= E (0 N-1) 1*6A*/
*centroidx=Poly_A*
( ((xk[0]+1.0)*((xk[0]*0.0)-(1.0*yk[0])))+
((1.0+1.0)*((1.0*1.0)-(1.0*0.0)))+
((1.0+0.0)*((1.0*1.0)-(0.0*1.0)))+
((0+xk[2])*((0*yk[2])-(xk[2]*1.0)))+
((xk[2]+xk[0])*((xk[2]*yk[0])-(xk[0]*yk[2])))
);
else if (xk[0]==0.0 && yk[0]==0.0 &&
xk[1]==0.0 && yk[1]==0.0 )
*centroidx=Poly_A*
(
((xk[2]+xk[3])*((xk[2]*yk[3])-(xk[3]*yk[2])))+
((xk[3]+1.0)*((xk[3]*1.0)-(1.0*yk[3])))+
((1+0.0)*((1.0*1.0)-(0.0*1.0)))+
((0.0+xk[2])*((0.0*yk[2])-(xk[2]*1.0)))
);
else if (xk[0]==0 && yk[0]==0 &&
xk[2] ==0 && yk[2]==0)
*centroidx=Poly_A*
(
((xk[3]+1.0)*((xk[3]*1.0)-(1.0*yk[3])))+
((xk[1]+1.0)*((yk[1]*1.0)-(1.0*xk[1])))+
((xk[3]+xk[1])*((xk[1]*yk[3])-(xk[3]*yk[1])))
```

```
);
else if (xk[2]==0 && yk[2]==0 &&
xk[3] ==0 && yk[3]==0)
*centroidx=Poly_A*
(
((1+xk[0])*((0.0*xk[0])-(yk[0]*1)))+
((1+1)*((1*1)-(1*0)))+
((xk[1]+1)*((yk[1]*1.0)-(1*xk[1])))+
((xk[1]+xk[0])*((xk[1]*yk[0])-(xk[0]*yk[1])))
);
else if (xk[0]==xk[3]==1 && yk[1]==yk[2]==1)
/*critical case Nx=1 Ny=1 para=0.5*/
*centroidx=Poly_A*
(
((xk[0]+1.0)*((xk[0]*0.0)-(1.0*yk[0])))+
((1.0+1.0)*((1.0*1.0)-(1.0*0.0)))+
((1.0+0.0)*((1.0*1.0)-(0.0*1.0)))+
((0+xk[2])*((0*yk[2])-(xk[2]*1.0)))+
((xk[2]+xk[0])*((xk[2]*yk[0])-(xk[0]*yk[2])))
);
printf("*****************************************************\ n");
printf("* Results\ n");
printf("*****************************************************\ n");
printf(" centroidx=%3.3e \ n", *centroidx );
printf(" 1-area=%3.3e \ n", 1-*area );
printf(" Poly_A=%3.3e \ n", Poly_A );
}
void centroidycalculation(double *x, double *y, double *centroidy,double *area)
{ double Poly_A;
if (1.0-*area<1e-5)
*area=1.0;
Poly_A=(1.0/(6.0*(1.0-*area)));
if (xk[1]==0 && yk[1]==0 &&
```

```
xk[3] ==0 && yk[3]==0)/*N=5 Cx= E (0 N-1) 1*6A*/
*centroidy=Poly_A*
(
((yk[0]+1.0)*((xk[0]*0.0)-(1.0*yk[0])))+
((1.0+1.0)*((1.0*1.0)-(1.0*0.0)))+
((1.0+0.0)*((1.0*1.0)-(0.0*1.0)))+
((0.0+yk[2])*((0.0*yk[2])-(xk[2]*1.0)))+
((yk[2]+yk[0])*((xk[2]*yk[0])-(xk[0]*yk[2])))
);
if (xk[0]==0 && yk[0]==0 &&
xk[1] ==0 && yk[1]==0 )
*centroidy=Poly_A*
(
((yk[2]+yk[3])*((xk[2]*yk[3])-(xk[3]*yk[2])))+
((yk[3]+1.0)*((xk[3]*1.0)-(1.0*yk[3])))+
((1.0+1.0)*((1.0*1.0)-(0.0*1.0)))+
((1.0+yk[2])*((0.0*yk[2])-(xk[2]*1.0)))
);
else if (xk[0]==0 && yk[0]==0 &&
xk[2] ==0 && yk[2]==0)
*centroidy=Poly_A*
(
((yk[3]+1.0)*((xk[3]*1.0)-(1.0*yk[3])))+
((yk[1]+1.0)*((yk[1]*1.0)-(1.0*xk[1])))+
((yk[3]+yk[1])*((xk[1]*yk[3])-(xk[3]*yk[1])))
);
else if (xk[2]==0 && yk[2]==0 &&
xk[3] ==0 && yk[3]==0)
/*case 3*/
*centroidy=Poly_A*
(
((0.0+yk[0])*((0.0*xk[0])-(yk[0]*1)))+
((0+yk[1])*((1*1)-(1*0)))+
```

```
((yk[1]+1.0)*((yk[1]*1.0)-(1*xk[1])))+
((yk[1]+yk[0])*((xk[1]*yk[0])-(xk[0]*yk[1])))
);
else if (xk[0]==xk[3]==1 && yk[1]==yk[2]==1)
/*critical case Nx=1 Ny=1 para=0.5*/
*centroidy=Poly_A*
(
((yk[0]+1.0)*((xk[0]*0.0)-(1.0*yk[0])))+
((1.0+1.0)*((1.0*1.0)-(1.0*0.0)))+
((1.0+0.0)*((1.0*1.0)-(0.0*1.0)))+
((0.0+yk[2])*((0.0*yk[2])-(xk[2]*1.0)))+
((yk[2]+yk[0])*((xk[2]*yk[0])-(xk[0]*yk[2])))
);
printf("*******************************************************\ n");
printf("* Results\ n");
printf("*******************************************************\ n");
printf(" centroidy=%3.3e \ n", *centroidy );
}
```

Appendix D

Modelling of Chemical Reaction

D.1 Chemical studies in literature

In order to provide conversion of the nitrobenzene to aniline (reaction see Figure D.1) the selection of the catalyst is important. For production of aniline via hydrogenation of nitrobenzene either at vapour phase or at liquid phase, different noble metal catalyst were investigated such as palladium [92, 93, 94, 95], platinum [13, 92, 95], nickel [96, 97], and copper [96]. Carbon [98], glass fiber [92], and silica [98] are used as carriers.

Hydrogenation of liquid nitrobenzene to aniline in a membrane reactor was performed by Torres et al. [13] to minimize mass transfer limitation in the microscale. It was found a rate enhancement factor of 20 when comparing the membrane reactor to a model fixed-bed reactor [14]. Hoeller [95] investigated hydrogenation of liquid nitrobenzene to aniline using structured catalytic beds and suggested Pd and Pt supported on glass fibers as catalyst. Yeong et al. [99] determined the yield of aniline produced via hydrogenation of liquid nitrobenzene using a microreactor falling film reactor and found producing aniline with microreactor is more effective than with conventional ones [99]. In a two stage fluidized bed reactor production of aniline has also been studied [100]. A comprehensive study of aniline production has been done by Frikha [101] in a batch

reactor. Hydrogenation of nitrobenzene in liquid phase over an industrial catalyst has been investigated in [102].

Both, Eley-Rideal and Langmuir-Hinshelwood mechanism fit the hydrogenation of nitrobenzene to aniline in liquid and vapor phase in different studies [95, 97, 102, 103]. Reaction kinetics of aniline obtaining hydrogenation of vapour nitrobenzene to aniline has been determined in [103, 104]. E.g. for the hydrogenation of liquid nitrobenzene to aniline reaction kinetics as Eley-Rideal model using Pd/Carbon is proposed by Hoeller et al. [95]:

$$r(C_{H_2}, C_{NB}) = k' \frac{K_{NB} C_{NB}}{1 + K_{NB} C_{NB}} \tag{D.1}$$

Frikha (2006) proposed a reaction rate of aniline catalyzed with Pd/Carbon [101] according to:

$$r(C_{H_2}, C_{NB}) = \frac{47.8}{3} e^{\frac{-2422}{T}} C_{cat} C_{NB}^{1/3} C_{H_2} \, (mol/m^3 s) \tag{D.2}$$

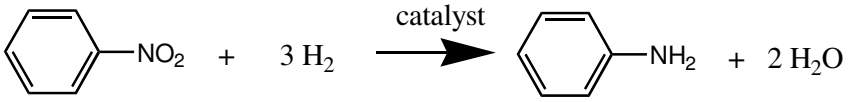

Figure D.1: Hydrogenation of nitrobenzene to aniline

D.2 Applied Reaction Mechanism in Simulation

The model of Hoeller et al. [95] was applied to build up the user defined function for a reaction at the catalyst coated channel walls of the microreactor.

K_{NB} is the adsorption coefficient for nitrobenzene while k^l is the modified reaction rate constant in Equation D.1. K_{NB} is obtained 7.2 l/mol by Hoeller et

al. [95]. k^l=0.74 mol/(g.l.s) was given by Hoeller et al. at 7 bar and should be recalculated to 1 bar.

The modified reaction rate constant is :

$$k^{'} = k_{Pd}.C_{sat} \rightarrow k_{Pd} = \frac{k^{'}}{C_{sat}} \tag{D.3}$$

Saturation concentration of hydrogen in nitrobenzene at 7 bar is $1{,}25.10^{-2}$ mol/l. Then the reaction rate constant for Pd (k_{Pd}) is 59.2 1/(g.s).

In order to use the reaction rate in Equation D.3, the amount of Pd should be known. The required data is the active Pd in the microreactor. Geiss (2010) [64] determined the active palladium in the microreactor: 0.011g catalyst is used with 5% Pd loading and 25% metal dispassion (case A). Surface of the sheet metal (194.4 mm^2) contains 0.0001375 gr Pd. Area specific Pd in the microreactor is thus 7.07 10^{-1} g/m^2. Jaiser (2011) [105] also determined 0.135 gr/m^2 with 33% dispassion. Therefore the area specific Pd in the microreactor in this case is 4.46 10^{-2} g/m^2 (case B).

	Total active Pd (gr)	reaction rate constant (1/s)
Case A (at T=110^0C)	8 10^{-6}	$4{,}73.10^{-4}$
Case B (at T=150^0C)	5 10^{-7}	$2{,}96.10^{-5}$

Table D.1: Reaction rate constants and total active Pd in the simulated geometry for hydrogenation of nitrobenzene divided from the lab microreactor containing a single channel with Pd/C coating

Total active Pd in computational domain is 8 10^{-6} and 5 10^{-7} g for Case A, and Case B respectively (Table D.1). Then reaction rate constant for hydrogenation of nitrobenzene to aniline using Palladium catalyst (k_R) is

$$k_{R_A} = 59.2\ 1/(g.s) \times 8\ 10^{-6} g = \ 4.73\ 10^{-4} 1/s(CaseA) \tag{D.4}$$

$$k_{R_B} = 59.2\ 1/(g.s) \times 5\ 10^{-7} g = \ 2.96\ 10^{-5} 1/s(Case2) \tag{D.5}$$

After the recalculation of the reaction rate constant for hydrogenation of nitrobenzene to aniline following reaction rate is implemented into computational domain.

$$r_{l,C_{H_2},C_{NB}} = k_R.C_{H_2} \frac{K_{NB}.C_{NB}}{1 + K_{NB}.C_{NB}} \tag{D.6}$$

D.3 Programming of Reaction Mechanism

```
 DEFINE_VR_RATE(vol_reac_rate00,c,t,r,mw,species_mf,rate,rr_t)
{
/*User Inputs*/
real rrb,k_,K_NB,cH_2,C_NB,C_H2;
real a,b,k,d,mass_Pd_tot,mass_Pd_cell; /*Palladium mass gr*/
real r_Cha=0.30; /*radius of channel mm*/
real L=6.00; /*length of the channel mm*/
/*(1/7.4e6)*0.33 total Aktiv Pd in microreactor gr/mm2*/
real total_Pd_mm2=4.46e-08;
real pi=3.14; /*Pi Number*/
/*total area of sheet on the microreactor in the lab mm2*/
real total_area=194.4;
/***********/
real yNBH = species_mf[0];
real yH2O = species_mf[1];
real yAniline = species_mf[2];
real yNB = species_mf[3];
/*================================*/
/* CONSTANTS for kinetic and equilibrium constants*/
```

```
/*modified reaction constant k*cH_2(0.74 mol/l*s*g_Pd=2*0.74*1.e-03 kg/m3*s*kg_Pd)*/
mass_Pd_tot=total_Pd_mm2*2*pi*r_Cha*L; /*5e-07*/
k=59.2*mass_Pd_tot; /*59.2 1/(gr.s) 5.e-7 gr ====> 2.96e-5 1/s*/;
C_UDMI(c,t,40)=k;
/*Adsorption equilibrium constant l/mol=m3/kmol (l/mol=1/123.06 kg/m3)*/
K_NB =7.2;
/* Concentrations */
C_UDMI(c,t,33)=yNBH;
C_UDMI(c,t,34)=yAniline;
C_UDMI(c,t,35)=yH2O;
C_UDMI(c,t,36)=yNB;
C_NB = (C_UDMI(c,t,36)*1106)/123.06;/*kmol/m3*/
C_H2 = (C_UDMI(c,t,33)*1106)/2;/*kmol/m3*/
/*================================*/
C_UDMI(c,t,37)=C_NB;
C_UDMI(c,t,38)=C_H2;
/* Calculation of reaction rate equation. It must be in kmol/(m3*s)*/
rrb=(k*K_NB*C_NB*C_H2)/(1+(K_NB*C_NB));
C_UDMI(c,t,39)=rrb;
//if ( C_UDMI(c,t,17)>1.0e-12)
*rate = (k*K_NB*C_NB*C_H2)/(1+(K_NB*C_NB));
//else
*rr_t = *rate;
}
```

References

[1] ULMANN. http://www.wiley-vch.de/vch/software/ullmann.

[2] I. Hassan M. Vaillancourt K. Pehlivan. Two−phase flow regime transitions in microchannels: A comparative experimental study. *Microscale Thermophysical Engineering*, Volume 9:165–182, 2005.

[3] A. Dani P.Guiraud A. Cock. Local measurement of oxygen transfer around a single bubble by planar laser−induced fluorescence. *Chemical Engineering Science*, 62:7245 – 7252, 2007.

[4] M. Stöhr J. Schanze A. Khalili. Visualization of gas-liquid mass transfer and wake structure of rising bubbles using ph−sensitive plif. *Experiments in Fluids*, 47:135–143, 2009.

[5] M. Wörner. Numerical modeling of multiphase flows in micrfluidics and micro process engineering: a review of methods and applications. *Microfluid Nanofluid*, 12:841–886, 2012.

[6] J. Yue L. Luob Y. Gonthierb G. Chena Q. Yuana. An experimental investigation of gas−liquid two−phase flow in single microchannel contactors. *Chemical Engineering Science*, 63:4189 – 4202, 2008.

[7] VDI Waermeatlas 3. Springer, CD Version.

[8] D. Ravid C. Ramshaw A. Harvey. *Process Intensification: Engineering for Efficiency, Sustainability and Flexibility.* Elsevier, 2008.

[9] V. Hessel P. Angeli A. Gavriilidis H. Loewe. Gas−liquid and gas−liquid−solid microstructured reactors: Contacting principles and applications. *Industrial Engineer Chemistry, Resources*, 44:9750–9769, 2005.

[10] J.J. Brandner E. Anurjew L. Bohn E. Hansjosten T. Henning U. Schygulla A. Wenka K. Schubert. Concepts and realization of microstructure heat exchangers for enhanced heat transfer. *Experimental Thermal and Fluid Science*, 30:801–809, 2006.

[11] L. Bohn S. Braune M. Kotthaus M. Kraut P. Pöchlauer M. Vorbach A. Wenka K. Schubert. First large scale application of microreaction technology within commercial chemical production of dsm. 9th Internat.Conf.on Microreaction Technology (IMRET 09), 2006. Potsdam, Germany.

[12] M. Kroeger A. Alke D. Bothe H.J. Warnecke. A vof-based approach for the simulation of reactive mass transfer from rising bubbles. 4th International Berlin Workshop on Transport Phenomena with Moving Boundaries 27th-28th September, 2007. Berlin, Germany.

[13] M. Torres J. Sanchez J.A. B. Dalmon Bernauer J. Lieto. Modelling and simulation of a three−hase catalytic membrane reactor for nitrobenzene hydrogenation. *Industrial and Engineering Chemistry, Research*, 33:2421−−2425, 1994.

[14] J. Peureuxa M. Torres H. Mozzanega A. Giroir-Fendlera J-A. Dalmon. Nitrobenzene liquid-phase hydrogenation in a membrane reactor. *Catalyst Today*, 25:409 – 415, 1995.

[15] R. Sander. Modelling atmospheric chemistry: Interactions between gas−phase species and liquid cloud/aerosol particles. *Survey in Geophysics*, 20:1–31, 1999.

[16] A. Guenther S.A. Khan M. Thalmann F. Trachsel K.V. Jensen. Transport and reaction in microscale segmented gas−liquid flow. *Lab Chip*, 4:278–286, 2004.

[17] Z. Yu O. Heraminger L.S. Fan. Experiment and lattice boltzmann simulation of two−phase gas−liquid flows in microchannels. *Chemical Engineering Science*, Volume 62:7172–7183, 2007.

[18] B.M.A. Wolffenbuttel T.A. Nijhuis A.Stankiewicz J. A. Moulijn. Novel method for non−intrusive measurement of velocity and slug length in two− and three−phase slug flow in capillaries. *Measurement Science and Technology*, Volume 13, Number 10:1540–1544, 2004.

[19] N. Shao A. Gavriilidis P. Angeli. Flow regimes for adiabatic gas-liquid flow in microchannels. *Chemical Engineering Science*, Volume 64:2749–2761, 2009.

[20] J. Aubin M. Ferrando V. Kiricny. Current methods for characterising mixing and flow in microchannels. *Chemical Engineering Science*, 65:2065–2093, 2010.

[21] M.K. Akbar D.A Plummer S.M. Ghiaasiaan. On gas−liquid two−phase flow regimes in microchannels. *International Journal of Multiphase Flow*, 29:855–865, 2003.

[22] T. Cubaud H. Chih−Ming. Transport of bubbles in square microchannels. *Physics of Fluids*, 16:4575–4585, 2004.

[23] S. Waelchli P. Rudolf von Rohr. Two−phase flow characteristics in gas−liquid microreactors. *International Journal of Multiphase Flow*, 32: 791–806, 2006.

[24] A.A Kulkarni J. Joshi. Bubble formation and bubble rise velocity in gas−liquid systems: A review. *Industrial Engineering Chemical Research*, 44:5873–5931, 2005.

[25] F. Takemura A. Yabe. Gas dissolution process of spherical rising bubbles. *Chemical Engineering Science*, 53:2691–2699, 1998.

[26] R. Higbie. The rate of absorption of pure gas into a still liquid during short periods of exposure. *Transactions of the American Institute of Chemical Engineers*, 31:365, 1935.

[27] N. Frössling. Über die verdunstung fallender tropfen (on the evaporation of falling drops. *Gerlands Beitr. Geophys*, 52:170–216, 1938.

[28] B. T. Chao. Motion of spherical gas bubbles in a viscous liquid at large reynolds numbers. *Physics of Fluids*, 5:69–79, 1962.

[29] H. Calderbank and M. B. Moo-Young. The continuous phase heat and mass-transfer properties of dispersions. *Chemical Engineering and Science*, 16:39?54, 1961.

[30] S.R. Duke S. Roy. Laser induced fluorescence measurements of dissolved oxygen concentration fields near air bubble surfaces. *Review of Scientific Instruments*, 71:3494–3502, 2000.

[31] J. Francois N. Dietrich P. Guiraud A. Cockx. Direct measurement of mass transfer around a single bubble by micro−plifi. *Chemical Engineering Science*, 66:3328–3338, 2011.

[32] C.W. Hirt B.D. Nichols. Volume of fluid (vof) method for the dynamics of free boundaries. *Journal of Computational Physics*, 39:201–225, 1981.

[33] M. Suusman P. Smereka S. Osher. A level set approach for computing solutions to incompressible two−phase flow. *Journal of Computational Physics*, 114:146–159, 1994.

[34] G. Tryggvason B. Bunner A. Esmaeeli D. Juric N. Al−Rawahi W. Tauber J. Han S. Nas Y−J. Jan. A front−tracking method for the computations of multiphase flow. *Journal of Computational Physics*, 169:708–759, 2001.

[35] F. Ozkan W. Woerner A. Wenka H.S. Soyhan. Critical evaluation of cfd codes for interfacial simulation of bubble−train flow in a narrow channel. *International Journal for Numerical Methods in Fluids*, 3:537–564, 2007.

[36] T. Taha Z.F. Cui. Cfd modelling of slug flow inside square capillaries. *Chemical Engineering Science*, 61:665–675, 2006.

[37] T.C. Thulasidas M.A. Abraham R.L Cerro. Flow patterns in liquid slugs during bubble-train flow inside capillaries. *Chemical Engineering Science*, 52:2947–2962, 1997.

[38] D. Qian A. Lawal. Numerical study on gas and liquid slugs for taylor flow in a t−junction microchannel. *Chemical Engineering Science*, 61:7609–7625, 2006.

[39] G.Q. Yang B. Du L.S Fan. Bubble formation and dynamics in gas−liquid−solid fluidization: A review. *Chemical Engineering Science*, 62:2–27, 2007.

[40] M.T. Kreutzer F. Kapteijn J.A. Moulijna J.J Heiszwolf. Multiphase monolith reactors: Chemical reaction engineering of segmented flow in microchannels. *Chemical Engineering Science*, 60:5895–5916, 2005.

[41] F. Ozkan K. Hecht P. Pfeifer K. Schubert B. Kraushaar−Czarnetzki. Influence of the contact angle on two−phase flow in microreactors for nitrobenzene−hydrogen−stainless steel/carbon. *Surface and Interface Analysis*, 42:1122–1127, 2010.

[42] H. Brauer. Unsteady state mass transfer through the interface of spherical particles 1: Physical and mathematical description of the mass-transfer problem. *International Journal of Heat and Mass Transfer*, 21:445–453, 1978.

[43] M. Ohta M. Suzuki. Numerical analysis of mass transfer from a free motion drop in a solvent extraction process. *Solvent Extraction Research and Development*, 3:138–149, 1996.

[44] M.R. Davidson M. Rudman. Volume−of−fluid calculation of heat or mass transfer across deforming interfaces in two−fluid flow. *Numerical Heat Transfer*, 41:291–308, 2002.

[45] T. Sato R.T. Jung S. Abe. Direct simulation of droplet flow with mass transfer at interface. *ASME Journal Fluids Engineering*, 122:510–516, 2000.

[46] D. Bothe M. Koebe K. Wielage H.J. Warnecke. Vof simulations of mass transfer from single bubbles and bubble chains rising in aqueous solutions. Proceedings of the Fourth ASME JSME Joint Fluids Engineering Conference July 6 - 11, 2003. Honolulu, Hawaii, USA.

[47] A. Onea M. Woerner D.G. Cacuci. A qualitative computational study of mass transfer in upward bubble train flow through square and rectangular mini−channels. *Chemical Engineering Science*, 64:1416–1435, 2009.

[48] J. Peter L.R. Weatherley. Modelling of mass transfer from falling droplets. *Chemical Engineering Science*, 56:4929–4947, 2001.

[49] M.A. Waheed M. Henschke A. Pfennig. Mass transfer by free and forced convection from single spherical liquid drops. *International Journal of Heat and Mass Transfer*, 45:4507–4514, 2002.

[50] C. Yang Z−H. Mao. Numerical simulation of interphase mass transfer with the level set approach. *Chemical Engineering Science*, 60:2643Ű2660, 2005.

[51] A. Koynov J.G. Khinast G. Trygvasson. Mass transfer and chemical reactions in bubble swarms with dynamic interfaces. *A.I.Ch.E.Journal*, 51: 2786–2800, 2005.

[52] A. Koynov J.G. Khinast. Micro mixing in reactive, deformable bubble, and droplet swarms. *Chemical Engineering and Technology*, 29:13–23, 2006.

[53] D. Darmana N.G. Deen J.A.M. Kuipers. Detailed 3d modelling of mass transfer processes in two−phase flows with dynamic interfaces. *Chemical Engineering and Technology*, 29:1027–1033, 2006.

[54] J. Wang P. Lua Z. Wang C. Yang Z−H. Mao. Numerical simulation of unsteady mass transfer by the level set method. *Chemical Engineering Science*, 63:3141–3151, 2008.

[55] A.A. Ganguli E.Y. Kenig. A cfd−based approach to the interfacial mass transfer at free gas−liquid interfaces. *Chemical Engineering Science*, 66: 3301–3308, 2011.

[56] F. Ozkan P. Pfeifer K. Schubert B. Kraushaar-Czarnetzki. Numerical investigations of bubble generation in microreactors. 1st SynTOP ISBN 978-3-18-092039-9, 2008. Potsdam, Germany.

[57] A.W. Adamson A.P. Gast. *The Solid-Liquid Interface Contact Angle in Physical Chemistry of Surfaces.* John Wiley and Sons Press New York, 1997.

[58] J. Shang M. Flurya J.B. Harsha R.L. Zollars. Comparison of different methods to measure contact angles of soil colloids. *Journal of Colloid and Interface Science*, 328:299–307, 2008.

[59] K. Hecht F. Ozkan P. Pfeifer B. Kraushaar-Czarnetzki. The influence of contact angle in the generation of multiphase flows. Jahrestreffen Reaktionstechnik 2009 Tagungshandbuch S.90,91, 2008. Wuerzburg, Germany.

[60] A.F. Stalder G. Kulik D. Sage L. Barbieri P. Hoffmann. A snake−based approach to accurate determination of both contact points and contact angles. *Journal of Colloid and Interface Science*, 286:92–103, 2006.

[61] J.D. Bernardin I. Mudawar C.B. Walsh E.I. Franses. Contact angle temperature dependence for water droplets on practical aluminium surfaces. *International Journal of Heat and Mass Transfer*, 45:1017–1033, 1997.

[62] T. Takamasa T. Hazuku T. Hibiki. Experimental study of gas liquid two phase flow affected by wall surface wettability. *International Journal of Heat and Fluid Flow*, 29:1593–1602, 2008.

[63] S. Hidaka A. Yamashita Y. Takata. Effect of contact angle on wetting limit temperature. *Heat Transfer Asian Research*, 35:513–526, 2006.

[64] S. Geiss. Hydrierung in mikrostrukturierten reaktoren. Master's thesis, Universitaet Heilbronn, Fakultaet Technik 2, 2010.

[65] J.U. Brackbill D.B. Kothe C. Zemach. A continuum method for modelling surface tension. *Journal of Computational Physics*, 100:335–354, 1992.

[66] J. O'Rourke. *Computational Geometry in C.* Cambridge University Press, 1996.

[67] A. Thomas. *Integrated Graphic and Computer Modelling.* Springer, 2008.

[68] T. Bauer R. Guettel S. Roy M. Schubert M. Al−Dahnan R. Lange. Modelling and simulation of the monolith reactor. *Chemical Engineering Research and Design*, 83 (A7):811–819, 2005.

[69] T.A. Nijhuis F.M. Dautzenberg J.A. Moulijn. Modelling of monolithic and trickle bed reactors for the hydrogenation of styrene. *Chemical Engineering Science*, 58, 7:1113–1124, 2003.

[70] Ansys. *Ansys, Fluent User Guide.* Ansys, 2011.

[71] M.C. Oztaskin M. Wörner H. S. Soyhan. Numerical investigation of the stability of bubble train flow in a square mini-channel. *The Physics of Fluids*, 21:042108, 2009.

[72] Ansys. *Ansys, Fluent Theoury Book.* Ansys, 2011.

[73] N. Shao W. Salman A. Gavriilidis P. Angeli. Cfd simulations of the effect of inlet conditions on taylor flow formation. *International Journal of Heat and Fluid Flow*, 29:1603–1611, 2008.

[74] T.C. Thulasidas M.A. Abraham R.L. Cerro. Bubble−train flow in capillaries of circular and square cross section. *Chemical Engineering Science*, 50: 183–199, 1995.

[75] H. Wong C.J. Radke S. Morris. The motion of long bubbles in polygonal capillaries 1−2. *Journal of Fluid Mechanic*, 292:71–110, 1995.

[76] S. S. Ponoth J.B. McLaughlin. Numerical simulation of mass transfer for bubbles in water. *Chemical Engineering Science*, 55:1237–1255, 2000.

[77] G. K. Batchelor. Small scale variation of convected quantities like temperature in turbulent fluid part 1. general discussion and the case of small conductivity. *Journal of Fluid Mechanics*, 5:113–133, 1959.

[78] A. Onea. *Numerical simulation of mass transfer with and without first order chemical reaction in two-fluid flows.* PhD thesis, University of Karlsruhe, Department of Mechanical Engineering, 2006.

[79] M. Koebe. *Numerische Simulation aufsteigender Blasen mit und ohne Stoffaustausch mittels der Volume of Fluid (VOF) Methode.* PhD thesis, University of Paderborn, Department of Mechanical Engineering, 2004.

[80] J. Francois N. Dietrich P. Guiraud A. Cock. Direct measurement of mass transfer around a single bubble by micro−plifi. *Chemical Engineering Science*, 66:3328–3338, 2011.

[81] G. Rosengarten D.J.E. Harvie J. Cooper−White. Contact angle effects on microdroplet deformation using cfd. *Applied Mathematical Modelling*, 30: 1033–1042, 2005.

[82] M. Renardya Y. Renardya J. Lib. Numerical simulation of moving contact line problems using a volume−of−fluid method. *Journal of Computational Physics*, 171:243–263, 2001.

[83] S. Sandesh B. Arijit. Numerical investigation of boundary conditions for moving contact line problems. *Physics of Fluids*, 12:199–511, 2000.

[84] K. Radhakrishnan P.A. Ramachandran P.H. Brahme R.V. Chaudhari. Solubility of hydrogen in methanol, nitrobenzene, and their mixtures: Experimental data and correlation. *Journal of Chemical Engineering Data*, 28: 1–4, 1983.

[85] R. Sander. Compilation of Henry's Law Constants for Inorganic and Organic Species of Potential Importance in Environmental Chemistry; http://www.mpch-mainz.mpg.de/ sander/res/henry.html.

[86] T.K Sherwood R.L. Pigford C.R. Wilke. *Mass Transfer.* McGraw-Hill, 1975.

[87] C.R. Wilke P. Chang. Correlation of diffusion coefficients in dilute solutions. *AIChE Journal*, 1,2:264–270, 1955.

[88] J. Crank. *The Mathematics of Diffusion.* Clarendon Press, Oxford, 1994.

[89] A. Apelblat. Mass transfer with a chemical reaction of the first order: analytical solutions. *Chemical Engineering Journal*, 19:19–37, 1980.

[90] G. Bercic A. Pintar. The role of gas bubbles and liquid slug lengths on mass transport in the taylor flow through capillaries. *Chemical Engineering Science*, 52,22:3709–3719, 1997.

[91] E.L. Cussler. *Diffusion, Mass Transfer in Fluid Systems.* Cambridge University Press, 2009.

[92] L. Kiwi-Minsker I. Yuranov V. Hoeller A. Renken. Supported glass fibers catalysts for novel multi-phase reactor design. *Chemical Engineering Science*, 54:4785–4790, 1999.

[93] J. Wishnak M. Klein. Reduction of nitrobenzene. *Industrial and Engineering Chemistry, Product Research and Development*, 23:44–50, 1984.

[94] X. Yu M. Wang H. Li. Study on the nitrobenzene hydrogenation over a pd-b/sio$_2$. *Applied Catalysis A:General*, 202:17–22, 2000.

[95] V. Hoeller D. Wegricht I. Yuranov L. Kiwi-Minsker A. Renken. Three-phase nitrobenzene hydrogenation over supported glass fiber catalysts: Reaction kinetics study. *Chemical Engineering and Technology*, 23:251–255, 2000.

[96] D.N. Rihani T.K. Narayanan L.K. Doraiswamy. Kinetic of catalytic vapour−phase hydrogenation of nitrobenzene. *Process Design and Development*, 4:403–410, 1965.

[97] F. Turek R. Geike R. Lange. Liquid-phase hydrogenation of nitrobenzene in a slurry reactor. *Chemical Engineering and Processing*, 20,4:213–219, 1986.

[98] E. Brazi G. Cordier G.N. Sauvion. Palladium based catalysts for hydrogenation of nitrobenzene. *Studies in Surface Science, Catalyst*, 75:2459 – 2462, 1993.

[99] K.K. Yeong A. Gavriilidis R. Zapf V. Hessel. Catalyst preparation and deactivation issues for nitrobenzene hydrogenation in a microstructured falling film reactor. *Catalysis Today*, 81:641–651, 2003.

[100] S. Diao W. Qian G. Luo F. Wei Y. Wang. Gaseous catalytic hydrogenation of nitrobenzene to aniline in a two-stage fluidized bed reactor. *Applied Catalysis A: General*, 286:30–35, 2005.

[101] N. Frikha E. Schaer J. Houzelot. Methodology of multiphase reaction kinetics and hydrodynamics identification: Application to catalyzed nitrobenzene hydrogenation. *Chemical Engineering Journal*, 124:19–28, 2006.

[102] J. Relvas R. Andrade F.G. Freire F. Lemos P. Araújo M. J. Pinho C. P. Nunes F. R. Ribeiroa. Liquid phase hydrogenation of nitrobenzene over an industrial ni-sio$_2$ supported catalyst. *Catalysis Today*, 133-135:828–835, 2008.

[103] B. Amon H. Redlingshoefer E. Klemm E. Dieterich G. Emig. Kinetic investigations of the deactivation by coking of a noble metal catalyst in the catalytic hydrogenation of nitrobenzene using a catalytic wall reactor. *Chemical Engineering and Processing*, 38:395–404, 1999.

[104] H.K. Gharda M.C Sliepcevich. Copper catalysts in hydrogenating nitrobenzene to aniline. *Industrial and Engineering Chemistry*, 52:417–420, 1960.

[105] S. Jaiser. Untersuchungen zur hydrierung von nitrobenzol im mikrostrukturreaktor. Master's thesis, Karlsruhe Institute of Technology, Institute for Micro Process Engineering, 2011.